THE MORPHOLOGY AND DYNAMICS OF SUBDUCTING LITHOSPHERE

BY

KAREN MARIE FISCHER

B. S., YALE UNIVERSITY (1983)

SUBMITTED TO THE DEPARTMENT OF
EARTH, ATMOSPHERIC, AND PLANETARY SCIENCES
IN PARTIAL FULFILLMENT OF THE REQUIREMENTS
FOR THE DEGREE OF

DOCTOR OF PHILOSOPHY

AT THE

MASSACHUSETTS INSTITUTE OF TECHNOLOGY
OCTOBER 1988

SIGNATURE OF AUTHOR ______________________________
DEPARTMENT OF EARTH, ATMOSPHERIC, AND PLANETARY SCIENCES

CERTIFIED BY ______________________________
THOMAS H. JORDAN
THESIS SUPERVISOR

ACCEPTED BY ______________________________
THOMAS H. JORDAN
CHAIRMAN, DEPARTMENT COMMITTEE

THE MORPHOLOGY AND DYNAMICS OF SUBDUCTING LITHOSPHERE

BY

KAREN MARIE FISCHER

SUBMITTED TO THE DEPARTMENT OF EARTH, ATMOSPHERIC, AND PLANETARY SCIENCES
ON OCTOBER 31, 1988 IN PARTIAL FULFILLMENT OF THE REQUIREMENTS
FOR THE DEGREE OF DOCTOR OF PHILOSOPHY IN GEOPHYSICS

ABSTRACT

Residual sphere images from deep earthquakes not only detect the presence of slab-associated velocity anomalies but can characterize the morphology and flow of lithosphere subducted into the lower mantle. Observations of seismic strain rate from deep-focus earthquake moment tensor data provide complementary insight into deformation of the slab due to resistance encountered at the 650-km discontinuity. We have compared travel times from deep events in the Kuril and Mariana arcs with the seismic velocity anomalies implied by kinematical models that thicken the slab perpendicular to its plane by reducing the vertical velocity of the flow with depth. We assume that the details of the deformation (whether the slab buckles, imbricates, fragments, etc.) are averaged out along the ray paths, and hence our models constrain the scale, not the mode, of slab thickening. For all models examined, the data require that slab material extends to depths of 900–1000 km. The deep event travel times are best fit by undeformed models, but the ability of the residual sphere method to resolve slab thickness is limited by ray bending effects. Although the Mariana times are consistent with advective thickening factors of 5 or more, factors larger than 3 are ruled out by the Kuril data. Global tomographic models and regional studies which delineate high-velocity anomalies in the lower mantle beneath zones of Cenozoic subduction are consistent with our results, as is recent work on pulse distortion by slab gradients.

Residual sphere analysis was also applied to 25 intermediate- and deep-focus earthquakes in the Tonga arc, mapping variations in slab strike and dip, depth extent and deep lateral advection at all latitudes along the arc. Similarly to the northwest Pacific, the Tonga slab is required to extend below the deepest events to depths of 800–900 km, and the data are consistent with, and in some cases prefer, advective thickening of the deep lithosphere perpendicular to the slab plane of factors of three or more. Considerable variation in slab structure occurs along the arc, and the match that the observed seismicity provides to detailed undulations in slab strike and dip is strong evidence that residual spheres do reflect near-source heterogeneity. Travel times in southern Tonga (21.5° S– 27° S) require that the slab bends to a steeper dip at depth, but residuals in central (19° S– 21.5° S) and northern (13° S– 19° S) Tonga do not. Southern Tonga also contains a cusp in along-arc structure and seismicity whose surface expression in the trench topography corresponds to the intersection of the arc with the Louisville ridge (25° S). Northern Tonga is the locus of considerable complexity. The relationship of seismicity to inferred slab morphology may be explained by the collision of the subducting Tonga lithosphere with a remnant lithospheric fragment, and the southward shear of deep material relative to shallow structure.

Evidence for slab deformation parallel as well as perpendicular to the arc also appears in average strain rate vectors constructed by summing observed moment tensor solutions from the Harvard CMT Catalogue. Assuming that the source data accurately reflect overall slab flow, compression of the deep slab parallel to its dip is balanced by thickening in the cross-strike and shear in the along-strike directions. The axis of maximum shortening deviates significantly more than 20° from down-dip only in northernmost Tonga where seismicity anf travel time data suggest disrupted subduction. Strain rate data indicate that the proportion of along-arc strain rate decreases south to north. Since estimates of scalar strain rate are constant with latitude, the degree of advective thickening perpendicular to the arc reaches a maximum in southern Tonga, assuming that aseismic flow and seismic deformation have the same strain rate geometry. If along-arc flow occurs largely as southward shear of the deeper lithosphere, vector descriptions of strain rate may require thickening factors of at least 1.5 in central Tonga. A substantially greater degree of deformation would be largely aseismic. Thickening factors significantly greater than one may not be necessary to match strain rate data from the arcs of the northwest Pacific where scalar values of strain rate are substantially smaller than in the deep Tonga slab. Aseismic extension of subducting lithosphere into the lower mantle argues against rigorously stratified convection, but a discontinuity in mantle properties, such as an increase in viscosity, is plausible if it merely resists the descending slabs without acting as a complete barrier to flow.

Thesis committee: Thomas H. Jordan, Thesis supervisor
Kenneth C. Creager, University of Washington, Seattle
Marcia K. McNutt
Jason Phipps Morgan

I dedicate this thesis to my grandfather,
George Bogdanovich Kistiakowsky
(1900 - 1982)

He lived with vigor, integrity and compassion,
and, together with my grandmother Elaine,
convinced me to speak up and take myself seriously.

ACKNOWLEDGEMENTS

Tom Jordan was a source of ideas, enthusiasm and tremendous clarity. He allowed me independence while ensuring that I tackled problems rigorously. Tom's research is marked by physical insight and analytical innovation. Working with him convinced me that it is fine to be a little audacious if your science is solid.

Ken Creager contributed much thought and criticism to chapters 2 and 3. He gave me a careful and friendly introduction to residual sphere modeling and was extremely generous with his time, knowledge and computer codes. In addition to being a fine scientist, Ken is one of the most considerate people I know.

Marcia McNutt gave me my start in geophysics at MIT, supervising my generals paper on the thermo-mechanical properties of the Marquesas Swell. Through our continued collaboration on south Pacific problems she has taught me a great deal about how to conduct research. Her intuition and mathematical rigor make working with her a pleasure, and her ability to combine her home and professional lives is an inspiration.

Jason Phipps Morgan provided valuable criticism and perspective on this thesis. I would like to thank him and my other thesis committee members for their encouragement. They made a difficult time almost fun.

Mike Purdy at the Woods Hole Oceanographic Institution supervised my generals paper on the East Pacific Rise oceanic crustal structure. I am grateful to him and the MIT-WHOI Joint Program in Oceanography for their support during my early days in graduate school.

Dave Krowitz kept the Apollo network going and was never too busy to answer a question. Mark Riedesel provided the program which produced the source mechanism plots in Chapter 4, and I am grateful to the group at Harvard for access to the CMT catalogue. Chapter 2 was orginally published in the *Journal of Geophysical Research*, and Vern Cormier, Steve Grand, Brad Hager, John Vidale, Bob Engdahl and John Woodhouse were a source of preprints and helpful discussions. The research presented in this thesis was sponsored by the National Science Foundation under grant EAR 8607340.

I was lucky to go through graduate school with a friendly and inspiring group of students. Many people on the 5th and 8th floors of the Green Building were constructively critical and practically helpful. I will always feel a bond with Sarah Kruse, Beth Robinson, and my classmates Mark Murray, Greg Beroza, and, in particular, Lind Gee. Together we shared a lot of excitement and disappointment.

To my family and my friends from outside the department, thanks for giving me a home, a sense of balance and a lot of love. My mother, Vera Kistiakowsky, taught me determination and high expectations, and she is still my favorite role model. Lisa Greber helped type the references and cheered me on. Lauren Caulton proofread much of the final draft; she has been a steadfast friend and a wonderful source of support.

Curriculum Vitae

Personal :	Born June 16, 1961, Boston, Massachusetts

Education:

9/79 - 5/83	B.S. in Geology and Geophysics, *summa cum laude*, Yale University, New Haven, Connecticut
9/83 - 10/88	Ph.D. in Geophysics, Massachusetts Institute of Technology, Cambridge, MA

Professional Experience:

6/81 - 9/81	Student Research Assistant in Geology and Geophysics, Yale University
6/82 - 9/82	Summer Student Fellow, Lamont-Doherty Geological Observatory, Columbia University
9/83 - 8/84	Graduate Research Assistant, MIT-WHOI Joint Program in Oceanography, Woods Hole Oceanographic Institution
9/84 - 1/88 6/88 - 10/88	Graduate Research Assistant, Department of Earth, Atmospheric and Planetary Sciences, Massachusetts Institute of Technology
1/88 - 5/88	Graduate Teaching Assistant, Department of Earth, Atmospheric and Planetary Sciences, Massachusetts Institute of Technology

Major Research Interests:	Seismology Subduction zones: mantle-lithosphere dynamics Thermo-mechanical modeling of swells and other mid-plate phenomena
Professional Societies:	American Geophysical Union Sigma Xi

Oceanographic Expeditions:

3/87 - 5/87	Leg 2 of the Crossgrain Expedition, Marquesas Islands, French Polynesia.

Scientific Publications:

K. M. Fischer and W. R. McCann. Seismic velocity modeling and earthquake relocation in the northeast Caribbean. *Bull. Seis. Soc. Amer., 74,* 1249-1262, 1984.

K. M. Fischer, M. K. McNutt and L. Shure. Thermal and mechanical constraints on the lithosphere beneath the Marquesas swell. *Nature, 322,* 733-736, 1986.

K. M. Fischer and G. M. Purdy. Seismic amplitude modeling and the shallow crustal structure of the East Pacific Rise at 12°N. *J. Geophys. Res., 91,* 14,006-14,014, 1986.

M. K. McNutt and K. M. Fischer. The South Pacific superswell. *Seamounts, Islands and Atolls,* B. H. Keating, P. Fryer, R. Batiza, and G.W. Boehlert, eds., Geophysical Monograph #43, American Geophysical Union, Washington, D.C., 1987.

K. M. Fischer, T. H. Jordan, and K. C. Creager. Seismic constraints on the morphology of deep slabs. *J. Geophys. Res., 93,* 4773-4783, 1988.

M. K. McNutt, K. M. Fischer, S. Kruse and J. Natland. The origin of the Marquesas Fracture Zone Ridge and its implications for the nature of hot spots, *Earth Planet. Sci. Lett.,* in press, 1988.

K. M. Fischer, K. C. Creager and T. H. Jordan. Mapping the Tonga slab. *J. Geophys. Res.,* in preparation, 1988.

K. M. Fischer and T. H. Jordan. Seismic strain and deep slab deformation, *Earth Planet. Sci. Lett.,* in preparation, 1988.

TABLE OF CONTENTS

CHAPTER 1

INTRODUCTION

Owing to their strong lateral gradients in seismic velocity and abundant deep-focus earthquakes, subduction zones provide ideal locales in which to map mantle flow using seismological data. The first to exploit this phenomenon were the original studies which identified dipping planes of seismicity with downgoing lithospheric slabs [*Sykes,* 1966; *Oliver and Isacks,* 1967; *Isacks et al.,* 1968; *Isacks et al.,* 1969]. They inaugurated a decade in which seismicity and focal mechanism data were the primary tools used to infer slab geometry and extent and often to characterize mantle flow. For instance, the global cut-off in earthquake distribution at roughly 700 km [*Isacks and Molnar,* 1971], the consistent evidence for down-dip compression in the lithosphere below 400 km [*Isacks and Molnar,* 1969, 1971; *Richter,* 1979; *Vassiliou,* 1984; *Giardini,* 1984; *Giardini and Woodhouse,* 1984; *Apperson and Frohlich,* 1987], and the high rate of seismic moment release in the vicinity of the 650-km discontinuity [*Richter,* 1979] have often been cited as evidence for the containment of downwelling lithospheric flow in the upper mantle. However, seismicity and source mechanisms fundamentally provide information on seismic strain release within the lithosphere, not on its structure, and a lack of intermediate- and deep-focus earthquakes cannot be taken to indicate the absence of a subducted slab. In order to elucidate slab structure, high resolution studies of seismic traveltime and waveform data are required. While the frequency dependent effects included in waveform analyses perhaps hold promise for finer resolution of certain features of the downgoing lithosphere [*Vidale,* 1987; *Vidale and Garcia-Gonzalez,* 1988; *Cormier,* 1988], interpreting travel times within a highly heterogeneous, three-dimensional subduction zone structure is at present a much more straightforward task.

Numerous studies of travel time residuals from subduction zone earthquakes have yielded estimates of a velocity contrast of 5% – 10% between the slab and the surrounding mantle [*Toksöz et al.*, 1971; *Mitronovas and Isacks,* 1971; *Fitch,* 1975, 1977; *Sondergeld et al.*, 1977; *Isacks and Barazangi,* 1977; *Frolich and Barazangi,* 1980; *Bock,* 1981; *Huppert and Frohlich,* 1981], but their ability to resolve the geometry and maximum depth extent of the anomaly is limited, particularly below depths of 500 km. However, *Jordan* [1977] and *Creager and Jordan* [1984] found that residual sphere analysis of seismic travel time data from the Kuril-Kamchatka arc required aseismic extension of the slab several hundred kilometers into the lower mantle. Subsequently, *Creager and Jordan* [1986] documented penetration of slab velocity anomalies to depths of at least 900 km beneath the Mariana and Japan arcs, and *Boyd and Creager* [1988] indicate that the Aleutian slab may extend some 350 km below the deepest earthquakes, to depths possibly greater than 600 km. Both of these studies also offer well-constrained estimates of the strike and dip of the surface of the downgoing lithosphere. Recent regional tomographic studies substantiate these findings in whole [*Engdahl and Gubbins,* 1987; *Kamiya et al.*, 1988] or in part [*Zhou and Clayton,* 1988]. The *Boyd and Creager* [1988] and *Engdahl and Gubbins* [1987] models for the Aleutian slab are highly correlated, and the *Kamiya et al.* [1988] inversion for the Japan arc matches the *Creager and Jordan* [1986] parameterization down to the detail of an increase in dip at 500 km depth.

The detection of aseismic slabs below deep-focus zones argues for deep circulation as a component of plate-tectonic return flow and against the hypothesis that the mantle is stratified into two convecting systems with a sharp chemical boundary near the 650-km seismic discontinuity [*Jordan et al.*, 1988]. It does not, however, rule out deformation of the deep slab due to resistance to downward flow at the upper mantle-lower mantle boundary. The most compelling evidence for advective distortion in the deep lithosphere without a doubt occurs in the Tonga arc of the southwest Pacific. This region produces at least 70% of the world's deep-focus earthquakes, a high rate of moment-release [*McGarr,* 1977; *Richter,* 1979], and, unlike many subduction zones where down-dip compression gives way to down-dip tension at intermediate depths, source mechanisms in Tonga indicate shortening parallel to dip even above depths of 300 km [*Isacks and Molnar,* 1971; *Richter,* 1979; *Vassiliou,* 1984; *Apperson and Frohlich,* 1987]. Furthermore, the shape of the downgoing seismicity is far from a simple arcuate surface [*Sykes,* 1966; *Billington and Isacks,* 1975; *Hanus and Vanek,* 1978; *Billington,* 1980; *Louat and Dupont,* 1982], and *Giardini and Woodhouse* relate observed earthquake moment tensors to lineations and trends in the seismicity, providing evidence for advection of the deep lithosphere perpendicular [1984] and parallel [1986] to the slab plane.

Tonga is therefore a logical region in which to study degree and mode of advective deformation in deep slabs, and the major portion of this thesis is dedicated to mapping the morphology of, and strain within, the deep Tonga lithosphere. First, however, we turn to travel time data in the Kuril-Kamchatka and Mariana arcs, where aseismic extension of the lithosphere into the lower mantle has already been documented [*Creager and Jordan,* 1984, 1986], in order to determine first-order constraints on the scale of advective thickening possible in deep slabs (chapter 2). Not only are the geometries of these subduction zones apparently much simpler than Tonga, but their position within the global station network offers better resolution of slab structure perpendicular to its plane using the residual sphere method. In chapter 3 we map the geometry and extent of the Tonga slab using residual sphere analysis of deep- and intermediate-focus earthquakes from all latitudes along the arc. A question of primary importance is whether the Tonga slab extends into the lower mantle, given the indications of resistance to penetration in the seismicity and source mechanism data. Second, we investigate whether travel time data in Tonga are consistent with advective thickening in the cross-strike direction as they are in Kuril-Kamchatka and the Marianas, and if correlations between inferred slab structure and the prominent contortions in the seismicity elucidate deformation parallel as well as perpendicular to the arc. In chapter 4 we return to the source mechanism data, which first suggested the possibility of deformation within the deep slab, to determine whether they yield additional constraints on slab strain and morphology. Exploiting the linear relationship between the earthquake moment tensors and the average seismic strain tensor for the volume containing the events [*Kostrov,* 1974], we map seismic strain rate throughout the deep lithosphere and relate these observations to slab geometry. Of particular interest are the relative amounts of seismic strain rate perpendicular and parallel to the arc, and the ability of moment tensor data to provide additional constraints on the degree of lithospheric thickening in response to compression at the 650-km discontinuity.

The debate between "stratified" and "whole mantle" convection has occupied a prominent place in geophysics over the last five years, and as previously mentioned, the extension of aseismic lithosphere slabs into the lower mantle is a strong argument against a two-layer system with no flux across its border. The zones of documented slab penetration alone represent a flux of 100 km^3/y into the lower mantle, and if we extend this calculation to all oceanic subduction zones, the slab flux rises to 300 km^3/y, implying that a volume equivalent to the entire upper mantle circulates into the lower mantle every billion years [*Creager and Jordan,* 1986]. Recently, however, a class of models have been proposed which allow for discontinutites in either physical properties such as viscosity [*Kincaid and Olson,* 1987; *Gurnis and Hager,* 1988] or small variations in chemical composition [*Silver et al.,* 1988] at the upper mantle-lower mantle boundary. While the arguments for compositional stratification are largely geochemical [*Silver et al.,* 1988], convincing evidence for a viscosity increase of a factor of 10–30 is provided by the long-wavelength geoid [*Hager,* 1984; *Hager et al.,* 1985]. In these models, the slab extends into the lower mantle, but how far it reaches or how much it deforms is a function of the type and degree of discontinuity. Therefore, another motivation for determining deep lithospheric morphology is that these estimates may provide direct observational constraints not only on the gross characteristics of mantle flow, but also on actual values of physical and chemical parameters.

CHAPTER 2

SEISMIC CONSTRAINTS ON THE MORPHOLOGY OF DEEP SLABS

INTRODUCTION

From a seismological point of view the easiest place to map deep mantle flow is in subduction zones, where the lateral gradients in seismic velocities are large and are frequently illuminated by deep focus sources. Studies of travel times from subduction zone earthquakes are providing an increasingly detailed picture of the morphology and extent of the downgoing lithosphere. In a series of papers [*Jordan,* 1977; *Creager and Jordan,* 1984, 1986; *Fischer et al.,* 1986] we have used residual sphere images from Kuril-Kamchatka, Japan, Mariana, and Tonga-Kermadec earthquakes to constrain the strike, dip, and extent of slab material thrust down along the western margin of the Pacific plate. We have found that in all deep focus zones examined thus far, lithospheric slabs must penetrate to depths of at least 1000 km in order to match the amplitude and pattern of travel time anomalies. This large flux of lithosphere into the lower mantle, greater than 100 km^3/yr in the western Pacific alone, is presumably balanced by mass transport from the deep mantle by upwelling plumes. Therefore the detection of aseismic slabs below deep focus zones argues for deep circulation as a component of plate tectonic return flow and against the hypothesis that the mantle is stratified into two convecting systems with a sharp chemical boundary near the 650-km seismic discontinuity [*Jordan et al.,* 1988].

Because the primary focus of our previous studies was to establish the existence of slab material below this discontinuity, we parameterized the downgoing lithosphere as a simple detached thermal boundary layer which undergoes minimal deformation en route to the deep mantle. In the case of the Tonga-Kermadec slab, residual sphere images may suggest a thickening of the slab perpendicular to its strike [chapter 3], but the data in the northwest Pacific can be satisfied by models in which the particle velocities are restricted to the slab plane, with the only significant cross-strike thickening of the slab due to thermal conduction, as opposed to lateral advection [*Creager and Jordan,* 1986]. As noted by *Creager* [1984] and

Creager and Jordan [1986], however, the ability of the residual sphere method to resolve slab width is limited by ray bending effects. They have demonstrated that the trade-off between slab length and slab width is weak and that slab structures considerably wider than simple thermal plate models can satisfy the residual sphere data for the Marianas.

Considerable evidence suggests that slabs encounter resistance to subduction with depth, particularly in the vicinity of the 650-km discontinuity. *Isacks and Molnar* [1969, 1971] documented that focal mechanisms from earthquakes occurring below 400 km require downdip compression, and their conclusion has been confirmed in a number of subsequent studies [e.g., *Vassiliou,* 1984; *Giardini,* 1984]. The data are particularly persuasive in the case of the Tonga deep seismic zone, with its large release of seismic energy [*Richter,* 1979] and moment tensor solutions, suggesting the lateral displacement of lithospheric material perpendicular to the arc [*Giardini and Woodhouse,* 1984]. Of course, these results do not preclude slab penetration into the lower mantle beneath Tonga, and the detection of high-velocity material in the slab plane below 650 km by residual sphere methods indicates that this penetration probably does occur [*Fischer et al.,* 1986; chapter 3]. A model in which the vertical component of flow velocity decreases in the transition zone, causing the lithosphere to thicken by the advection of material away from the slab plane, would reconcile the moment tensor and seismicity data with the residual sphere results.

An increase in viscosity between the upper and lower mantle is one mechanism that could cause the slab to slow and deform while passing through the 650-km discontinuity. *Hager et al.* [1983] and *Vassiliou et al.* [1984] show that small increases in viscosity may induce downdip compression in the deeper regions of the slab, while allowing the slab to penetrate the 650-km discontinuity without much distortion of dip and width, whereas viscosity jumps of several orders of magnitude confine slab flow to the upper mantle. Intermediate viscosity increases allow the slab to penetrate but significantly shorten and thicken it [*Gurnis and Hager,* 1988]. Most authors agree there are large viscosity variations in the uppermost mantle, but the question of how viscosity changes in the deep interior is the subject of a longstanding debate. Although an essentially isoviscous mantle is favored by some authors [*Peltier,* 1974, 1981; *Peltier and Wu,* 1982; *Cathles*, 1975], a moderate viscosity increase in the transition zone does not appear to be precluded by either the postglacial rebound data [*McConnell,* 1968; *Walcott,* 1973] or the systematics of activation energies and volumes [*Sammis et al.*, 1977]. Recent support for viscous stratification has been obtained by *Hager* [1984] and *Hager et al.* [1985], who call for a viscosity increase by a factor of 10–30 at 650 km in order to satisfy the long-wavelength geoid.

Residual sphere images of deep slab penetration and the various hypotheses regarding deformation of slab material are motivating the development of new techniques for mapping subduction flow. A high-velocity slab acts as an "antiwaveguide," reducing the amplitudes and broadening the waveforms of the seismic waves traveling along it [*Sleep,* 1973; *Silver and Chan,* 1986; *Vidale,* 1987; *Cormier,* 1988]. It should be possible to combine this information with travel time data to better constrain the details of slab structure. Although waveform distortions apparently due to deep slab structure have been observed [*Silver and Chan,* 1986; *Beck and Lay,* 1986; *Cormier,* 1988], *Vidale* [1987] has argued that the lack of significant broadening in *SH*-polarized pulses propagating downdip from Kuril-Kamchatka deep focus events is evidence for a slab somewhat thicker than the simple thermal plate models of *Creager and Jordan* [1986]. The problem of interpretation is difficult, however. Accurately computing the propagation of seismic waves through three-dimensional slabs is a nontrivial numerical exercise, especially at angles oblique to the downdip direction where the effects of diffraction and multipathing should be most pronounced [*Silver and Chan,* 1986; *Cormier,* 1988]. Moreover, the inverse problem for amplitudes and waveforms is very nonlinear, and the possible effects of heterogeneities elsewhere along the wave path make it highly nonunique.

Travel times are less sensitive than waveforms and amplitudes to the details of slab deformation but, by the same token, are easier to interpret. This paper uses residual sphere images from deep earthquakes in the northwestern Pacific to establish bounds on the advective thickening of the slab as it penetrates through the transition zone into the lower mantle. The possibility of advective deformation in the deep Tonga slab is examined in chapter 3, but the good azimuthal station distribution for the northwestern Pacific arcs yields more stringent constraints on cross-strike deformation. The forward modeling is similar to our previous studies: a three-dimensional velocity structure is obtained from a temperature field parameterized in terms of a simple kinematical model of subduction flow, which is required to be consistent with the observed seismicity. In this study we generalize the flow model to include the thickening of the slab perpendicular to its plane.

RESIDUAL SPHERE IMAGES

Four deep focus earthquakes were selected for this study, two from the Kuril-Kamchatka arc and two from the Mariana arc (Table 1). Figure 2.1 shows their epicenters on a map of the seismic zones and their hypocenters projected on cross sections through the three-dimensional slab models derived by *Creager and Jordan* [1986]. The slab models were constructed to satisfy the residual sphere data from these and other events. Our method for constructing residual sphere images is essentially identical to that employed by *Creager and Jordan* [1986], and we give only an abbreviated description here. Chapter 3 contains a more in depth discussion. The data are P wave arrival times compiled by the International Seismological Centre (ISC) with ray paths bottoming between 800 km ($\Delta \geq 25°$) and the core-mantle boundary ($\Delta \leq 100°$). Residuals relative to the *Herrin et al.* [1968] radial Earth model are corrected for three types of large-scale aspherical heterogeneity: hydrostatic ellipticity [*Dziewonski and Gilbert,* 1976], mean station anomalies [*Dziewonski and Anderson,* 1983], and the L02.56 lower mantle structure [*Dziewonski,* 1984]. Each observation is assigned a variance that is the sum of two parts, the square of a reading error and *Dziewonski and Anderson's* [1983] single-observation variance about the mean station anomaly. Theoretical times corresponding to the same station set are generated by tracing rays through a three-dimensional slab model, assuming that the hypocenter is located at the ISC depth in the cold thermal core of the slab.

The residual sphere is a plot of residuals, either the observed or theoretical, on the lower focal hemisphere [*Davies and McKenzie,* 1969]. Two operations are applied in an identical manner to both the observed and theoretical residual spheres. The first eliminates any travel time anomalies that can be parameterized as a hypocentral relocation or origin time shift; formally, this relocation procedure is a projection of the N-dimensional residual vectors into an (N–4)-dimensional subspace orthogonal to the discretized and weighted residual sphere harmonics of zeroth and first degree. The second filters the residual spheres by applying an operator whose spectrum tapers smoothly to zero for harmonics of high angular degree. Applying this smoothing operation to the observed times increases the signal-to-noise ratio of near-source heterogeneity by preferentially damping random observational errors and heterogeneities far from the source, whose spectra on the residual sphere are shifted to high wave numbers. Applying it to the theoretical times accounts for the bias in the spectrum of near-source heterogeneity introduced by smoothing the data.

As a measure of the fit of the model to the observations, we compute the variance reduction factor

$$R = 1 - ||\Delta \mathbf{t}_d - \Delta \mathbf{t}_m||^2 / ||\Delta \mathbf{t}_d||^2 \qquad (2.1)$$

where $\Delta \mathbf{t}_d$ is the error-weighted, relocated, and smoothed data residual vector and $\Delta \mathbf{t}_m$ is the corresponding model vector. The procedure for inverting the data is to maximize R by adjusting the parameters of the slab model, which include the local strike, dip, and depth extent, as well as the thermal coefficient $\partial v_p/\partial T$. The latter specifies the (linear) relationship between temperature and compressional velocity; in the study by *Creager and Jordan* [1986], it was determined to be –0.5 ± 0.1 m/s/°K by inverting the data for intermediate focus earthquakes, which are insensitive to how far the slab extends below the seismicity cutoff. This value is consistent with the lower mantle estimates of *Hager et al.* [1985] and various laboratory studies [*Sumino*, 1979; *Sumino et al.*, 1983; *Suzuki and Anderson*, 1983; *Suzuki et al.*, 1983].

Figure 2.2 compares the observed residual spheres for the four deep focus earthquakes used here with the theoretical residual spheres calculated from the best fitting slab models of *Creager and Jordan* [1986]. The agreement is very good, both in the details of the pattern and the overall amplitude. The best variance reduction (R = 88%) is obtained for event 1, an earthquake of intermediate magnitude ($m_b = 6.0$) having sharp, clean arrivals [*Jordan,* 1977]. The worst (R = 66%) is for the smaller magnitude ($m_b = 5.6$) event 3. The three-dimensional models used in the ray tracing were obtained by rotating the cross sections shown in Figure 2.1 about arc poles at 60°N, 130°E for Kuril-Kamchatka and at 20°N, 90°E for the Marianas. The Mariana slab is essentially vertical, while the Kuril-Kamchatka slab displays a change of dip from about $\delta = 52°$ above 500 km depth to $\delta = 72°$ below 600 km [*Veith,* 1974; *Jordan,* 1977; *Creager and Jordan,* 1986]. Both slab models have velocity anomalies persisting to about 1400 km depth. However, as discussed in detail by *Creager and Jordan* [1984, 1986], the residual spheres for the deepest foci "saturate" below about 1000 km; that is, extending the slab model to depths arbitrarily greater than this saturation depth does not change the theoretical patterns, so that extensions below about 1000 km cannot be resolved by the data. Decreasing slab length above this depth does significantly degrade the data model fit, leading us to conclude that the velocity anomaly must continue to at least 1000 km.

MODELING SLAB DEFORMATION

Creager and Jordan [1986] generated the slab structures shown in Figure 2.1 from a two-dimensional, entrained flow model where particle paths are constrained to be parallel to a specified surface and the shear normal to this surface is minimized. An error function thermal profile corresponding to the age of the lithosphere is used to initialize the finite difference algorithm, which computes the temperature structure of the descending lithosphere by stepwise alternating between mass transport and conductive heating [*Toksöz et al.,* 1973]. In such a model the downdip velocity of the slab is constant at the plate tectonic rate, and the temperature anomaly is transported outward from the cold core of the slab by conduction alone; hence lateral thickening occurs very slowly. During the 10 m.y. required for the 150 Ma lithosphere to descend from 200 to 1200 km depth in the Mariana model, for example, thermal diffusion increases slab width by only 20%. This sort of flow obviously cannot be maintained to arbitrary depth, so at some point the lateral advection of thermal anomalies will become important. The form this deformation takes is unclear. *Davies* [1980] catalogues a number of scenarios: buckling, breaking, and imbricating, fragmenting into a shower of small pieces, and so forth. We do not choose among any of these mechanisms; instead, we assume that the details of the deformation are averaged out along the ray paths, so that the travel time data resolve the slab as a smoothly broadening and coherent whole.

We retain the description of subduction as a two-dimensional steady state flow in the plane perpendicular to the slab, and we solve the thermal conduction equation as before. To broaden the slab, however, we construct a new kinematic flow model where the vertical component of particle velocity decreases with depth throughout a given depth range. The particular deformation model adopted in this study is specified by three parameters: z_1, the depth at which the broadening begins; ζ, the depth interval over which it occurs; and γ, the ratio of the vertical particle velocity v_1 at z_1 to the vertical velocity v_2 at $z_2 = z_1 + \zeta$. Mass is conserved and the boundary conditions are such that the ratio of the horizontal velocity u to the vertical velocity v is the same at z_1 and z_2; that is, the slab dip $\delta = \arctan v/u$ is the same above and below the region of deformation. The particle paths are lines of constant $\Gamma(x,z)$, where

$$\begin{aligned} 2\Gamma(x,z) \;=\; & -\,[(1-\gamma^{-1})\cos(\pi(z-z_1)/\zeta) + \gamma^{-1} + 1]\, v_1 x \\ & +\; [(1-\gamma)(2z_1 - z)/\zeta + 2]\, u_1 z \end{aligned} \tag{2.2}$$

The horizontal and vertical components of particle velocity are given by the spatial derivatives of this stream function:

$$u = \partial\Gamma/\partial z \quad v = -\partial\Gamma/\partial x \tag{2.3}$$

This flow field has the property that the slab width smoothly increases (and v decreases) by a factor of γ over the depth range ζ, so that $\gamma = 1$ gives no distortion and $\gamma = 2$ yields a slab twice as thick at z_2 than at z_1. Figure 2.3 illustrates the latter case for the vertically plunging Mariana slab, assuming $z_1 = 580$ km and $\zeta = 150$ km. Figure 2.4 displays the isotherms for the Kuril-Kamchatka slab when $z_1 = 580$ km, $\zeta = 450$ km, and γ is increased from 1 to 2 to 4, and when $z_1 = 580$ km, $\gamma = 3$, and ζ ranges from 150 to 750 km.

CONSTRAINTS ON SLAB WIDTH AND PENETRATION DEPTH

In Figure 2.4 and our subsequent calculations, $\gamma = 1$ corresponds to *Creager and Jordan's* [1986] best fitting models (Figure 2.1). To investigate the slab widths allowed by the travel time data, we have computed the variance ratios R of events 1–4 for a series of models where z_1 is fixed at 580 km, ζ takes on values of 0, 150, 450, and 750 km, and γ is incremented from 1 to 5. Strike and dip were varied, but we found that the values obtained by *Creager and Jordan* [1986] for $\gamma = 1$ were close to optimal over the entire range of parameters with the exception of $\gamma \geq 3$ for $\zeta = 750$ km in the Kurils where shallower slab dips produced better fits to the data. The level of penetration was maintained at 1400 km, well below the saturation depths of 900–1100 km for events 1–4. For each thermal model the velocity structure used to trace the rays was determined from the thermal coefficient of velocity $\partial v_p/\partial T$ that gave the best fit after hypocenter relocation and data smoothing, regardless of its value. We will return to the question of how slab width affects the estimates of $\partial v_p/\partial T$ and saturation depth in our discussion below.

Kuril-Kamchatka slab

Three-dimensional ray bending tends to reduce the sensitivity of the theoretical times to increasing γ. If the ray paths were not significantly perturbed by slab heterogeneity, we would expect the band of negative residuals associated with ray paths in high-velocity slab material to be wider for a thicker (bigger γ) slab. However, because narrower models have larger velocity gradients normal to the slab, rays tend to travel greater distances along the slab core and are bent more sharply as they leave the slab plane. Thus rays to a station not directly along the slab plane will accumulate nearly as much travel time anomaly for a narrow slab as for a wide one. Figure 2.5 illustrates this effect for the Kuril-Kamchatka slab by superimposing theoretical travel times calculated with and without ray bending for a thin ($\gamma = 1$) and a thick ($\gamma = 4$) model as a function of azimuth (ζ was fixed at 150 km). When the times are calculated with no ray bending (top panel), the thick slab produces negative anomalies that are wider by a factor of 3 than the thin slab. Including three-dimensional ray bending (bottom panel) affects the width of the negative troughs for the wide slab very little but substantially widens those for the narrow slab. *Engdahl and Gubbins* [1987] make a similar observation in their study of central Aleutian slab structure. They conclude that if ray bending effects are not included in the inversion of travel time data, slab width is overestimated.

Contours of variance reduction as a function of γ and ζ are shown for the two Kuril-Kamchatka earthquakes in Figure 2.6. The undistorted slab model gives the best variance reduction, obtaining R = 88% and 71% for events 1 and 2, respectively. For constant ζ the fit degrades monotonically with increasing γ. We have shaded in Figure 2.5 the values of R outside the 90% confidence level of acceptability. The critical value was calculated from a chi-square distribution with 10 degrees of freedom, the number of degrees of freedom in the residual sphere smoothing filter. According to this statistical criterion, slab models with thickening factors less than about 3 are acceptable, but those with $\gamma \geq 4$ provide significantly poorer fits to the data for $\zeta = 0$, 150 and 450 km. The $\zeta = 750$ km models are consistent with the data up to γ of at least 5. This insensitivity to increasing γ expresses the simple fact that much of the widening in the ζ = 750 km models occurs below 1000–1200 km, the depth at which the residual spheres from even the deepest events "saturate" with respect to slab length.

Figure 2.6 also indicates that for fixed γ, R is lowest at ζ = 450 km, marginally improving at smaller and larger values. Once the travel time variations associated with unconstrained hypocenter/origin time perturbations have been projected out of the residual spheres, the data are not sensitive to absolute values of v_p but only to velocity gradients in the ray cone below the source [*Creager and Jordan,* 1984, 1986]. In the case of the Kuril-Kamchatka events the gradients normal to the ray paths are minimized for ζ = 450 km; in cross section the slab flares like the ray cone (cf. Figure 2.4). This degrades the match to the residual sphere anomaly patterns.

Figure 2.7 compares the smoothed travel time residuals for event 1 as a function of azimuth, with similar plots computed by subtracting from the observed residual sphere the theoretical patterns for three models where ζ = 150 km and γ = 1, 3, and 5. The quality of the fit provided by the undistorted slab is evident, especially in the northwestern and northeastern quadrants where the dense North American and European station arrays are located. A qualitative assessment of Figure 2.7 (and a similar plot for event 2) corroborates the conclusion drawn from Figure 2.6: γ = 3 is poorer than γ = 1, but not substantially so, whereas γ = 5 is clearly unacceptable. An important feature in the data that is not fit by the wide slab (γ = 5) is the steep gradient in the residuals as a function of takeoff angle in the downdip direction. This is manifested in the steep lineation of misfit times at an azimuth of about –30° in the fourth frame of Figure 2.7, which is not seen for γ = 1 and 3.

Varying slab width produces a relatively subtle change in the pattern of residuals on the focal sphere compared to the simple pattern rotations produced by perturbing strike or dip. Figure 2.8, in a projection identical to Figure 7, shows the effect of decreasing the dip and strike of the reference slab model by 10° for event 1. These perturbations decrease R to 54 and 59%, respectively, well outside the 90% confidence region. If we assume γ = 1, the strike and dip are resolved to ±5° for this earthquake. The orientation parameters are somewhat less resolved for larger value of γ, but the best estimates of strike and dip remain pretty much the same for γ values less than 5 and ζ values less than 750 km.

To examine the constraints on slab length, we plot in Figure 2.9 the event 2 variance reduction contours and $\partial v_p/\partial T$ values for slab models of various penetration depths and thickening factors. The best variance reduction is obtained for small γ and long slabs. The data are quite insensitive to increasing slab length below about 1100 km, the saturation depth for these events, and variance reduction gets worse with increasing γ. When the penetration depth is less than 950 km, variance reduction is unacceptable at the 90% confidence level regardless of the value of γ. At depths less than about 900 km, $\partial v_p/\partial T$ exceeds -1.0 m/s/°K, twice *Creager and Jordan's* [1986] preferred value of -0.5 ± 0.1 m/s/°K. The latter is consistent with the estimate of -0.4 m/s/°K obtained by combining *Hager et al.'s* [1985] value for the large-scale v_p-ρ variation in the lower mantle (4 km s^{-1}/Mg m^{-3}) and *Jeanloz and Thompson's* [1983] thermal expansion coefficient (2.5×10^{-5} °K^{-1}), as well as a number of high-temperature laboratory studies [*Sumino*, 1979; *Sumino et al.*, 1983; *Suzuki and Anderson*, 1983; *Suzuki et al.*, 1983]. Given these constraints on $\partial v_p/\partial T$ from several data sources, $\partial v_p/\partial T$ values much in excess of -1.0 m/s/°K are probably unacceptable.

Mariana slab

As in the case of the Kurils, the undistorted ($\gamma = 1$) Mariana slab model gives the best variance reduction for the two earthquakes considered, and the fit at constant ζ degrades with increasing γ. However, relative to the Kuril-Kamchatka data, residual spheres from the Marianas place weaker constraints on acceptable γ: R values for events 3 and 4 both lie within the 90% confidence region for thickening factors as large as 5 (Figure 2.10). This lower sensitivity is due primarily to three geometrical differences: (1) Because the Marianas are farther than the Kurils from the large station concentrations in western Europe and North America, the number of data points available for the individual events is substantially fewer

(~180 versus 300). (2) In contrast to the Kurils where the slab dips at 72° and the strong downdip gradients in travel time are well sampled by European stations, the orientation and vertical geometry of the Mariana slab lead to smaller amplitudes and gradients on the residual sphere (Figure 2.2). (3) As in the case of the Kurils, the differences in theoretical times generated by models of differing thicknesses are small due to the ray bending effects discussed previously; however, because of the geometrical weakness associated with the station distribution and vertical Mariana slab, these can more readily be mapped into variations in depth and origin times and are therefore projected out in our relocation procedure.

In an attempt to obtain better constraints on γ, we calculated the variance reduction for the same suites of slab models except, rather than allowing an arbitrary relocation of the hypocenter, we fixed the event depth at various values, including that reported by the ISC. The resulting differences in residuals were largely compensated by shifts in origin times, and the dependence of variance reduction on γ was not substantially altered.

Despite their insensitivity to slab thickness, the Marianas data provide a robust lower bound on penetration depth (Figure 2.11). As in the Kurils, the data are relatively insensitive to changes in slab length at depths below about 1000 km, but shortening the slab above this depth produces a rapid decline in the quality of the fit, and a sharp increase in $\partial v_p/\partial T$. The increase in variance reduction with penetration depth for $\gamma = 1$ shown in Figure 2.11 is less rapid than in Figure 2.3 of *Creager and Jordan* [1986] because here we allow $\partial v_p/\partial T$ to vary, whereas they fixed it. Even with this additional flexibility, the minimum slab length determined by the formal 90% confidence region is 800 km. If values of $\partial v_p/\partial T$ larger than −1.0 m/s/°K are rejected, then this minimum penetration depth is increased to about 900 km.

DISCUSSION

The results of this study confirm two conclusions of *Creager and Jordan* [1986]: (1) the lower bounds established by residual sphere data on the depth extent of the high-velocity structures underlying deep focus zones depend only weakly on the cross-strike width of these zones, and (2) structures considerably wider than simple thermal plate models can satisfy the residual sphere data. In particular, significant advective thickening of the slab in and below the transition zone, suggested by the mechanisms of deep focus earthquakes [e.g., *Giardini and Woodhouse,* 1984] and models of subduction flow from a low-viscosity upper mantle to a high-viscosity lower mantle [*Gurnis and Hager,* 1988], is compatible with the travel time data.

The residual sphere images from four deep focus events in the Kuril-Kamchatka and Mariana subduction zones have been used to place an upper bound on the amount of advective thickening. In terms of our particular parameterization of slab deformation (equation 2.2), a thickening factor γ as great as 5 or more can be accommodated in the Marianas. In the Kurils, however, the residual sphere data limit γ to be less than 3 or 4 if the deformation occurs largely above a depth of about 1000 km. We should be quick to point out that we cannot say from our data that such advective broadening is really a feature of subduction flow; in fact, among the models examined here, simple slab penetration ($\gamma = 1$) yields the best fit to the residual spheres of Figure 2.2. But our calculations show there is no discrepancy between the travel time data and the waveform observations and modeling discussed, for example, by *Vidale* [1987].

Of course, the lateral advection of cold slab material must become important somewhere above the core-mantle boundary, and constraining the nature of this plate tectonic return flow is an important task for structural seismology. Some insights are already available from global tomographic mapping and high-resolution regional studies of lower mantle heterogeneity. *Jordan and Lynn* [1974] discovered a high-velocity anomaly for both *P* and *S* waves at depths of 800–1400 km in the lower mantle beneath the Caribbean Sea, which they associated with subduction flow beneath the western margin of North America (see also *Jordan* [1975]). *Lay* [1983] presented additional evidence for the Caribbean anomaly, and *Grand* [1987] has obtained a spectacular three-dimensional image of this feature by a tomographic inversion of multiple-*S* travel times. In his maps the Caribbean anomaly extends northward beneath the central United States and downward to at least 1700 km. It dips eastward and is plausibly explained as the accumulation of cold slab material subducted into the lower mantle during the opening of the Atlantic. The analysis of regional travel times by *Lay* [1983] and the global inversions of body wave data by *Dziewonski and Woodhouse* [1987] indicate that this high-velocity region continues around the periphery of the Pacific into Eurasia.

At a depth of 1200 km the peak amplitude of the Caribbean anomaly measured from *Grand's* [1987] tomographic maps is about 1% and its cross-strike width is a little less than 1000 km. Because of the smoothing Grand used in his inversion, however, the actual anomaly may be narrower with a greater peak amplitude (S. Grand, personal communication, 1988). Unsmoothed plots of travel time anomalies by *Jordan and Lynn* [1974] suggest a total width of about 500 km, which is consistent with the advective thickening models shown in Figure 2.4 and the waveform modeling results of *Vidale and Garcia-Gonzalez* [1988].

The horizontal resolution of the global tomographic inversions of *Dziewonski and Woodhouse* [1987] is about 2000 km in the lower mantle, so their images have been even more severely low-pass filtered. Nevertheless, as these authors have pointed out, the fact that subduction zone anomalies are more evident in the lower mantle than above the seismicity cutoff is an additional argument for some advective thickening. For example, *Dziewonski and Woodhouse's* [1987] P wave map at 1200-km depth (their Figure 2.8) has a broad (~3000 km) positive feature behind the Kuril-Kamchatka arc with peak perturbation of about 0.25%. Integrating along a horizontal line perpendicular to the strike of the arc yields a total travel time anomaly of roughly –0.5 s, a value larger than would be expected from the slab penetration model of Figure 2.1 whose total anomaly of –0.3 s is concentrated in a much narrower zone which low wave number models could not completely resolve. At 1200 km depth, however, the $\gamma = 3$ models displayed in Figure 2.4 have significantly larger cross-strike anomalies (–0.8 s) spread out over a region that is nearly half as wide as in the global models. Filtering such a structure to low wave numbers could explain the tomographic results. The large volume of slab material in the lower mantle that these broad anomalies imply is consistent with the tectonic history of the western Pacific margin [*Hilde et al.*, 1976]; subduction of slabs along this margin at a rate of 80 mm/yr for at least the last 45 m.y. (the approximate age of the bend in the

Emperor-Hawaiian hotspot chain) thrusts enough lithosphere into the upper half of the lower mantle to fill a volume corresponding to $\gamma = 3$.

Advective thickening models such as those shown in Figure 2.4 require strain rates in the deep slab which are significantly greater than the seismic strain rates implied by earthquake moments observed below 500 km. To show this, we approximate the rate of seismic moment release using a method similar to that of *Richter* [1979] which is discussed in more detail in chapter 4. For every event in the 1964–1984 ISC catalog between 500 and 700 km depth with $5.0 \leq m_b \leq 6.0$ in a given subduction zone, we calculate its seismic moment assuming a linear relation between m_b and the logarithm of M_o [*Gutenberg and Richter,* 1955, 1956; *Hanks and Kanamori,* 1979]. We sum the moments over this magnitude range, scale the total to an upper moment cutoff of 2.0×10^{22} N m (2.0×10^{29} dyn cm, corresponding to $m_b = 8$) assuming a b value of unity (b values are discussed more fully in chapter 4; suffice it to say that a b value of unity may cause the rate of seismic moment release to be overestimated). We divide by the time interval to obtain an average rate of seismic moment release, $\dot{M}_{\text{seismic}}$ ($\dot{M} = \partial M_o / \partial t$). In the Kuril and Mariana arcs the rates of seismic moment release are relatively low: $\dot{M}_{\text{seismic}} = 3.7 \times 10^{19}$ N m/yr and 5.3×10^{18} N m/yr, respectively. On the other hand, Tonga, the Earth's most active deep seismic zone, yields $\dot{M}_{\text{seismic}} = 2.7 \times 10^{20}$ N m/yr, a value consistent with *Richter's* [1979] estimate. These rates are sensitive to the upper moment cutoff; the largest deep focus earthquake documented by *Abe and Kanamori* [1979] has an estimated moment of 2.2×10^{21} N m, about an order of magnitude less than our assumed cutoff value. Therefore the values of $\dot{M}_{\text{seismic}}$ given above are likely to be overestimates, unless the largest events are significantly undersampled in the 70-year interval considered by *Abe and Kanamori* [1979].

The strain rate function for the flow described in equation 2.2 can be determined from its spatial derivatives. The integral of this function over slab volume scales to an equivalent rate of moment release, $\dot{M}_{\text{flow}}$. It depends linearly on v_1 and the along-strike extent of the slab and, over the parameter ranges $2 \leq \gamma \leq 4$ and 1 km $\leq x_1 \leq$ 100 km, roughly linearly on γ and x_1 (the latter being the initial width of the deforming volume at z_1; see Figure 2.3). The integral asymptotically decreases to a constant value with increasing ζ; we assume $\zeta = 200$ km, which is consistent with the deformation occuring in the deep seismic zone. We perform this calculation for $x_1 = 25$ km which corresponds roughly to the width of the deep seismicity (except in parts of Tonga where it underestimates the seismic zone) and $x_1 = 100$ km which represents total undeformed slab thickness. $\dot{M}_{\text{flow}}$ values for $x_1 = 25$ km therefore reflect the strain rate due to advective deformation of the seismically active portion of the deep slab, whereas $\dot{M}_{\text{flow}}$ values for $x_1 = 100$ km include the warmer, aseismic outer regions. In Tonga, $\dot{M}_{\text{seismic}}$ for $\gamma = 3$ is only 50% of $\dot{M}_{\text{flow}}$ if $x_1 = 25$ km and 15% of $\dot{M}_{\text{flow}}$ if $x_1 = 100$ km. That is, even in the most seismically active deep slab, the observed moment release can account for less than half of the strain predicted in the seismic core of the slab and less than 10% of the total slab deformation if the thickening factor is 3 or more. In the two subduction zones constrained by the residual sphere data presented in this paper, the discrepancy is much larger: for $x_1 = 25$ km, a thickening factor of 3 implies $\dot{M}_{\text{seismic}}$ is about 5% of $\dot{M}_{\text{flow}}$ for the Kurils and less than 1% for the Marianas. We conclude, therefore, that if substantial advective thickening does occur, the deformation must be largely aseismic.

CONCLUSIONS

While descending lithospheric slabs appear to penetrate the 650-km discontinuity, they may experience considerable advective thickening perpendicular to the arc at or below that depth. Deep event travel times are best fit by undeformed models, but a twofold increase in slab thickness fits all events nearly as well. Although the Mariana times allow advective thickening factors of 5 or more, factors larger than 3 are not consistent with the Kuril data. For all models examined, the data require that slab material extends to depths of 900–1000 km. The insensitivity of the travel time data to slab width, relative to the tight constraints that they place on slab strike, dip, and depth extent, may be explained by the combined effects of three-dimensional ray bending and the geometrical weakness associated with the station distribution and the vertical Mariana slab.

A subducting lithosphere which advectively thickens upon its entry into the lower mantle is consistent with seismicity and moment tensor data which point to compressive stresses in the deep slab. An increase in viscosity between the upper and lower mantle could be the primary dynamical control on such a flow, and an intriguing question for future research is to delimit what range of viscosity structures and slab rheologies are consistent with the above constraints on deep slab thickening. If such deformation does occur, its mechanisms are undoubtably much more complicated than the simple two-dimensional kinematical flow models used here. Our models assume that the details of the deformation (whether the slab buckles, imbricates, fragments, etc.) are averaged out along the ray paths, and hence we constrain only the scale and not the mode of slab thickening. Comparison of observed and predicted rates of seismic moment release suggests that any substantial advective thickening is largely aseismic. Residual sphere modeling in the Tonga arc, where deep events are distributed both normal and parallel to the arc, holds promise for further elucidation of how the deformation of deep slabs may occur.

TABLE 1. SOURCE PARAMETERS OF EVENTS USED IN THIS STUDY

Event	Date	Time, UT	Lat., °N	Lon., °E	Depth, km	m_b	Region
1	Jan. 29, 1971	2158:03.2	51.69	150.97	515	6.0	Kuril-Kamchatka
2	Aug. 30, 1970	1746:08.9	52.36	151.64	643	6.5	Kuril-Kamchatka
3	Oct. 30, 1979	0137:06.6	18.77	145.16	585	5.6	Mariana
4	July 3, 1972	0119:27.3	18.70	145.10	625	5.5	Mariana

Figure 2.1. Map on left is a mercator projection of the northwest Pacific showing the epicenters (solid dots) of events 1–4 modeled in this study. The Pacific plate boundary (barbed line), seismicity contours in kilometers (light lines), and absolute Pacific plate velocity (arrows) are also shown. Slab models on right are for the northern Kuril (top) and Mariana (bottom) arcs [from *Creager and Jordan*, 1986]. *P* wave velocities are contoured at 0.25 km/s, and ambient values are the radial model of *Herrin et al.* [1968]. Circles are projections of well-recorded ISC hypocenters in the vicinity of the profile; the stars indicate the locations of events 1–4.

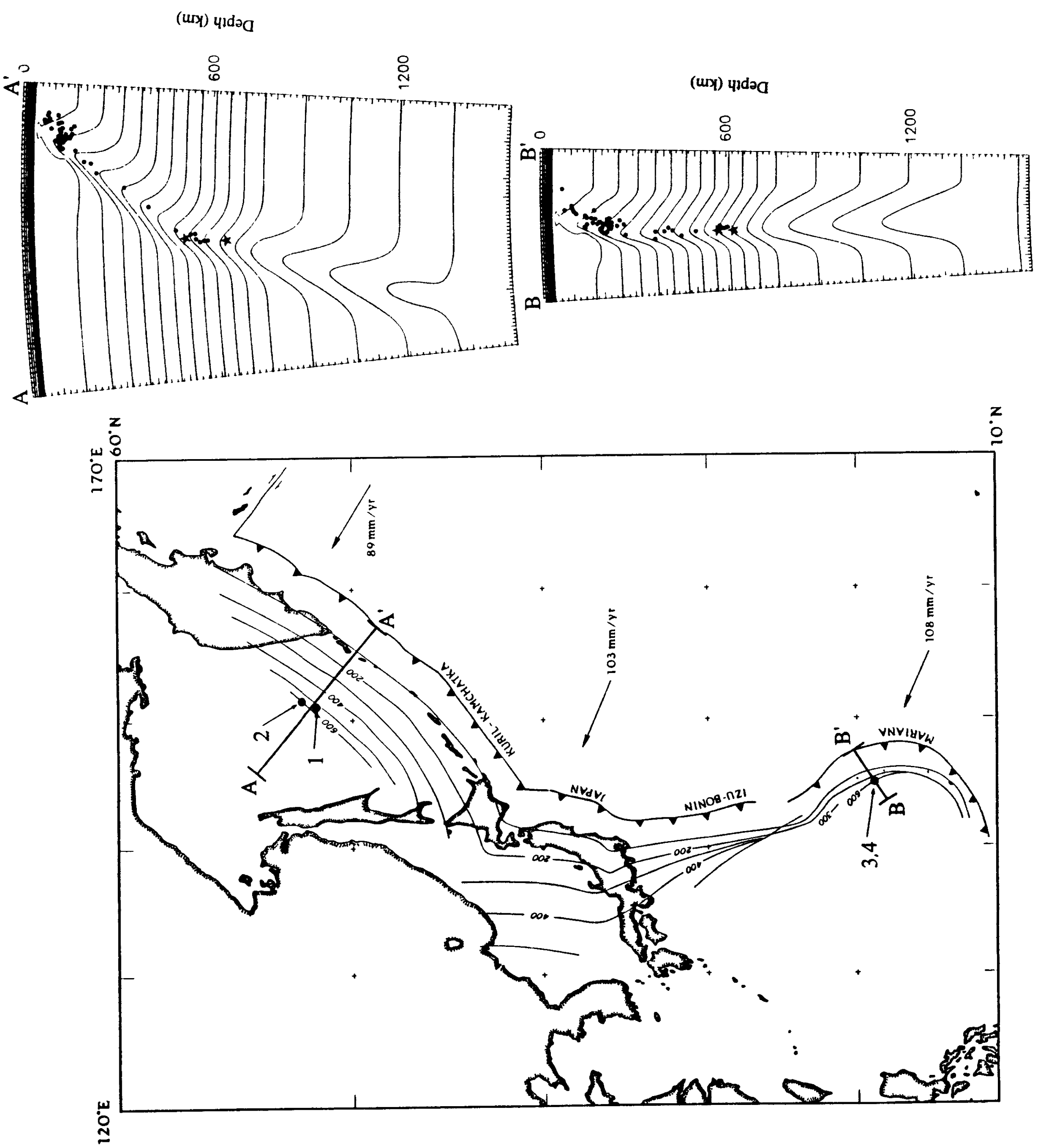
A
A'
0
600
1200
Depth (km)
B
B'
0
600
1200
Depth (km)
120°E
170°E
60°N
10°N
1
2
3,4
KURIL - KAMCHATKA
JAPAN
IZU-BONIN
MARIANA
89 mm/yr
103 mm/yr
108 mm/yr
200
400
600
300

Figure 2.1

Figure 2.2. Observed (left) and theoretical (right) residual spheres for events 1–4. Residual spheres are equal-area, lower hemisphere projections. Outer perimeter corresponds to the locus of rays with takeoff angles of 60° from vertical; data outside this range are not shown. Circles represent negative residuals; crosses are positive; the size of the symbol is proportional to residual, with 1-s residuals shown in upper box. Slab models are shown in Figure 2.1 and correspond to $\gamma = 1$ (no advective thickening). Bold lines running through the theoretical residual spheres represent planes tangent to the slab models from which they were calculated. In the Kurils the local slab strike is 31° and the dip below 500 km is 72°; the Mariana slab dips at 90° below 200 km, and its strike is 327°. Numbers in upper right are ISC depths.

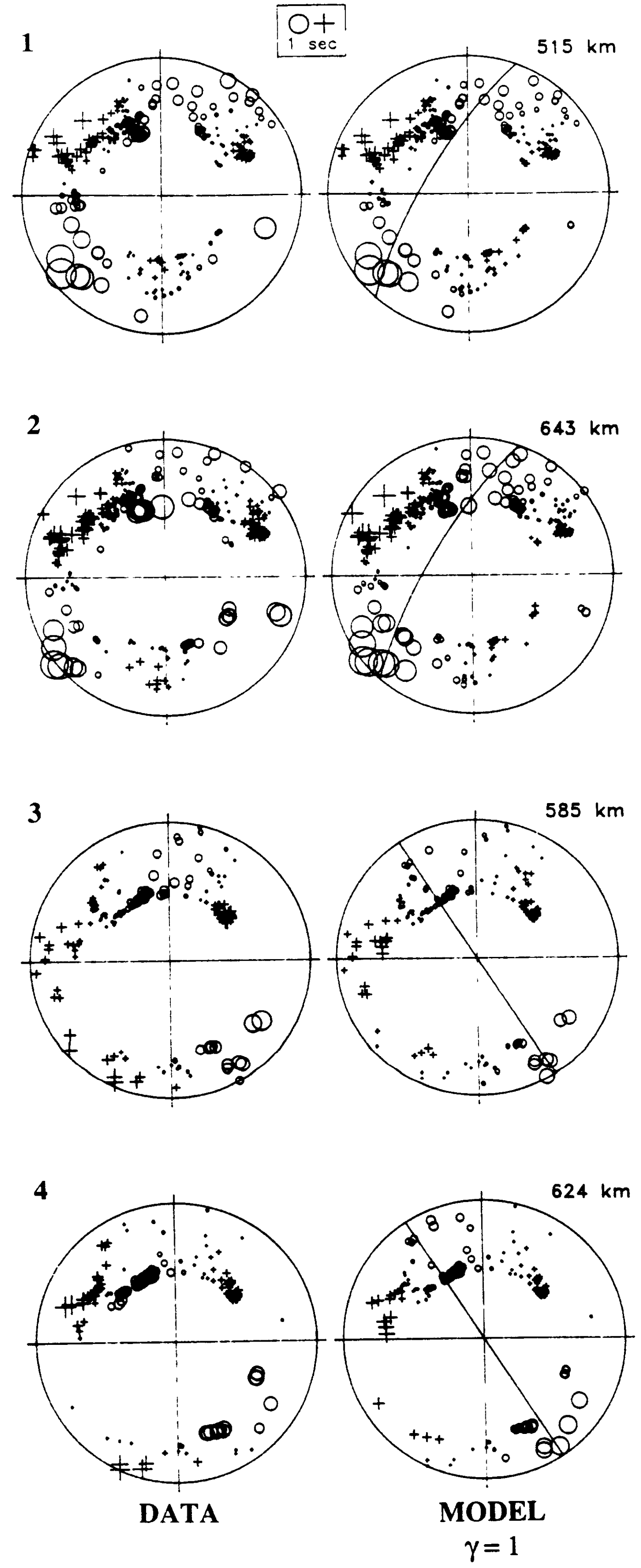

Figure 2.2

Figure 2.3. Lines of constant Γ for the subduction flow model of equation 2.2. Case illustrated is the vertical Mariana slab, for a thickening factor $\gamma = 2$ over a depth range $\zeta = 150$ km. The only streamlines shown are for diverging particle paths inside a nominal initial slab width $x_1 = 100$ km at $z_2 = 580$ km.

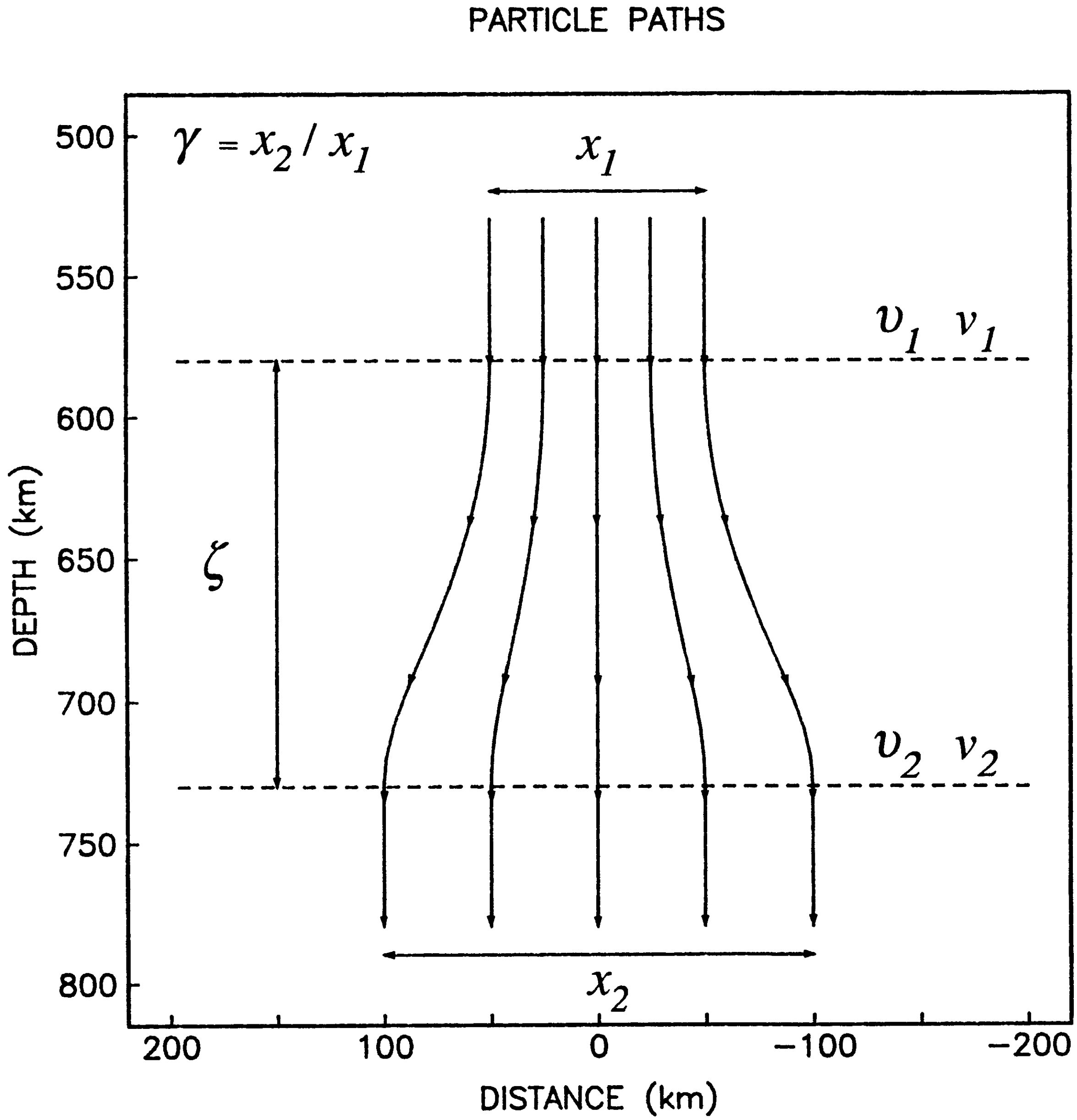
PARTICLE PATHS
$\gamma = x_2 / x_1$
x_1
x_2
v_1 ν_1
v_2 ν_2
ζ
500
550
600
650
700
750
800
DEPTH (km)
200
100
0
−100
−200
DISTANCE (km)

Figure 2.3

Figure 2.4. Isotherms for Kuril slab models obtained by the finite difference calculations described in the text. A divergent flow with thickening factor γ is imposed between $z_1 = 580$ km and $z_2 = z_1 + \zeta$; streamlines for this flow conform to equation 2.2. Results for $\gamma = 1, 2,$ and 4 with ζ held fixed at 150 km are on left; those for $\zeta = 150, 450,$ and 750 km with $\gamma = 3$ are on right. Contour interval is 200°C; depth scale is in kilometers with no vertical exaggeration.

Figure 2.4

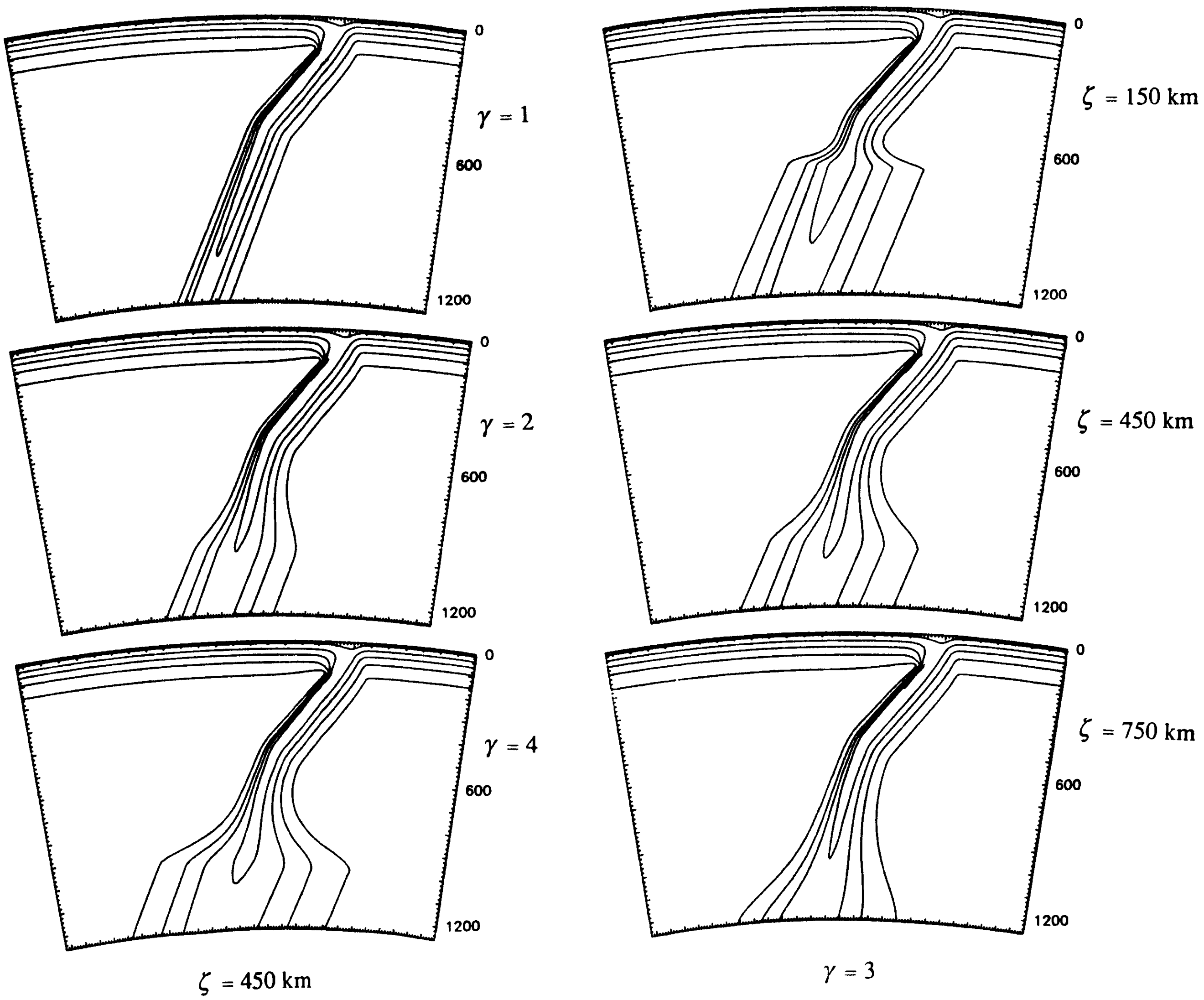

0
γ = 1
600
1200
0
γ = 2
600
1200
0
γ = 4
600
1200
ζ = 450 km
0
ζ = 150 km
600
1200
0
ζ = 450 km
600
1200
0
ζ = 750 km
600
1200
γ = 3

Figure 2.5. Curves of unrelocated and unsmoothed theoretical travel time residuals calculated by ray-tracing through models where $\zeta = 150$ km and $\gamma = 1$ (solid line) or $\gamma = 4$ (dashed line). The two negative troughs in each plot correspond to rays which have traveled substantial distances down and along the slab plane. Ray path perturbations due to slab heterogeneity were ignored in the top panel, where the thick slab produces negative anomalies that are wider by a factor of three than the thin slab. Including three-dimensional ray bending (bottom panel) affects the width of the negative troughs for the wide slab very little but substantially widens those for the narrow slab. This effect explains why the residual sphere data are relatively insensitive to slab width.

Figure 2.5

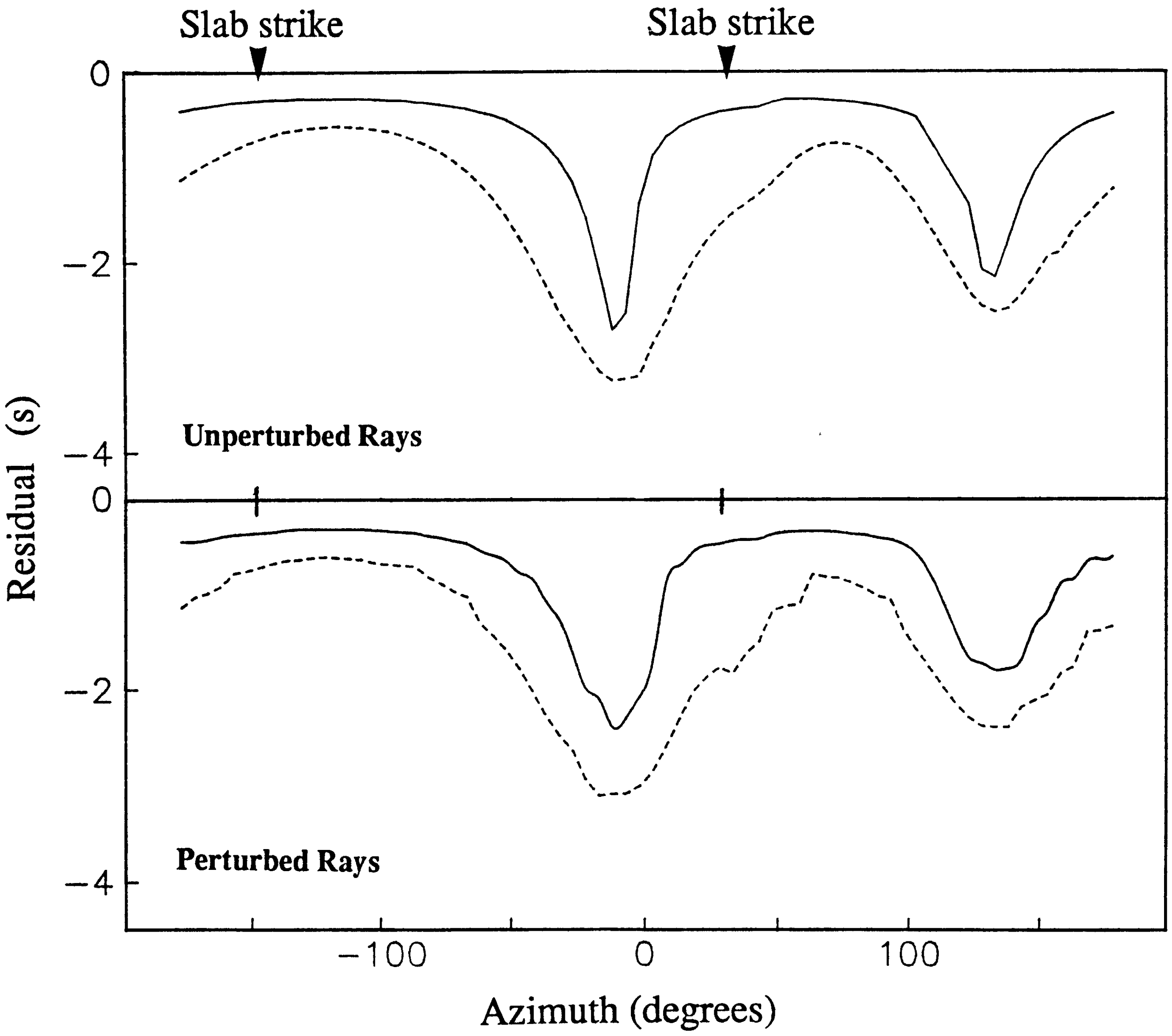
Slab strike
Slab strike
0
−2
−4
0
−2
−4
Residual (s)
Unperturbed Rays
Perturbed Rays
−100
0
100
Azimuth (degrees)

Figure 2.6. Contours of variance reduction calculated according to equation 2.1 for Kuril events 1 (left panel) and 2 (right panel). Vertical axis is the depth interval ζ; the horizontal axis is the thickening factor γ. Contour interval is 2%. The shaded area corresponds to the models whose variance reductions are significantly less at the 90% confidence level than a model with 10 degrees of freedom, the criterion we use to indicate unacceptable fits to the data.

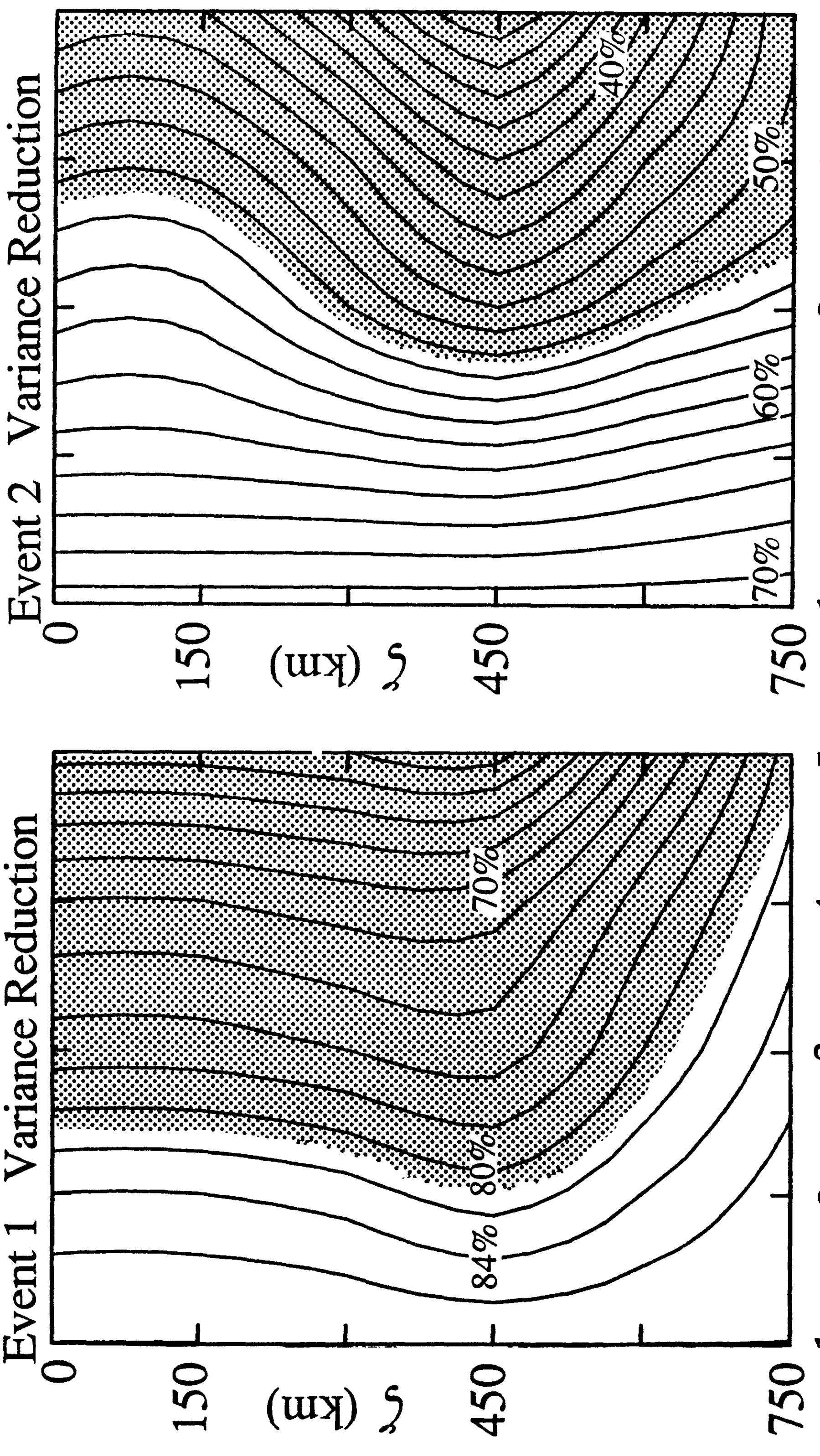
Event 2 Variance Reduction
70%
60%
50%
40%
ζ (km)
0
150
450
750
γ
1
2
3
4
5
Event 1 Variance Reduction
84%
80%
70%
ζ (km)
0
150
450
750
γ
1
2
3
4
5

Figure 2.6

Figure 2.7. Plots of corrected, relocated, and smoothed travel time residuals as a function of azimuth on the residual sphere for Kuril event 1. Lower panel is the residual sphere data for event 1 (same as data residuals in Figure 2.2). Travel time residuals in the other panel are the difference between the data and the theoretical times calculated for slab models where ζ is held fixed at 150 km and $\gamma = 1$, 3, and 5. Upper panel corresponds to the Kuril slab model of Figure 2.1; points are identical to model residuals in Figure 2.2. Variance reduction for each model is shown in the upper right corner of their frame; models for $\gamma = 1$ and 3 produce acceptable fits; $\gamma = 5$ does not.

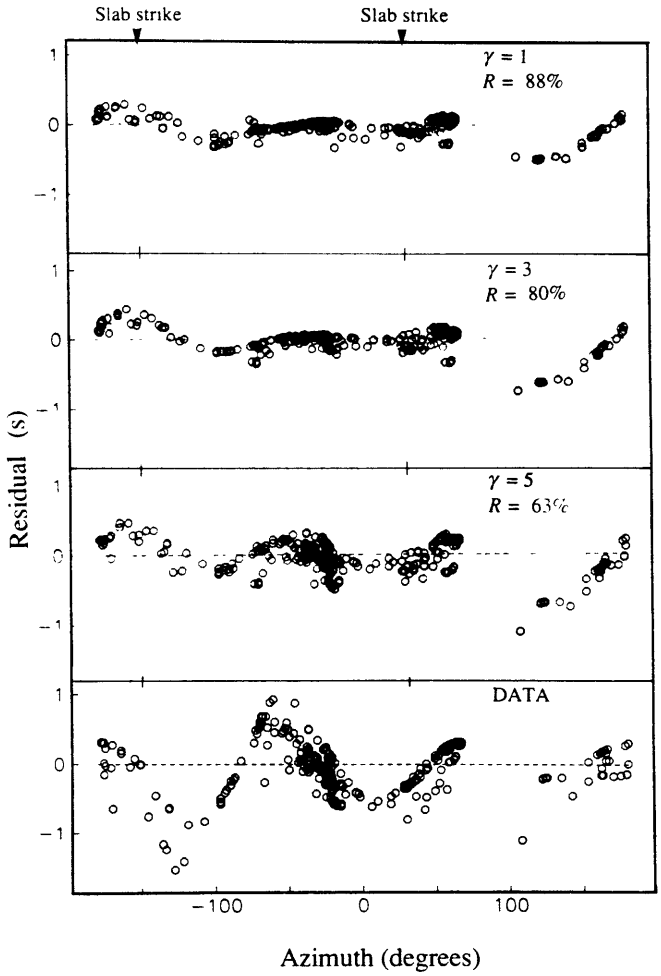
Slab strike
Slab strike
γ = 1
R = 88%
γ = 3
R = 80%
γ = 5
R = 63%
DATA
1
0
−1
Residual (s)
−100
0
100
Azimuth (degrees)

Figure 2.7

Figure 2.8. Plots of corrected, relocated, and smoothed travel time residuals as a function of residual sphere azimuth for Kuril event 1. The upper and lower panels are identical to those of Figure 2.7; the former corresponds to the best fitting slab model of Figure 2.1, which has a strike of 31° and a dip of 72°. The middle panels correspond to models where $\gamma = 1$ (no advective thickening) and the strike and dip vary from their best fitting values; in the second panel the dip is decreased to 62°, and in the third the strike is decreased to 21°. These variations produce unacceptable fits to the data.

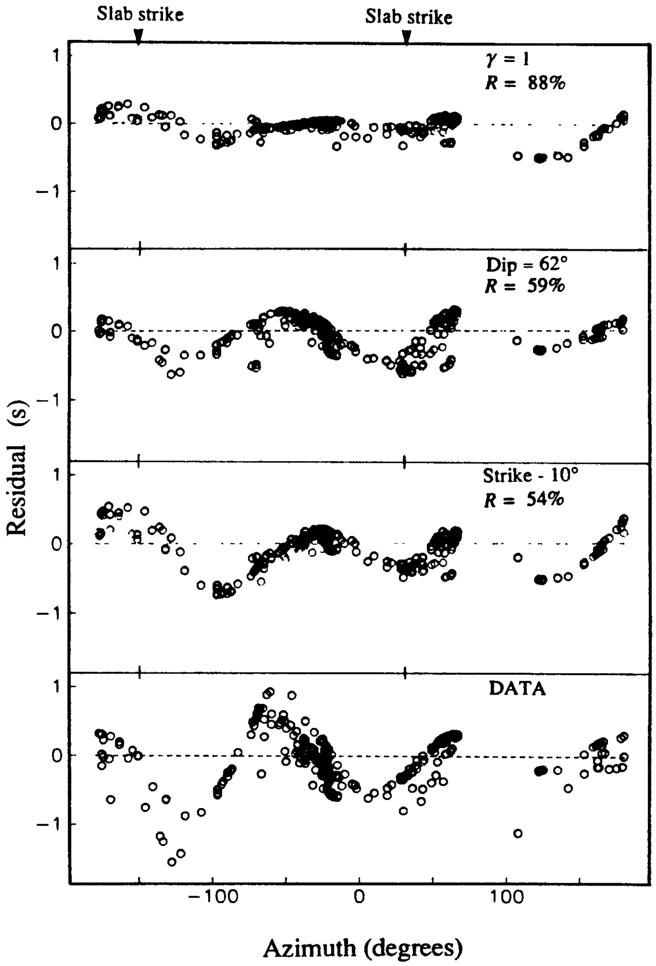
Slab strike
Slab strike
γ = 1
R = 88%
Dip = 62°
R = 59%
Strike - 10°
R = 54%
DATA
Residual (s)
1
0
−1
−100
0
100
Azimuth (degrees)

Figure 2.8

Figure 2.9. (Top) Contours of variance reduction calculated according to equation 2.1 for Kuril event 2. Vertical axis is the thickening factor γ; horizontal axis is slab penetration depth. $\zeta = 150$ km for all models. Contour interval is 2%. The shaded area corresponds to the models whose variance reductions are significantly less at the 90% confidence level than a model with 10 degrees of freedom, the criterion we use to indicate unacceptable fits to the data. For models extending below 900–1000 km variance reduction is good, but it falls off for models ending much above this depth. (Bottom) Contours of $\partial v_p/\partial T$ obtained from the least squares fit of the model residual spheres to the data. $\partial v_p/\partial T$ increases rather dramatically as slab length shortens above 900 km; the shaded area corresponds to values of $\partial v_p/\partial T$ greater than -1.0 m/s/°K, considered to be unacceptably large on the basis of other data (see text).

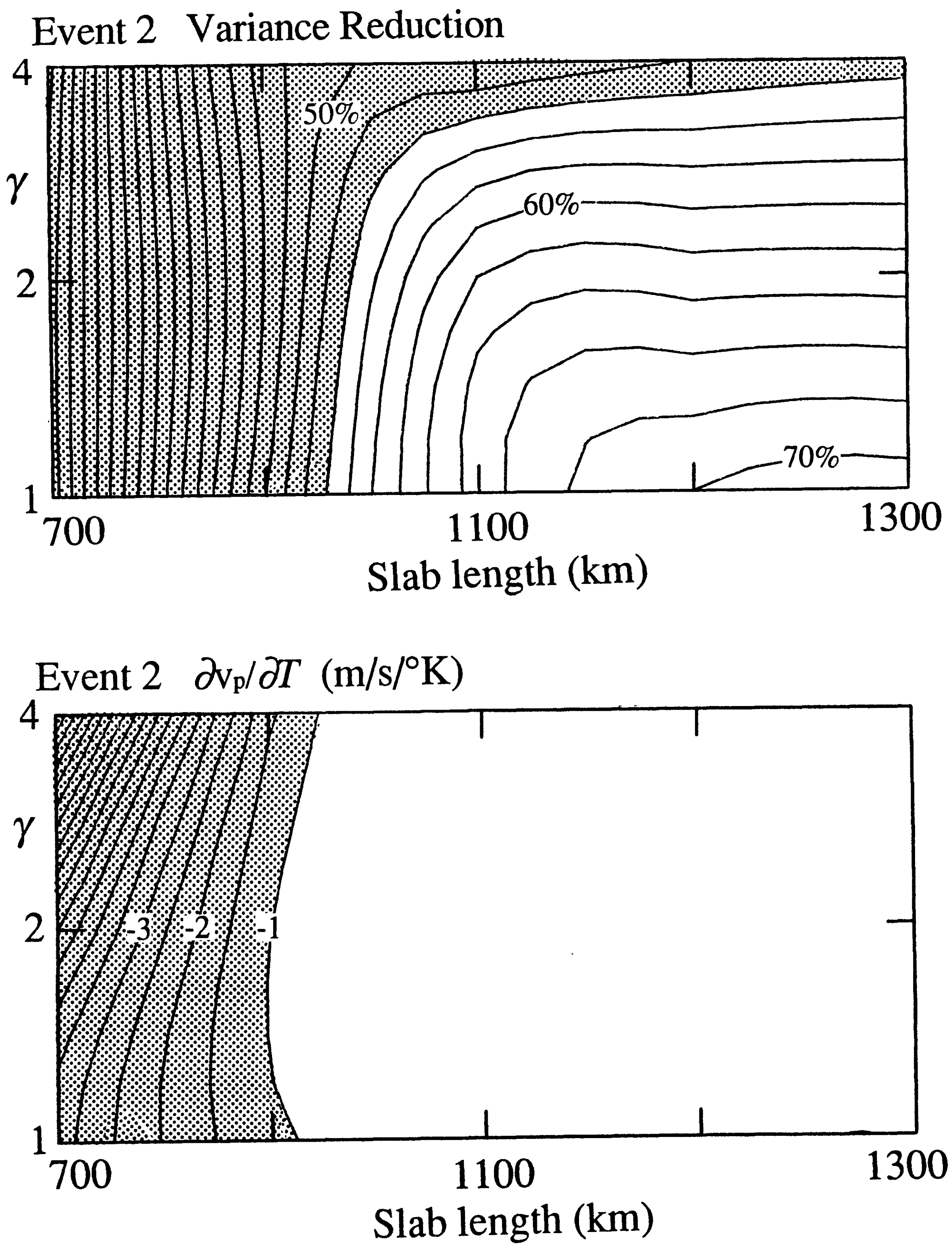
Event 2 Variance Reduction
4
γ
2
1
50%
60%
70%
700
1100
1300
Slab length (km)
Event 2 $\partial v_p/\partial T$ (m/s/°K)
4
γ
2
1
-3
-2
-1
700
1100
1300
Slab length (km)

Figure 2.9

Figure 2.10. Contours of variance reduction calculated according to equation 2.1 for Mariana events 3 (left panel) and 4 (right panel). Vertical axis is the depth interval ζ; the horizontal axis is the thickening factor γ. Contour interval is 2%. Comparison with Figure 2.6 shows that the constraints on γ are much weaker than in the Kurils; no points on this plot have variance reductions that are significantly worse at the 90% confidence level than a model with 10 degrees of freedom. Hence for these events, a γ of at least 5 is acceptable.

Figure 2.10

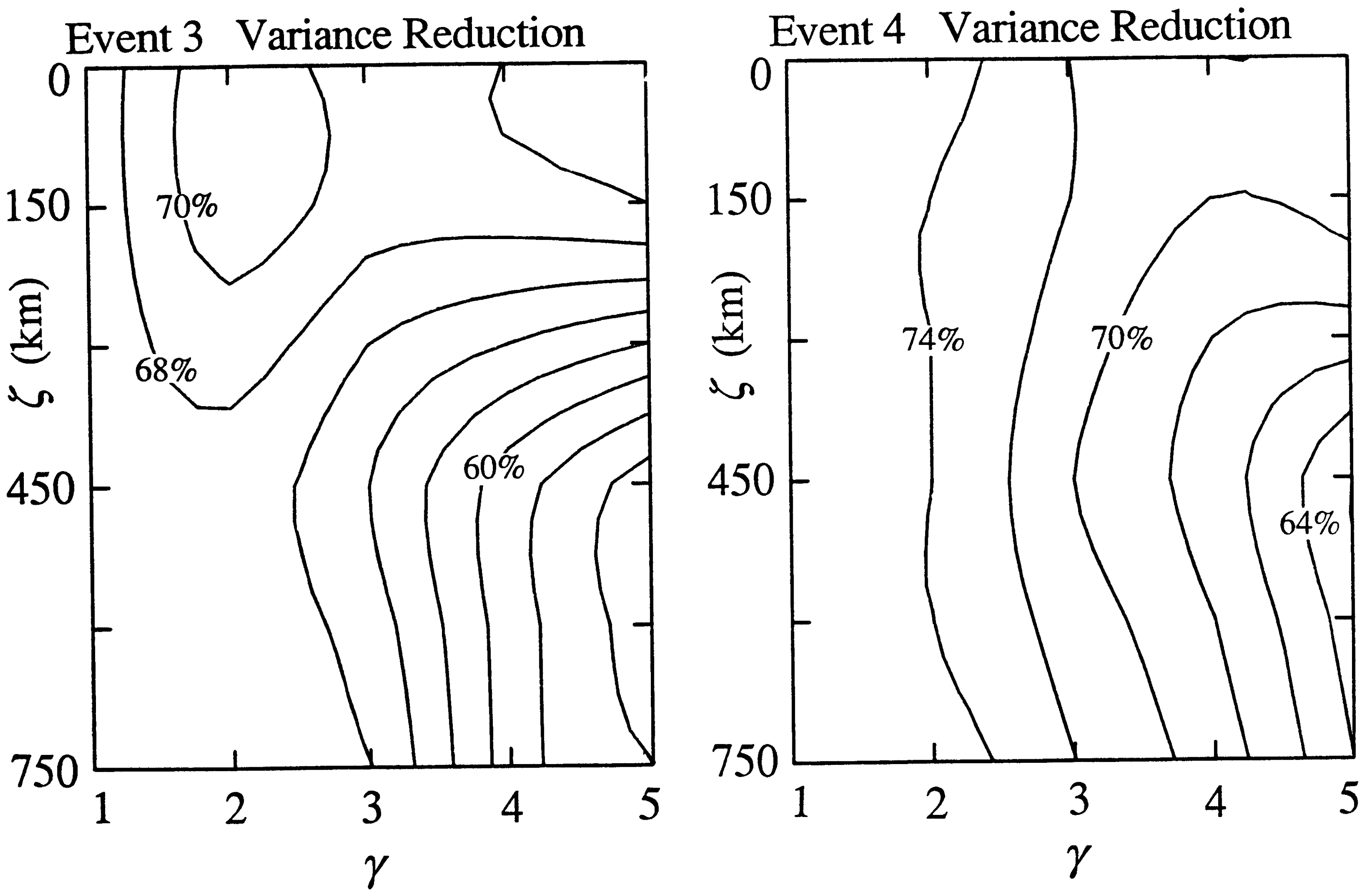
Event 3 Variance Reduction
Event 4 Variance Reduction
ζ (km)
0
150
450
750
γ
1
2
3
4
5
70%
68%
60%
74%
70%
64%

Figure 2.11. (Top) Contours of variance reduction calculated according to equation 2.1 for Mariana event 4. Conventions same as in Figure 2.9. For slab models extending below 800–900 km, the variance reduction is acceptable, but it degrades quickly for shallower penetration depths. (Bottom) Contours of $\partial v_p/\partial T$ obtained from the least squares fit of the model residual spheres to the data. $\partial v_p/\partial T$ increases rapidly as slab length shortens above 900 km; the shaded area corresponds to values of $\partial v_p/\partial T$ greater than −1.0 m/s/°K, considered to be unacceptably large on the basis of other data (see text).

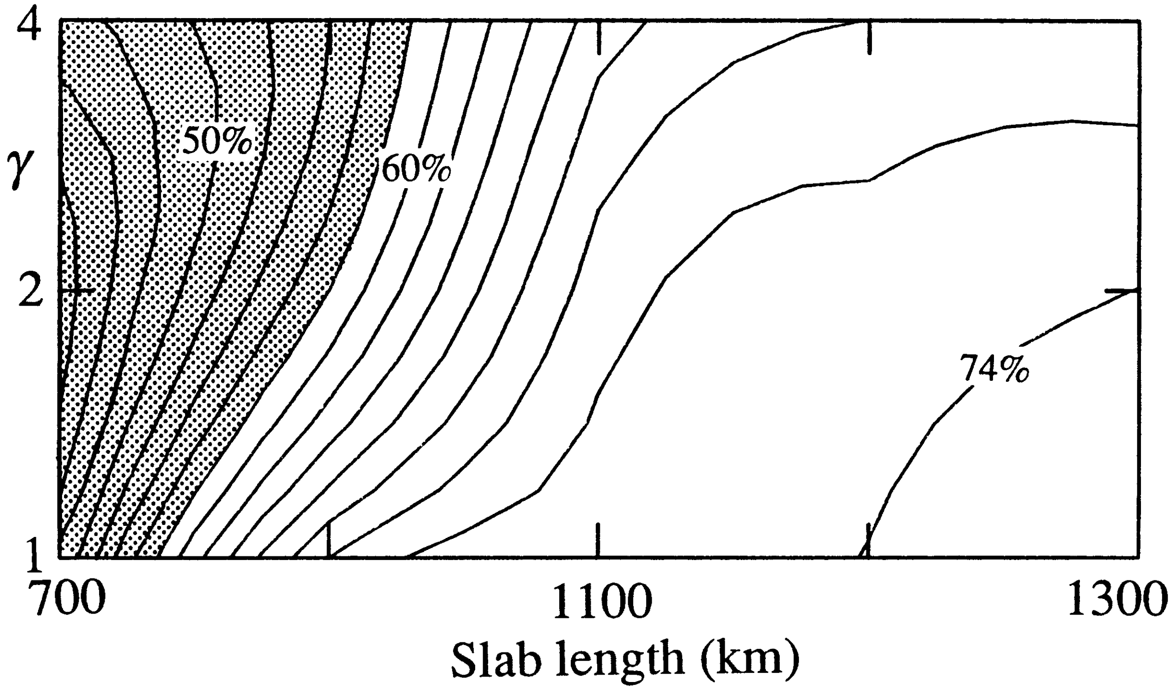

Event 4 Variance Reduction

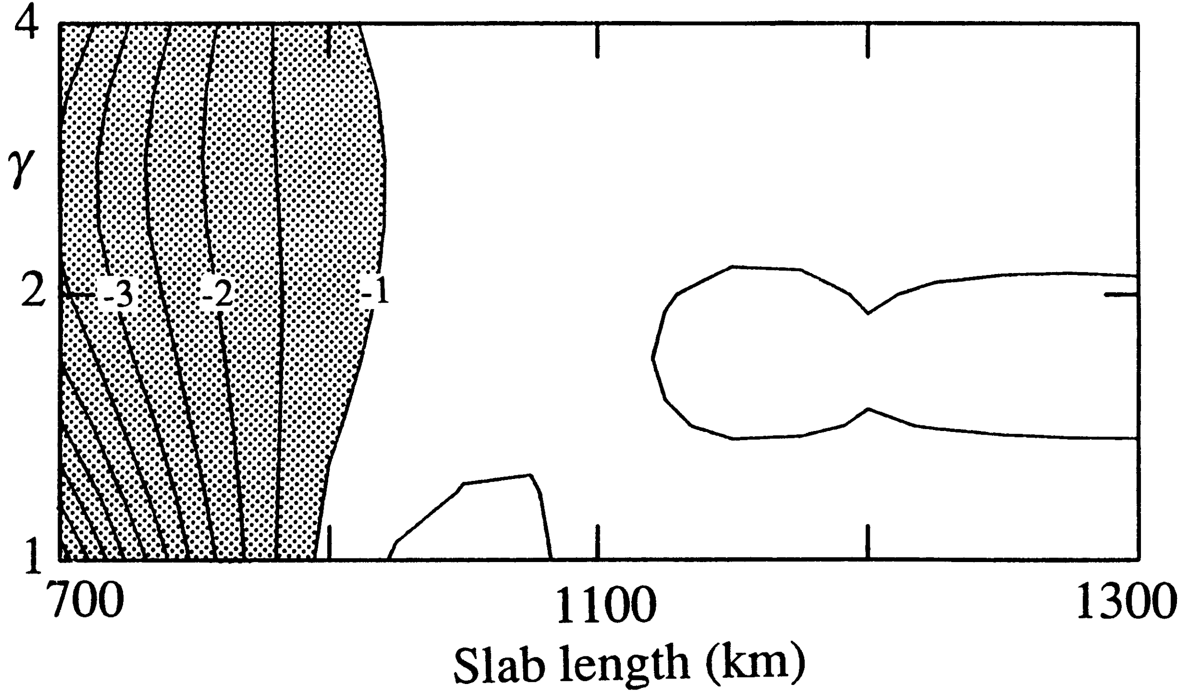

Event 4 $\partial v_p/\partial T$ (m/s/°K)

Figure 2.11

CHAPTER 3

MAPPING THE TONGA SLAB

INTRODUCTION

Since the pioneering studies which first identified dipping planes of seismicity with downgoing lithospheric slabs [*Sykes,* 1966; *Isacks et al.* 1969; *Isacks and Molnar,* 1971] the distribution of subduction zone earthquakes has been used to infer slab geometry and extent and often to characterize mantle flow. However, seismicity fundamentally provides information on seismic strain release within the lithosphere, not on its structure, and a lack of intermediate- and deep-focus earthquakes cannot be taken to indicate the absence of a subducted slab. In particular, *Jordan* [1977] and *Creager and Jordan* [1984] found that residual sphere analysis of seismic travel time data from the Kuril-Kamchatka arc required aseismic extension of the slab several hundred kilometers into the lower mantle. Subsequent residual sphere studies [*Creager and Jordan,* 1986; *Fischer et al.,* 1988] documented penetration of slab velocity anomalies to depths of at least 900 km beneath the Mariana and Japan arcs, as well as Kuril-Kamchatka, while showing that the slab may substantially widen as it enters the lower mantle, a point discussed more thoroughly in Chapter 2. Several regional tomographic studies substantiate these findings in whole [*Jordan and Lynn,* 1974; *Grand,* 1987; *Kamiya et al.,* 1988] or in part [*Zhou and Clayton,* 1988], and lithospheric extension into the lower mantle is consistent with recent attempts to model wave propagation through the deep slab [*Vidale,* 1987; *Vidale and Garcia-Gonzalez,* 1988; *Cormier,* 1988; *Engdahl et al.,* 1988] as well as global tomography [*Dziewonski and Woodhouse,* 1987]. The detection of aseismic slabs below deep-focus zones argues for deep circulation as a component of plate-tectonic return flow and against the hypothesis that the mantle is stratified into two convecting systems with a sharp chemical boundary near the 650-km seismic discontinuity [*Jordan et al.,* 1988].

In this study we map the geometry and extent of the Tonga slab using residual sphere analysis of deep- and intermediate-focus earthquakes from all latitudes along the arc. The abundant seismicity which characterizes subduction in Tonga allows for a finer resolution of slab structure than was possible in any of the other arcs examined so far with the residual sphere method. Furthermore, the shape of the downgoing seismicity is far from a simple plane and its complexities, along with focal mechanisms and moment tensor data, have generated numerous models of slab morphology and speculations on mantle flow [*Sykes,* 1966; *Billington and Isacks,* 1975; *Hanus and Vanek,* 1978; *Richter,* 1979; *Billington,* 1980; *Louat and Dupont,* 1972;*Giardini and Woodhouse,* 1984, 1986; *Hamburger and Isacks,* 1987]. Applying the residual sphere method in Tonga allows us to compare contortions in the seismicity to slab structure as constrained by real data, resolving the aseismic as well as seismic regions of the slab and giving a fuller picture of lithospheric deformation.

Of primary importance is whether the Tonga slab extends into the lower mantle. Since *Davies and McKenzie* [1969] first documented the effects of large-scale slab structure on travel times observed from subduction zone earthquakes, numerous authors have analyzed travel time and amplitude signals from Tonga events in an attempt to further quantify the seismic properties and extent of the downgoing slab [*Toksöz et al.*, 1971; *Mitronovas and Isacks,* 1971; *Barazangi et al.,* 1972; *Sleep,* 1973; *Engdahl,* 1975; *Billington and Isacks,* 1975; *Engdahl et al.,* 1977; *Fitch,* 1975, 1977; *Isacks and Barazangi,* 1977; *Sondergeld et al.*, 1977; *Frolich and Barazangi*, 1980; *Huppert and Frohlich,* 1981; *Bock,* 1981; *Bock and Ha,* 1984; *Ansell and Gubbins,* 1986; *Bock,* 1987]. Of these, travel time studies involving ray paths from deep- and intermediate-focus events hold the most promise for determining the depth to which the slab extends, but to date their conclusions vary widely. *Fitch* [1975, 1977] and *Frolich and Barazangi* [1980] favor high velocity material extending below the deepest events, while *Sondergeld et al.* [1977], *Bock* [1981] and *Ansell and Gubbins* [1986] do not.

A second question we address is the character of slab deformation in the transition zone. If the Tonga lithosphere bends to a steeper dip below 500 km as is the case in the Japan and Kuril-Kamchatka arcs [*Creager and Jordan,* 1986; *Kamiya et al.*, 1988] it indicates that downward curvature is not restricted to the northwest Pacific and must be explained in models of slab dynamics such as *Garfunkel et al.* [1986], *Kincaid and Olson* [1987], *Gurnis and Hager* [1988], and *Hsui et al.* [1988]. Furthermore, considerable evidence suggests that the Tonga slab encounters resistance to subduction with depth, particularly in the vicinity of the 650-km discontinuity. The deep Tonga seismic zone accounts for nearly 70% of the Earth's deep seismicity and a very large release of seismic energy [*Richter,* 1979]. In addition, earthquakes occuring below 400 km generally indicate down-dip compression [*Isacks and Molnar, 1971; Vassiliou,* 1984; *Giardini and Woodhouse,* 1984]. These results may indicate that the slab is slowing and laterally deforming, perhaps due to an increase in mantle viscosity. In this study we examine whether travel time data in Tonga are consistent with advective thickening perpendicular to slab strike as they are in Kuril-Kamchatka and the Marianas [*Fischer et al.*, 1988].

Finally we investigate the correlation between our slab structure as inferred from travel time data in Tonga and several of the more prominent features in the seismicity. At the present-day Tonga trench (Figure 3.1), the Pacific plate is subducting at an azimuth slightly north of west under the Australian shield at roughly 10 cm/yr, with both plates are moving northward with respect to the mantle at 5 cm/yr [*Minster and Jordan,* 1978]. Seismicity extends down-dip from the trench to depths of 700 km (Figure 3.2). At its northern end, the curvature of the deep seismicity tightens, bending westward away from the east of north strike observed at intermediate depths and elsewhere along the arc [*Sykes,* 1966; *Billington,* 1980; *Giardini and Woodhouse,* 1984; *Hamburger and Isacks,* 1987]. Other anomalous features in northern Tonga (13° -19° S) include a diffuse band of well-located deep events which lie at least 100 km to the southwest of the main seismic zone [*Billington and Isacks,* 1975; *Billington,* 1980; *Giardini and Woodhouse,* 1984; *Hamburger and Isacks,* 1987], and a pronounced "bench" in the dip of the seismicity between 300 km and 450 km depth [*Isacks and Barazangi,* 1977; *Billington,* 1980; *Giardini and Woodhouse,* 1984]. By contrast, central Tonga (19°- 21.5° S) seismicity is relatively planar, but events in southern Tonga delineate a plane which bifurcates into two parallel bands at around 500 km [*Billington,* 1980; *Giardini and Woodhouse,* 1984]. The Louisville Ridge, an aseismic seamount chain [*Larson and Chase,* 1972], marks the southern end of the Tonga arc where it intersects the trench at 25° S; a pronounced bend in both seismicity and trench topography are observed at this latitude [*Karig,* 1970; *Billington,* 1980]. While some authors attribute these complexities to past tectonic interactions at the Earth's surface [*Isacks and Barazangi,* 1977; *Billington,* 1980], others believe they reflect resistance to penetration of slab material at the top of the lower mantle [*Giardini and Woodhouse,* 1984, 1986] or some combination of both alternatives [*Hamburger and Isacks,* 1987]. By constructing structural models for the slab we intend to shed light on this debate.

RESIDUAL SPHERE ANALYSIS

Real and synthetic data

The residual sphere projection was introduced by *Davies and McKenzie* [1969] to examine the teleseismic travel time signature of downgoing slabs. It displays travel time anomalies as a function of station azimuth and take-off angle from the earthquake on the lower focal hemisphere, emphasizing the near-source features in the data. Residual sphere analysis as developed by *Jordan* [1977] and *Creager and Jordan* [1984] is essentially a way of evaluating slab models by comparing the synthetic travel times they produce with the real travel time data observed for individual subduction zone events. In order to make this comparison, we first extract the near-source, or slab, travel time component from both real and synthetic datasets.

The isolation of the near-source component may be described as a series of corrections and operators applied to the data:

$$\Delta \mathbf{t_d} = \mathbf{C'}\ \mathbf{Q}\ (\ \mathbf{Dt_d} - \mathbf{c_S} - \mathbf{c_M} - \mathbf{c_R} - \mathbf{c_E}\ ) \qquad (3.1)$$

$$\Delta \mathbf{t_s} = \mathbf{C'}\ \mathbf{Q}\ (\ \mathbf{Dt_s} - \mathbf{c_R}\ ) \qquad (3.2)$$

$\Delta\mathbf{t_d}$, $\Delta\mathbf{t_s}$, $\mathbf{t_d}$, and $\mathbf{t_s}$ are the real and synthetic reduced times, and the real and synthetic raw times, respectively. **C'**, **Q**, and **D** are smoothing, relocation and observation operators, and $\mathbf{c_S}$, $\mathbf{c_M}$, $\mathbf{c_R}$, and $\mathbf{c_E}$ are corrections for station anomalies, lower mantle heterogeneity, radial earth structure and ellipticity. The real data, $\mathbf{Dt_d}$, are *P*-wave arrival times compiled by the International Seismological Centre (ISC) with ray paths bottoming between 800 km ($\Delta \geq$ 30°) and the core-mantle boundary ($\Delta \leq$ 100°). In principal, travel times can be thought of as continuous functions over the surface of the earth, but while $\mathbf{t_s}$ can be computed a continuous spatial function, $\mathbf{t_d}$ is known only at the locations of those stations reporting for the earthquake. **D**, the observation operator, is a vector containing delta functions at the take-off angles and azimuths which correspond to the stations at which which we have real data. Residuals relative to the *Herrin et al.* [1968] radial earth model, are computed and corrected for hydrostatic ellipticity [*Dziewonski and Gilbert,* 1976], and those greater than 5 seconds are discarded. Figure 3.3 illustrates these corrections and operators for an event the ISC locates at 102 km depth in southern Tonga. The raw residuals $(\mathbf{Dt_d} - \mathbf{c_R} - \mathbf{c_E})$ are predominantly strongly negative at azimuths and takeoff angles close to the strike and dip of intermediate-focus southern Tonga seismicity (indicated by the great circle plotted in Figure 3.3a). These times correspond to rays which have traveled at least several hundred kilometers in the plane of the slab, and their presence in the uncorrected data indicates that none of the subsequent operations or corrections applied to the data "creates" the slab anomaly in $\Delta\mathbf{t_d}$, (Figure 3.3f). Figure 3.4 shows $(\mathbf{Dt_d} - \mathbf{c_R} - \mathbf{c_E})$ for all 25 events we model in this study. While one expects a slab signature in a residual sphere for an earthquake with several hundred kilometers of seismically active slab beneath it, several of the deepest events exhibit strong anomalies with similar orientations, giving a preliminary suggestion that the slab extends below the seismicity.

($\mathbf{Dt_d} - \mathbf{c_R} - \mathbf{c_E}$) are corrected for two further types of large-scale aspherical heterogeneity: $\mathbf{c_S}$, $\mathbf{c_M}$ are corrections for mean station anomalies [*Dziewonski and Anderson,* 1983] and the L02.56 lower-mantle structure [*Dziewonski,* 1984]. (See Figures 3.3b, 3.3c and 3.3d for examples).

The theoretical times, $\mathbf{t_s}$, are generated by tracing rays through a three-dimensional slab model, assuming the hypocenter is located at the ISC depth; lateral position within the slab is constrained by the location of the individual earthquake relative to the overall seismicity in its particular arc segment. Ray paths and travel times within the slab structure are computed following the algorithm of *Creager* [1984] which includes the effects of three-dimensional ray-bending, and ray tracing in the radial Earth outside the near-source region is accomplished with the fast spline method of *Cerveny and Jansky* [1983]. Multiplying $\mathbf{t_s}$ by $\mathbf{D}$ yields synthetic residuals at those locations (for an example see Figure 3.3g). Later in the chapter we show plots of synthetic travel times as a continuous function of station take-off angle and azimuth from the source, but in general, any residuals shown will be either $\Delta \mathbf{t_d}$ or $\Delta \mathbf{t_s}$, unless otherwise specified.

Q

Subduction zones contain large lateral velocity heterogeneity in the form of the slab which, along with other aspherical structure will intoduce bias into earthquake locations referenced to radial models [*Mitronovas and Isacks,* 1971; *Fujita et al.,* 1981; *Nieman et al.,* 1986]. The projection operator $\mathbf{Q}$ (defined in equation 2.4 of *Creager* [1984]) accounts for bias in the travel times due to mislocation of the original ISC hypocenter by eliminating any travel time anomalies that can be parameterized as a hypocentral relocation or origin-time shift; formally, this relocation procedure is a projection of the N-dimensional residual vectors into an (N-4)-dimensional subspace orthogonal to the discretized and weighted residual sphere harmonics of zeroth and first degree. In practice we relocate an earthquake by a weighted least-squares minimization of its corrected real or synthetic residual vector and recompute the travel times with respect to the new location. Relocation vectors for the theoretical times are 0 to 25 km in length and oriented in a direction roughly down the dip of the particular slab model, similar to those obtained for synthetic data from Kuril-Kamchtaka slab models [*Creager*, 1984]. However, this operation should not be confused with an attempt to obtain a location which is more accurate in a physical sense than the ISC hypocenter. By removing any residuals that could be due to a shift in event time or location, we also subtract the effects of real lateral heterogeneity whose expression on the residual sphere is contained in the discretized and weighted monopolar and dipolar terms, overestimating the mislocation bias and underestimating the slab anomaly. Our interest, however, lies not in more accurate earthquake locations, but in a bias-free comparison of the real and synthetic times.

C'

C' filters the residual spheres by applying an operator whose spectrum tapers smoothly to zero for harmonics of high angular degree. Applying this smoothing operation to the observed times increases the signal-to-noise ratio of near-source heterogeneity by preferentially damping random observational errors and heterogeneities far from the source, whose spectra on the residual sphere are shifted to high wavenumbers (Figure 3.3f). Applying it to the theoretical times accounts for the bias in the spectrum of near-source heterogeneity introduced by smoothing the data (Figure 3.3i).

Event 17 (located in southern Tonga) contains a good example of the type of high-frequency feature removed by **C'**. A group of positive times is embedded in the negative slab anomaly of the raw residual sphere (Figure 3.3a) near 280° azimuth and at a relatively steep take-off angle. These residuals remain positive, though somewhat diminished in amplitude, throughout the processing, until they are smoothed out with the application of **C'**.

Such high-frequency features are not predicted by a smooth near source structure, such as the slab model which produces the analagous synthetic times in Figure 3.3h. We attribute the high frequency signal to distant lateral heterogeneities we have not adequately corrected for. This particular anomaly appears to be due to a very localized upper mantle anomaly not accurately accounted for in the station correction. Four out of the five stations comprising the slow feature for event 17, Songkhla, Thailand (SNG), Pak Chong,Thailand (PCT), Chiang Mai, Thailand (CHG) and Hong Kong (HKC) also report relatively positive times whenever they appear in other residual spheres (Figure 3.4). Bhumibol Dam, Thailand (BDT) is more variable. Other "slowspots" in the predicted slab field are harder to explain, however. Many of the deep earthquake residual spheres have non-slab-predicted slow times at azimuths slightly east of north (event 23 in Figure 3.4 is a particularly good example), but others with the same stations do not (event 24). Since the appearance of this "slowspot" also has no apparent correlation with event magnitude, nor are these phases necessarily emergent, the positive travel times are probably not due to innaccurate picking of the arrival-time.

In addition to removing high frequency features from the real residuals, C' diminishes the steep gradient travel time observed for down-dip raypaths (Figures 3.3d and 3.3e). Given that this gradient is of primary importance in constraining which slab models fit the data, an obvious question is whether our particular choice of smoothing operator biases our estimates of the various slab parameters. In order to address this concern, we investigate smoothing operators which allow more degrees of freedom in the solutions for the observed or theoretical times.

Two parameters which are critical in the description of the smoothing operator are α and κ.. C' may be written as $C_{ss}(C_{ss} + \alpha C_{nn})^{-1}$ where C_{nn} is the diagonal noise covariance matrix with elements $\sigma_{nj} = (\sigma_{ej} + \sigma_{pj})^{-1/2}$; σ_{ej} is the reading error for the jth station, and σ_{pj} is the estimation error associated with the jth station anomaly [*Creager and Jordan* , 1984]. C_{ss} is the $N \times N$ smoothing matrix whose components are given by equation 23 of *Creager and Jordan* [1984]. The variable α parametizes a trade-off curve (*Backus & Gilbert*, 1970) between the data misfit and solution roughness. Smaller values of α allow more degrees of freedom. κ determines the half width of the low pass filter kernel contained in C_{ss} (Equation 22, *Creager and Jordan*, [1984]). The smoothing operator typically employed in residual sphere studies [*Creager* 1984; *Creager and Jordan*, 1984] assumes $\alpha = \lambda\ 10^{-5}$ and $\kappa = 2.8$ where λ is the largest eigenvalue of the weighted smoothing operator $C_{nn}^{-1/2}\ C_{ss}\ C_{nn}^{-1/2}$. In this study we define an intermediate filter which assumes $\alpha = \lambda\ 10^{-14}$ and $\kappa = 1.0$ in order to maintain a larger down-dip gradient in the residuals. While relocated times smoothed with the standard operator are defined above as $\Delta \mathbf{t_d}$ or $\Delta \mathbf{t_s}$, those smoothed with the intermediate operator are denoted $\Delta \mathbf{t_d}'$ and $\Delta \mathbf{t_s}'$. Comparisons of the standard and intermediate operators and their effects on parameter estimation will be discussed later in the chapter.

MODELING THE SLAB

Slab geometry and extent

Our criterion for evaluating the fit of a model to the data is the variance reduction factor

$$R = 1 - \|\Delta \mathbf{t_d} - \Delta \mathbf{t_s}\|^2 / \|\Delta \mathbf{t_d}\|^2 \qquad (3.3)$$

We invert the data in order to maximize R by adjusting the parameters of the slab model, which include the local strike, dip, length, deep slab width and the amplitude of the velocity anomaly. In addition, we investigate a range of slab morphologies which advectively deform in the plane of the slab at depths of 500 km or more. *Creager and Jordan* [1984, 1986] exclusively employed models which extended undeformed from the upper to lower mantle; here we include structures which smoothly thicken in response to a diverging flow field within the transition zone [*Fischer et al.*, 1988] or which break and imbricate as they penetrate the 650-km discontinuity.

The three-dimensional slab velocity structures we use to model the data originate as two-dimensional, entrained flow profiles where particle paths at shallow depths (< 500 km) are constrained to be parallel to a specified surface and the shear normal to this surface is minimized. An error-function thermal profile corresponding to the age of the lithosphere is used to initialize the finite-difference algorithm, which computes the temperature structure of the descending lithosphere by step-wise alternating between mass transport and conductive heating [*Toksöz et al.,* 1973]. The calculation also includes induced corner flow beneath the backarc region. This choice of initial thermal structure yields a shallow slab width on the order of 100 km, a value consistent with the travel times and waveform frequency content of observed seismic phases which travel from hypocenters at all depths upwards through, or near, the slab [*Barazangi et al.,* 1972; *Ansell and Gubbins,* 1986; *Prasad and Bock,* 1987].

Slab width at depth (below 500 km) depends on the type and scale of lateral advection imposed on the flow field in the transition zone. If slab flow remains parallel to its shallow trajectory (as in *Creager and Jordan* [1984, 1986]), the slab thermal anomaly will thicken only due to conduction, increasing in width by at most 20% from its initial surface value. The flow parametrization of *Fischer et al.* [1988], however, thickens the slab by a specified factor over a given depth range by smoothly increasing horizontal flow velocity at the expense of vertical flux. This flow field is described more fully in chapter 2. The third mode of deformation we examine is characterized by laterally offset slab fragments; as the slab reaches the 650-km discontinuity it breaks, and as its lower portion translates horizontally relative to the shallow lithosphere in the plane of the slab profile, downward migration of both segments continues.

The three-dimensional structure of the Tonga slab is specified by rotating the two-dimensional model around a pole so that the curvature of the slab matches the seismicity local to the earthquake being modeled. Varying the strike of the slab is accomplished by shifting the location of the pole while maintaining it at a constant distance from the event. Approximating non-arcuate subduction zone like Tonga with a constant curvature slab obviously may lead to inconsistencies in slab strike between models for different regions. However, the best-fitting strike value for a given earthquake is heavily weighted by structure very near the source and may be considered a local estimate of strike and curvature in a more complex, undulating structure.

Unless otherwise specified, the slab models in this study have velocity anomalies persisting to about 1300 km depth, although constraints on slab length provided by the Tonga travel time data will also be examined. *Creager and Jordan* [1984, 1986] showed that for the deepest foci in the northwestern Pacific, extending the slab model to depths arbitrarily greater than about 1000 km does not change the theoretical patterns, so that extensions below this depth cannot be resolved by the data. However, decreasing slab length above 900 to 1000 km does significantly degrade the data-model fit, a result confirmed by *Fischer et al.* [1988] for slab models which undergo considerable advective thickening in the transition zone.

The thermal coefficient of velocity

A final slab parameter, $\partial v_p/\partial T$, linearly scales the thermally defined slab models to *P*-wave velocity anomalies. In the study by *Creager and Jordan* [1986], it was determined to be –0.5 ± 0.1 m/s/°K by inverting the data for intermediate-focus earthquakes, which, in the northwest Pacific, are insensitive to how far the slab extends below the seismicity cutoff. This value is consistent with the lower-mantle estimates of *Hager et al.* [1985] and various laboratory studies [*Sumino,* 1979; *Sumino et al.*, 1983; *Suzuki and Anderson,* 1983; *Suzuki et al.,* 1983]. In this study and in *Fischer et al.* [1988], however, $\partial v_p/\partial T$, and hence the amplitude of the slab velocity anomaly, is allowed to vary freely. This approach ensures that $\partial v_p/\partial T$ will not bias our estimates of the other slab parameters, in particular slab length.

Creager and Jordan [1986] investigated the effects that elevation or depression of upper-mantle phase boundaries within the slab have on estimates of $\partial v_p/\partial T$ and other slab paramters. Following their approach we assume that the olivine to spinel phase transformation at 420 km [*Weidner*, 1985] has a Clapeyron slope of 3.5 MPa/°K [*Suito*, 1977, and the spinel to perovskite phase change at 650 km [*Liu*, 1976a,b; *Yagi et al*, 1979; *Ito and Yamada*, 1982] a Clapeyron slope of –2 MPa/°K [*Ito and Yamada*, 1982]. In a typical Tonga slab profile, these values elevate the 420-km phase boundary by up to 100 km (increasing the thermal and velocity anomalies) and depress the 650-km transition by as much as 50 km (diminishing the anomalies). However, these regions of anomalous phase have minimal effect on the synthetic travel time residuals. For intermediate-focus earthquakes, their respective perturbations to travel time largely cancel each other out. For events below 500 km, elevation of the 650-km phase boundary leaves the pattern of residual sphere anomalies intact, and increases the amplitude of $\partial v_p/\partial T$ by less than 10%. This discrepancy is significantly smaller than the scatter in individual $\partial v_p/\partial T$ estimates for each of the 25 modeled earthquakes; these values range from –0.3 m/s/°K to –0.7 m/s/°K. $\partial v_p/\partial T$ values for models with and without phase change are listed in Table 2.

C' and parameter estimation

For Tonga earthquakes, a juxtaposition of smoothed and unsmoothed residual spheres reveals that our typical smoothing operator underestimates the size of the positive to negative gradient in the northwest residual sphere quadrant. Here, as previously promised, we investigate smoothing operators which allow more degrees of freedom in the solutions for the observed or theoretical times in order to determine whether our use of the standard smoothing operator biases our estimates of the various slab parameters. Figure 3.5 demonstrates the effects of various smoothing operators on the data for event 9, a deep-focus earthquake in central Tonga. The left-hand column shows observed travel time residuals; the residual sphere at top has been relocated but not smoothed, while the bottom one has been smoothed with the standard operator (its residuals may be denoted Δt_d); the middle row contains relocated times smoothed with the intermediate filter ($\Delta t_d'$). The intermediate filter with its larger number of degrees of freedom maintains a steeper down-dip gradient, but still diminishes many of the higher wave number travel time patterns. The right hand column of Figure 3.5 contains the relocated theoretical residual spheres for the best-fitting central Tonga slab model with no smoothing (top), the intermediate filter ($\Delta t_s'$, middle row), and the standard filter (Δt_s, bottom). Since the unsmoothed theoretical times define a pattern that is already quite smooth, application of the intermediate and standard filters has relatively little impact.

Despite the enhanced high-frequency content in $\Delta t_d'$ and the unsmoothed times, the slab strike and dip values which fit them best (dip = 59°, strike = 5°) are quite close to the values preferred by Δt_d (dip = 64°, strike = 15°) and in fact almost lie within the Δt_d 90% confidence level of acceptibility. This critical level is calculated for a chi-squared distribution with 10 degrees of freedom, the number of degrees of freedom in the standard smoothing operator, and corresponds to the variance reduction value which will be exceeded with 90% probability by models providing fits to the data equally good as the best-fitting model. Stated differently, a slab dipping at 59° with a strike of 5° explains 62% of the signal in Δt_d while the preferred model (dip = 64°, strike = 15°) achieves a value of 78%; the 90% confidence level correponds to 65%, hence the former model is nearly, but not quite, acceptable. The data for other earthquakes in Tonga also indicate that the best-fitting strike and dip values determined for either $\Delta t_d'$ or the unsmoothed times lie no more than 10° from the strike and 5° from the dip of the model prefered by Δt_d, suggesting that the slab signal produced by smoothing with the standard operator is a fairly accurate reflection of the raw data. Furthermore, since the values preferred by $\Delta t_d'$ and the unsmoothed times are not consistently greater or smaller than those determined with Δt_d, we conclude that the standard smoothing operator is not introducing a systematic bias into the estimation of these parameters. In terms of slab length, since the standard smoothing operator reduces the negative to positive gradient produced by ray paths near the top boundary of the slab, it, if anything, biases our results toward shorter slab models.

MAPPING THE SLAB

The tangent arc approximation

The complex shape of the downgoing seismicity in the Tonga subduction zone suggests that the slab itself may be fairly contorted. Our ultimate goal is to explain the residual sphere travel times from our dataset of 25 deep- and intermediate-focus events (Table 1, Figure 3.2) with one fully three-dimensional lithospheric model, but, in order to minimize the number of free parameters in the infinite variety of possible slab structures, we initially model each earthquake with an undeformed planar slab, that is, a slab which extends at constant curvature and dip and roughly invariant strike from shallow depths into the lower mantle, thickening only slightly as a consequence of thermal conduction. These models represent tangent arc approximations to the true shape of the slab and provide an unbiased estimate of the major structural features throughout the zone. Their variable parameters are slab strike, dip, depth, along-arc extent, and $\partial v_p/\partial T$; we simply incrementally adjust each of them independently of the others until we find the combination which maximizes R, variance reduction.

While the preferred values for strike and dip show considerable variability, constraints on slab length and lateral extent are quite uniform among the 25 earthquakes. With the exception of the intermediate-focus events 1 and 2 whose data are fit best by a slab terminating at 500 km depth, all of the Tongan earthquakes examined acheive their greatest variance reduction with slabs extending to 1000 km or deeper, and the deep focus events require penetration to at least this depth. The residual sphere data for all events are satisfied if the slab extends laterally to roughly where the seismicity terminates in the north (14.5° S), and to where deep-focus activity ceases in the south (27° S).

The best-fitting values for strike, dip, and $\partial v_p/\partial T$ are shown in Table 2. Two trends are immediately apparent. First, the preferred value of slab strike increases from 15° at the northern end of the arc to 35° or 40° at more southern latitudes, but then swings abruptly northward again in the region sampled by the four most southern earthquakes (events 22 –

25). Second, that in northern and central Tonga (events 1 – 11) slab dip appears to be independent of depth (event 7 being an exception), while south of 22° S the planes tangent to slab structure at intermediate depths (events 15 – 18, 21, 24 and 25) on the whole dip at shallower angles than those obtained for deep-focus data (events 13, 14, 19, 20, 22 and 23). Furthermore, these results are independent of the maximum value of variance reduction, a quantity that ranges from 32% – 91%. By contrast, the best-fitting values of $\partial v_p/\partial T$ are quite uniform and show no particular correlation with event location; the values here, -0.5 ± 0.2 m/s/°K, are very similar to the *Creager and Jordan* [1986] estimate of -0.5 ± 0.1 m/s/°K. What variability does exist is not necessarily a reflection of near-source heterogeneity; it may be due to an imperfect fit of a model to the data, either because the model does not accurately reflect slab structure or due to incomplete removal of non-source heterogeneity from the data in the smoothing operation and corrections.

Towards a unified slab model

With the next generation of models we determine slab structures that satisfy both the intermediate- and deep-focus data in a given segment of the arc. In southern Tonga such a model must bend to a steeper dip somewhere below the intermediate-focus events, but since the residual sphere data are sensitive not only to the slab directly beneath them but to structure averaged over several hundred kilometers, they do not uniquely determine the location of the bend. However, seismicity in southern Tonga defines a relatively uniform plane which extends 50° – 55° down to 550 km, suggesting that the bend occurs at or below this depth. Furthermore, the data for two deep earthquakes in the eastern half of the southern Tonga bifurcated zone (events 14 and 20) are better matched if the dip increase is slightly below them rather than at a shallower depth. For southern Tonga, therefore, we define "bending" models which extend to a depth of 550 km at a dip of 50° – 55°, and whose deeper dip is left as a free parameter. Models with a shallow dip much different from this not only mismatch the observed trend of the seismicity, but, more importantly, provide poor fits to the majority of intermediate-focus events. In central and northern Tonga we define a "bending" model whose dip is set at 50° above 250 but is allowed to vary as a single free parameter below this depth. The residual sphere data for earthquakes in central and northern Tonga (with the exception of event 7) do not require any variation in slab dip since their tangent arc approximations all dip at 64°, but a bend at 250 km does not significantly perturb their theoretical times, and the seismicity between 14°S and 17°S (events 1 and 2) and in central Tonga (events 8 – 11) is not matched without it. The seismicity and travel time data between 17°S and 20°S are not consistently well-modeled by any simple bending slab.

Table 2 summarizes best-fitting values of slab strike and dip obtained for the bending slab parameterization, and a comparison of the synthetic times yielded by these models (Δt_s) with the real data (Δt_d) is shown in Figure 3.6. Compared to the tangent arc approximation, the bending models yield a smoother variation in strike and dip along the arc; that is, events in the same arc segment may in general be explained by the same, or very similar, models. An examination of where the 90% level of acceptibility falls in the strike and dip parameter space indicates that, for the better modeled events, strike is constrained to lie within ± 10°, and dip within ± 5°, of their maximum variance reduction values. Furthermore, this increased consistency in along-arc structure is accomplished without an overall decline in variance reduction, suggesting that a bend to steeper dip at depth is a real feature of the lithosphere in southern Tonga. Only three earthquakes (events 15, 18 and 22) experience a drop in variance reduction which is greater than 5%, and out of the four that are substantially better fit by the bending models (events 7, 14, 20 and 25) three lie in the depth range 340 km – 510 km and hence are particularly sensitive to structure at the depth of the bend (550 km).

TONGA SLAB MORPHOLOGY AND EXTENT

The bending slab parameterization of the Tonga lithosphere respresents our best attempt at matching the residual spheres for all 25 events, in addition to the observed seismicity, with an advectively undeformed model. Here we further develop these results to investigate several aspects of Tonga slab morphology with direct bearing on the dynamics of subducting lithosphere: the maximum depth to which the slab extends, the character of its deformation at depth and the degree to which these structural variations are matched by trends in the seismicity.

Penetration depth

The travel time residual spheres for all of the earthquakes modeled, with the exception of events 1 and 2, are best fit by slabs extending to at least 1000 km, and the data for the deep-focus events rule out models reaching depths of less than 800 km – 900 km. Curves of variance reduction as a function of slab depth are constructed by terminating the anomaly defined by the best-fitting model for a given earthquake at various depths and recomputing synthetic times for each structure. The resulting R values (shown by the symbols in the left-hand plots of Figure 3.7) indicate increasing slab length beyond 1000 km does not significantly improve the fit of a model to the data; that is the travel time observations "saturate" below about 1000 km because the majority of the downgoing rays have turned out of the high velocity anomaly by this depth [*Creager and Jordan,* 1984, 1986]. Apart from events 1 and 2, however, decreasing slab length above 1000 km does produce a decrease in variance reduction.

The deep-focus earthquakes (events 4, 5, 12, 13, 22 and 23, shown by solid lines) are particularly sensitive to the slab termination depth, and for these data the 90% level of acceptibility (whose range in a particular arc segment is indicated by the vertical dashed lines in each plot) indicate a minimum slab depth extent of 725 km – 775 km in northern Tonga south of 17° S, 800 km – 850 km in central Tonga, and 825 km – 875 km in southern Tonga. However, a slab this short in northern Tonga (terminating less than 100 km below the deepest seismicity) requires anomalously high values of $\partial v_p / \partial T$ (–1.3 m/s/°K for event 4 and –1.6 m/s/°K for event 5) more than double the best estimate of –0.5 m/s/°K from other studies [*Sumino,* 1979; *Sumino et al.*, 1983; *Suzuki and Anderson,* 1983; *Suzuki et al.*, 1983; *Hager et al.,* 1985; *Creager and Jord5an,* 1986]. Constraining $\partial v_p/\partial T$ to be −1.0 m/s/°K or less yields R values for events 4 and 5 which rule out models shorter than roughly 850 km. Applying this constraint on $\partial v_p/\partial T$ to models for central and southern Tonga does not significantly alter estimates of minimum slab depth for these arc segments.

In contrast to every other event modeled in this study, events 1 and 2 (dashed lines in the top left-hand plot of Figure 3.7) indicate an intersection of a variance reduction maximum and acceptable $\partial v_p/\partial T$ values with a 525 km slab, and while their 90% confidence levels do not rule out models of 800 km – 900 km, slabs extending deeper than this are not acceptable. The hypocenters for these earthquakes are located at intermediate depth in the far northern end of the Tonga arc, a region devoid of seismicity below a depth of 300 – 400 km. In order to constrain the latitudinal overlap between the slab segment which events 3 – 5 require to extend into the lower mantle and that sampled by events 1 and 2, we compute R as a function of along arc extent. The travel time data for events 3 – 5 are satisfied with a lower mantle slab terminating to the north at roughly 17.5° S, less than 100 km beyond the lateral cut-off in deep-focus activity. While residual spheres for events 1 and 2 prefer a short (525 km) slab extending northward to roughly 14.5°, the most northern latitude at which any subduction zone seismicity occurs, they are equally well fit by a structure of variable length which to their south reaches the lower mantle. A combination of these data therefore suggest that the depth of slab penetration increases from roughly 500 km at the most northern end of the arc to a depth of at least 800 km – 900 km at the onset of deep-focus seismicity. South of 17.5° S, the travel time data are consistent with, but do not require, slabs extending much deeper into the lower mantle. These results are consistent with travel time data from the Mariana and Kuril arcs which necessitate slab penetration to 900 – 1000 km [*Jordan,* 1977; *Creager and Jordan,* 1984, 1986; *Fischer et al.,* 1988]. The slightly deeper minimum slab depth in the northwestern Pacific may be due to a station distribution which samples the residual sphere more densely and evenly.

Lateral deformation

Before determining the relationship of the observed seismicity to the variations in strike and dip indicated by the bending slab parameterization, constraints on the character and dimension of structure in the plane of the slab profile are required. We calculate best-fitting parameter and variance reduction values for two classes of slab structure which are based on the bending model but include advective deformation of the deep lithosphere. "Broken" slab models contain lithospheric fragments laterally offset in the plane of the slab. This paramterization was devised to structurally mimic the imbricated bands of seismicity in southern Tonga. The example shown in Figure 3.8b shows one portion of the slab reaching from the trench down to 750 km depth and a second slab fragment, to the left, extending from 450 km into the lower mantle. The peak velocity anomalies of these two segments are spaced 100 km apart, resulting in a combined width (defined as the half-width of the anomaly multiplied by two) of roughly 200 km between 450 km and 750 km depth, with a significant drop in velocity at the center of the total anomaly. The second mode of deformation which produces "thickened" slab models is defined by a flow field which, over a given depth range, progressively increases the horizontal distance between particle paths at the same depth while conserving mass [*Fischer et al.*, 1988]. The specific flow parameters we use here increase the width of the slab from an undeformed value of 100 km at a depth of 550 km to 300 km at 700 km depth (Figure 3.8c).

The residual sphere travel times are in general insensitive to deep advection in the plane of the slab. In particular, slab material must extend into the lower mantle irregardless of whether the slab model is "bending," "broken" or "thickened." *Fischer et al.* [1988] obtained a similar result for data from deep-focus earthquakes in the Kuril-Kamchatka and Mariana arcs, showing that even with thickening factors of five or more, slabs were required to reach depths of at least 900 km – 1000 km. Variance reduction values for the best-fitting broken and thickened models (summarized for six deep-focus earthquakes in Table 3) indicate that judged by the 90% level of acceptibility these structures are equivalent to the bending model in their ability to explain the observed travel times, except for event 12 whose data are significantly better fit by the thickened slab parameterization. The residual misfit for the bending, broken and thickened models are shown for the six events in Figure 3.9; Δt_d is the real data for the given earthquake (top panel) and the misfit is defined as $\Delta t_d - \Delta t_s$ where Δt_s corresponds to either the bending, broken or thickened parameterization (second, third and bottom panels, respectively). Clearly the thickened model provides a superior fit to the data for event 12 (the amplitude in $\Delta t_d - \Delta t_s$ about zero is minimized; Figure 3.9c).

While the dependence of misfit on deep lateral structure is much smaller for events 4, 9, 13, 22 and 23, some variation does exist at less than the 90% confidence level. The data for four out of these five events are slightly worse fit by a broken versus a bending or a thickened slab (Table 3; event 4, Figure 3.9a and event 12, Figure 3.9c are good examples), and where a difference in R exists between the bending and thickened models (events 9, 22 and 23) the thickened model is always preferred. The latter result, identical to the statistically more significant finding from event 12, contrasts with travel time data from the Kuril-Kamchatka and Mariana arcs which, while consistent with thickening factors of three or more, are best fit by an undeformed bending model [*Fischer et al.*, 1988]. Estimates of slab strike and dip are also generally independent of the specified variations in deep lateral structure. An exception is the 74° dip required for the broken model by event 3 and event 9 data, versus the 64° estimate obtained for the bending and thickened structures. This result, plus lower R and higher $\partial v_p/\partial T$ values, argues against a broken slab model (of the form shown in Figure 3.8b) for northern and central Tonga.

Undulations in strike and dip: structure versus seismicity

At this point we have established that slab length, strike and dip are first-order model parameters which, to a large extent, are independent of secondary characteristics such as the mode of deformation in the transition zone. While an undeformed slab or a structure which smoothly thickens within the transition zone are perhaps prefered by the travel time data, the slab must extend into the lower mantle, and the parameters obtained for the bending model in Table 2 appear to be generally valid for advectively deformed structures as well.

The variation in local values of slab strike and dip is demonstrated by a comparison of the synthetic residual spheres for the bending model parameterization (Figure 3.10), each of which may be viewed as though it were a lens looking down through the slab at the hypocentral location of the event. In order to emphasize the actual strike and dip values for a given earthquake the residuals are $\mathbf{t_s} - \mathbf{c_R}$ minus a mean value; that is, the synthetic data are neither relocated nor smoothed and they are displayed on the residual sphere as a continuous function in azimuth and take-off angle. As in residual sphere plots of discrete data, the regions reporting negative times are blue and those reporting positive times are red.

One of the most striking features of Tonga subduction zone structure is the transition from a slab of constant dip north of 22°S (events 1 – 10, except event 7) to one where the dip steepens by 15° – 25° in the deep focus earthquake zone; the bend is clearly resolved given the ± 5° error bar on dip estimates, and, with the exception of events 6 and 7, the dip of the slab matches that of the downgoing seismicity. In Figure 3.10 the positions of the great circles corresponding to the best-fitting values of local strike and dip for the bending models (indicated by the white line in each residual sphere) provides the most accurate comparison of the various dip values. For several of the earthquakes the negative slab anomaly is offset in dip due to a hypocentral location outside of the cold thermal core of the slab, an effect particularly pronounced for events 12, 20 and 23 which lie in the eastern half of the southern Tonga double seismic zone. Moving an event location to the east of the slab core decreases the apparent dip of the anomaly on the residual sphere; an offset to the west increases it. The correspondence of the observed seismicity to the slab profile is shown in Figure 3.11; each frame corresponds to the profiles indicated in Figure 3.2. The profiles are defined so that the structural parameters inferred for each earthquake they contain are identical to within the resolution of the data (the particular strike and dip values for the models shown are chosen from the middle of the actual parameter distribution).

Another large-scale undulation in Tonga lithospheric structure is the smooth increase in slab strike from a value of 10° at its northern end to a maximum of 35° – 40°, followed by an abrupt swing back to the north shortly after 25° S. The seismicity (viewed from above in Figure 3.2 and in profile in Figure 3.11) also follows this curve, except for the group of deep-focus earthquakes which bend sharply to the west, north of 17° S. Arc segment B – B' is the one region of the arc where no model providing a good match to the observed travel times also fits the seismicity. The data for deep-focus events 3 – 5 require a slab strike slightly east of north no matter whether a model is straight, bending, broken or thickened. Furthermore, we attempt to model the data with tighter radii of curvature and with structures containing a discontinuity in slab strike; neither approach yields a strike value consistent with the data which is significantly to the west of north. Simply put, the northern Tonga travel times are not fit by a continuous slab model which also matches the strike and dip of the observed seismicity, but a variety of other models may fit the data. The orientation of profile B – B' in Figure 3.11 is based on the slab strike inferred from the residual sphere data which coincides with that of the intermediate-focus seismicity, and the diffuse appearance of the events below 550 km is entirely due to their more westward orientation. Viewed from an azimuth of N 35° W they define a coherent vertical band with a secondary discrete grouping offset to its west. Introducing the data for events 6 and 7 indicates that at intermediate depths this segment also strikes east of north, a result which is consistent with the seismicity above 500 km and which reinforces the residual sphere estimate of deep slab azimuth. However, since the pronounced "bench" in slab dip (Profile B – B', Figure 3.11) is not consistent with a simple bending model, the strike and dip values for events 6 and 7 (Table 2) should not be taken to define a specific slab morphology, but rather as an indication of the general orientation of a more complex structure.

A final feature of the Tonga lithosphere which is matched by the seismicity is its apparent decrease in depth extent at the northern termination of the arc. In profile A – A' (Figure 3.11) the best-fitting slab model terminates at 525 km depth and the deepest earthquake hypocenters occur at roughly 300 km. In contrast, the best-fitting structures south of 17° S extend into the lower mantle and contain intense seismicity below 500 km depth. All slab cross-sections indicate a sharp decrease in the number of events between 300 km and 500 km depth. A possible explanation for the drop in seismic activity at these depths is a shift in the balance of slab buoyancy forces due to the phase change at 400 km, and the numerous events below 500 km depth may in turn be due to the 650-km phase change, or to the slab encountering resistance at the top of the lower mantle. If this hypothesis is true, the lack of seismicity below 500 km in northernmost Tonga supports the residual sphere result that the slab in profile A – A' never reaches the upper mantle-lower mantle boundary.

THE DYNAMICS OF SUBDUCTING LITHOSPHERE

Residual sphere analysis of the travel time data from 25 earthquakes reveals that the three-dimensional morphology of the descending lithosphere in Tonga has a number of features in common with slabs elsewhere, but also others which appear to be products of its particular tectonic setting. The penetration of the Tonga slab into the lower mantle (independent of variations in other model parameters), the range of advectively deformed structures which are consistent with the data, and the downward bend in slab dip observed in southern Tonga are reminiscent of the Kuril-Kamchatka, Mariana and Japan lithospheric models obtained by *Creager and Jordan* [1984,1986] and *Fischer et al.* [1988]. However, the shortening of the slab in northernmost Tonga, the complex relationship of seismicity to structure between 17° S and 20° S, and the abrupt northward swing in strike in southern Tonga appear related to historical peculiarities of the Tonga region.

Northern Tonga: where slabs collide

One of the most noted features in Tonga seismicity is the westward hook in the deep-focus zone at the northern end of the arc. However, while previous authors have taken this feature to indicate a bend in slab structure [*Sykes,* 1966; *Billington and Isacks,* 1975;

Billington, 1980; *Giardini and Woodhouse,* 1984, 1986; *Hamburger and Isacks,* 1987], residual spheres for five earthquakes within the hook indicate that the northern end of the slab in fact strikes east of north. The trend of the deep seismicity (which three-dimensional rotations of its hypocenters reveal to be a roughly vertical band striking at about N 35° W) therefore cuts across the deep structure, indicating that if these earthquakes do occur within the Tonga slab, some advective deformation in the transition zone must occur; an undeformed 100-km thick lithosphere striking E of N is simply too thin to contain this band of seismicity. An appealing explanation for the orientation of this band of events is that it marks the intersection of the downgoing lithosphere and a remnant slab fragment from an ancestral subduction zone configuration [*Isacks and Barazangi,* 1977; *Hamburger and Isacks,* 1987].

Several authors have proposed that prior to 10 my ago subduction occurred continuously along a curved zone from Tonga through the Vityaz trench whose location is marked by the chain of rough topography connecting Samoa and the Solomons (Figure 3.1) [*Karig,* 1970; *Karig and Mammerickx,* 1972; *Gill and Gorton,* 1973; *Coleman and Packham,* 1976; *Hamburger and Isacks,* 1987]. This model suggests that between 10 my and 5 my ago the polarity along the northern margin reversed, causing this boundary to swing counter-clockwise to the location where it now forms the New Hebrides arc; a schematic view of this process is shown in Figure 3.12. The seaward migration of the Tonga trench produced opening in the Lau basin beginning at about 5 my ago. *Hamburger and Isacks* [1987] use this geologic history to reconstruct past plate motions and they determine that the remains of the slab subducted at the now-inactive Vityaz trench (which we term the Vityaz slab) now lies in the mantle to the west of Tonga; *Hamburger and Isacks* [1987] infer that the diffuse band of anomalous deep-focus seismicity extending from the northern tip of the New Hebrides Trench, to Fiji, ending at the deep-focus hook of the Tonga subduction zone, delineate its upper margin at a depth of 550 – 650 km. Their reconstruction also includes a slab fragment which was subducted at a now defunct trench along the Hunter fracture zone sometime after

4 my ago. This fragment, however, has not penetrated into the mantle much beyond 600 km and may not yet have intersected the Tonga slab.

According to the *Hamburger and Isacks* [1987] reconstruction an upper corner of the Vityaz slab hits the Tonga lithosphere with an along-arc strike that roughly matches the most northern Tongan deep-focus events, N 35° W. A cartoon of this interaction is shown in Figure 3.13, profile B – B', with the Tonga slab thickening as it penetrates past the Vityaz fragment *en route* to the lower mantle. The Vityaz lithosphere is of course probably deforming as well, and its orientation is parallel or sub-parallel to the strike of the deepest events. An obvious question is whether the Vityaz slab has a signature in the residual sphere travel times for the deep earthquakes within profile B – B'. An examination of Figures 3.6 and 3.9a reveals that event 4 does contained a pronounced negative anomaly not modeled by the bending, broken or thickened Tonga slab models at roughly the azimuths (270° – 300°) and take-off angles (< 50 °) which would sample the Vityaz structure. Event 3 does not indicate such an anomaly, however, and while the event 5 travel times may, it is substantially weaker than in event 4. One explanation is that seismic energy from events in the westward trending hook simply do not travel through the Vityaz structure long enough to reflect it in their travel times. If the earthquakes are located within the Vityaz slab, the simplest way of explaining the azimuth of this band, perhaps the dip of the fragment is too shallow to appear in the residual sphere projections; the first lithosphere the downgoing rays would sample would be the Tonga slab. Such a phenomenon is observed in the Japan arc [*Creager and Jordan,* 1986]. A less straightforward possibility is that the westward trending hook actually occurs completely inside the Tonga slab; in this case, in order to prevent energy from earthquakes inside the Tonga slab from effectively sampling the Vityaz lithosphere the effects of three-dimensional ray-bending (explained more fully in chapter 2) would have to compensate for the tendency of the high velocity lithosphere to act as an anti-waveguide. Finally, a third possibility is that the apparent northward strike of northern Tonga slab is not due to its lithospheric structure at all, but perhaps reflects another type of high velocity anomaly in the lower mantle adjacent to the Tonga arc.

In addition to the deep-focus hook and the band of anomalous hypocenters subparallel to it, the Tonga-Vityaz collision also may explain the bench between 300 and 450 km depth. *Isacks and Barazangi* [1977], *Billington* [1980], and *Hamburger and Isacks* [1987] attribute this feature to onset of opening in the Lau Basin roughly 5 my ago, but it also may represent the slab buckling in response to the additional compressional stress provided by its collision with the Vityaz fragment. Other evidence that the Tonga slab encounters increased resistance to penetration is that deep seismic moment release peaks in this arc segment [*Wyss et al.,* 1984].

Northern Tonga: evidence for lateral shearing

The shallowing of the maximum depth of seismicity towards the northern termination of the Tonga arc, documented by *Louat and Dupont* [1972] and *Giardini and Woodhouse* [1986], led the latter authors to propose a shearing of older, deeper slab material southward relative to the shallow structure. They offer as additional evidence the centroid moment tensor solutions for numerous deep-focus events (data we will examine further in Chapter 4) and the deep aseismic gap at 23° S, which, given their interpretation of this feature as a "scar" marking the subduction of the Louisville ridge, should lie some 500 km further north.

The apparent shallowing of maximum slab depth revealed by travel time data from earthquakes in northern Tonga demonstrates that, in this case, seismicity to a large degree reflects structure; lithospheric penetration into the lower mantle is only required to a latitude of 17.5° S, while a much shorter slab (no deeper than about 500 km – 600 km) continues to roughly 14.5 ° S. This lateral cut-off of the shallow slab agrees with that determined by *Barazangi et al.* [1972] in a study of travel times from Tonga earthquakes to stations located just seaward of the trench, and not only matches the northern termination of the shallow seismicity, but also a shift in tectonic environment. Present-day motion along the trace of the ancestral Vityaz trench is accomodated by shallow strike-slip activity, and the transition between the seafloor morphology and near-surface tectonics indicative of a trench environment and those of a transform fault regime occurs at roughly 14.5 ° S [*Wright,* 1986].

Giardini and Woodhouse [1986] propose that the southward shear is a result of differential motion between the subducted lithosphere and the surrounding mantle; they point out that, according to *Minster and Jordan* [1978], the Pacific plate, the Australian plate and therefore the trench and shallow slab are moving northward with respect to a hotspot reference frame at 5 cm/y, and that if a strain at this rate were imposed on the northern edge of the Tonga lithosphere as it subducted, by the time it reached a depth of 600 km 10 my later, it would be displaced roughly 500 km south of the point where it entered the trench. This model assumes that surface plate motions reflect shallow mantle flow, but that the deeper regions of the lithosphere is fixed with respect to the mantle. Another geometry perhaps capable of producing differential motion between the descending lithosphere and surrounding mantle is one where the plate motion vector between the subducting and overiding plate is oblique to the trench, but this situation is not observed in Tonga [*Minster and Jordan,* 1978]. Finally, preliminary modeling of the balance of buoyancy forces internal to slabs subducting in a three-dimensional flow model suggests that the morphology of the northern slab boundary may in fact be due not to some peculiarity of global flow in the Tonga region, but rather to a higher rate of downward flux in the central regions of the arc [*W. Tao,* pers. comm.]. Therefore, while the structural offset between the shallow and deep slab does appear to be real and is not explained by the tectonic history of the region unless the descending lithosphere is displaced southward after entering the mantle [*Hamburger and Isacks* , 1987], the actual mechanism of the southward shear is still uncertain.

Southern Tonga: a cusp in strike

Over most of its length the Tonga slab describes a typical subduction zone curve, with the exception of the abrupt swing from a strike of 35 ° – 40° to one of 0° – 10° which the residual sphere and seismicity data map at all depths just south of 25° S. This feature was first noted in the seismicity by *Billington* [1980], and *Ansell and Gubbins* [1986] cite it in the slab velcocity anomaly based on analysis of travel time residuals from Tongan events recorded at stations to the south in New Zealand. It coincides with an eastward facing dimple in trench topography which most authors map at 24° S – 25° S (shown by dbdb5 bathymetry data in Figure 3.1) [*Karig,* 1970; *Gill and Gorton,* 1973; *Billington,* 1980; *Kroenke,* 1984; *Kawakatsu,* 1986; *Hamburger and Isacks,* 1987], the latitude of the most recently subducted portion of the Louisville Ridge (due to its oblique angle with the trench the ridge subducts progressively southward). *Vogt* [1973] and *Vogt et al.* [1976] propose that the ridge imparts extra buoyancy to the Pacific plate, causing it to resist seaward migration of the trench. Further evidence of ridge buoyancy is provided by focal mechanisms [*Christensen and Lay,* 1988] and the dramatic drop in seismic energy release at the ridge-trench intersection [*Wyss et al.,* 1984] which may indicate decoupling in the interplate thrust zone.

However, this model must be adapted to include the bend in the subducted lithosphere which the residual sphere data map to lower mantle depths, a feature which lies on a down-dip azimuth from the trench cusp, and not on the trace of the subducted Louisville Ridge. One explanation for this geometry is that the initial resistance to ridge subduction is stronger dynamically than ridge effects or other forces in the deeper lithosphere; that is, the southward sweeping Louisville Ridge produces a time-dependent "ripple" in the entire slab profile directly beneath it. The mechanism by which a non-steady-state feature with such a tight radius of curvature could be transmitted down the lithosphere to depths of 500 km or more without a change in shape is unclear, however. Another view is that cusps are inherent to slab structure and develop without the subduction of anomalous features at a wavelength defined by the dimensions of the entire downgoing plate [*Fukao et al.,* 1987]. In this model the Louisville Ridge may accentuate a bend in the downgoing lithosphere, but is not its sole causative factor.

Southern Tonga: a bend in dip

While the pronounced parallel bands of the deep-focus seismicity in the southern half of the Tonga arc have been taken to suggest particularly strong resistance to slab penetration of the lower mantle [*Giardini and Woodhouse,* 1984], the bend to steeper dip resolved in the deep slab by residual sphere travel times indicate that this arc segment is in fact structurally more similar to northwest Pacific subduction zones than either northern or central Tonga. A number of recent studies indicate that downward curvature of the lithospheric profile may be a global feature of subduction dynamics. *Gurnis and Hager* [1988] propose a viscosity increase of at least a factor of ten between the upper and lower mantle which, due to retrograde trench migration [*Garfunkel et al.,* 1986; *Kincaid and Olson,* 1987] and the continuity of horizontal shear stresses across the 650-km discontinuity, produces a bend in slab dip at this interface. In contrast, *Hsui et al.* [1988] emphasize the balance between density anomalies produced by warping phase boundaries within the slab with gravitational torque due to the entire slab length. Whatever the actual mechanism, however, if downward curvature of the deep slab is a product of typical subduction dynamics, its absence in northern and central Tonga must be explained. In northern Tonga a bend in slab dip may be prevented or obscured by the collision of the Tonga slab with the Vityaz fragment; the case for central Tonga is less clear, although this region may represent a transitional regime between the northern and southern segments.

CONCLUSIONS

Residual sphere data from earthquakes in the Tonga subduction zone require that the descending slab extends to depths of 800 km – 900 km or more. The contorted deep seismic zone and down-dip compressional focal mechanisms suggest that the lithosphere encounters considerable resistance to penetration at the 650-km discontinuity; the travel time data are consistent with, and in the case of one earthquake may prefer, slab models which advectively deform in the transition zone by factors of three or more. In these simple flow parameterizations the details of deformation are averaged out along ray-paths, and any structure with the same basic slab parameters, strike, dip and down-dip extent, will fit the data whether it buckles, fragments, imbricates, etc. The drop in percent velocity anomaly at the center of the broken slab parameterization is an example of a second order feature which is resolved by the observed travel times at less than the 95% confidence level.

Travel time data in the northwest Pacific, are also consistent with substantial advective thickening factors (up to three in Kuril-Kamchatka and five or more in the Marianas), suggesting that advective thickening is possibly a global phenomenon; these residuals, however, are also consistent with slab models that extend into the lower mantle without deforming. Other sources of seismic data may further constrain the degree of deformation in the deep lithosphere. The frequency dependent effects of waveform data have this potential, and scalar and vector descriptions of observed seismic strain rate may require advective thickening factors of 1.5 or more in the central Tonga slab [chapter 4].

Considerable variation in slab structure occurs along the arc, and the match that the observed seismicity provides to the detailed structural undulations is a strong argument that the residual spheres do in fact reflect near-source heterogeneity. The data in southern Tonga require a bend to steeper dip in the deep slab, but the travel times in central and northern Tonga do not. If downward curvature of the slab profile is indeed a global feature of subduction flow, as residual spheres from the northwest Pacific and recent dynamic studies may suggest, the absence of such a feature in northern and central Tonga is perhaps explained by their particular tectonic history.

Much of the complexity in the down-going lithosphere and seismicity, for instance the imbricated deep event distribution in southern Tonga, is explained by resistance to slab penetration at the 650-km discontinuity, and while the precise mechanism for the southward shear of the deep slab is unclear, it is probably related to mantle flow. Certain features, however, are also products of the tectonic history of the arc. The westward hook, the bench in dip and the oblique deep-focus band which appear in northern Tonga may all be explained by the collision of the northward striking Tonga slab with the remnant Vityaz fragment, and the cusp in slab strike and seismicity observed at 25° S is perhaps related to the subduction of the Louisville ridge.

Residual sphere data plus the work of *Grand* [1987] and *Kamiya et al.* [1988] suggest penetration of lithospheric material into the lower mantle beneath the Mariana, Kuril-Kamchatka, Japan, Phillipine and now, Tonga arcs, as well as eastern North America, and while most of these studies do not resolve slab anomalies much below 900 km – 1000 km, *Grand* [1987] and lower mantle models obtained from global tomography suggest that subduction-related downwellings may extend much deeper [*Woodhouse and Dziewonski,* 1987]. While this large flux of lithospheric material into the lower mantle argues against rigorously stratified convection, a discontinuity in the physical properties of the mantle, such as an increase in viscosity [*Vassiliou et al.,* 1984; *Gurnis and Hager,* 1988] is completely plausible if it merely resists the descending slabs without acting as a complete barrier to flow.

TABLE 1. SOURCE PARAMETERS OF EVENTS USED IN THIS STUDY

Event	Date	Time, UT	Latitude, °N	Longitude, °E	Depth, km	m_b	Region
1	June 15, 1984	14:22:25.4	−15.83	−174.8	267	6.0	Tonga
2	Feb. 25, 1984	15:29:13.2	−16.69	−174.77	244	5.5	Tonga
3	July 20, 1980	21:20:03.6	−17.88	−178.60	588	6.0	Tonga
4	Jan. 21, 1977	06:11:05.3	−18.06	−178.37	601	5.7	Tonga
5	Oct. 20, 1981	13:51:45.7	−18.26	−179.30	641	5.5	Tonga
6	Nov. 18, 1984	00:49:11.0	−18.77	−175.44	226	5.4	Tonga
7	Nov. 1, 1984	09:27:39.8	−19.78	−175.79	227	5.6	Tonga
8	June 17, 1980	08:42:57.0	−20.21	−178.44	580	5.5	Tonga
9	July 6, 1977	11:28:31.5	−21.00	−178.58	592	5.6	Tonga
10	April 10, 1982	21:24:41.4	−21.07	−176.25	205	5.5	Tonga
11	Sept. 28, 1984	03:03:46.7	−21.43	−177.79	357	5.7	Tonga
12	April 6, 1971	11:06:28.9	−22.20	−179.51	598	5.6	Tonga
13	May, 29 1975	06:42:11.7	−22.37	179.57	597	5.6	Tonga
14	June 17, 1978	23:12:09.9	−23.03	−179.57	508	5.6	Tonga
15	Aug. 5, 1979	00:53:48.2	−22.86	−177.47	204	6.1	Tonga
16	June 22, 1977	12:08:33.7	−22.91	−175.74	69	6.3	Tonga
17	April 13, 1980	18:04:34.5	−23.53	−177.27	102	6.6	Tonga
18	May 12, 1980	14:23:45.5	−23.63	−177.17	170	5.5	Tonga
19	April 19, 1974	07:05:08.6	−24.08	178.59	594	5.6	Tonga
20	Feb. 3, 1976	12:27:31.4	−25.12	179.72	486	5.7	Tonga
21	Feb. 22, 1975	22:04:33.5	−24.98	−178.88	333	6.1	Tonga
22	Feb. 15, 1971	07:51:02.0	−25.20	178.41	574	5.7	Tonga
23	Mar. 30, 1972	05:34:50.4	−25.69	179.58	479	6.1	Tonga
24	Feb. 7, 1984	05:13:17.8	−25.85	−178.79	339	5.3	Tonga
25	April 19, 1982	07:55:15.8	−26.07	−178.62	344	5.5	Tonga

TABLE 2. BEST-FITTING MODEL PARAMETERS

		Straight Slab Models			Bending Slab Models			
Event	Depth, km	dip, strike	*R*	$\partial v_p/\partial T$	dip1, dip2*, strike	*R*	$\partial v_p/\partial T$	$\partial v_p/\partial T$**
1	267	64°, 15°	66%	−0.7	64°, 15°	66%	−0.7	−0.7
2	244	64°, 15°	78%	−0.6	64°, 15°	78%	−0.6	−0.6
3	588	64°, 15°	36%	−0.5				−0.5
4	601	64°, 15°	68%	−0.6				−0.7
5	641	64°, 15°	66%	−0.5				−0.5
6	227	64°, 20°	69%	−0.3				−0.3
7	226	54°, 30°	48%	−0.4	55°, 74°, 30°	85%	−0.5	−0.4
8	580	64°, 15°	63%	−0.5	64°, 15°	63%	−0.5	−0.6
9	592	64°, 15°	78%	−0.5	64°, 15°	78%	−0.5	−0.5
10	205	64°, 20°	71%	−0.4	64°, 20°	72%	−0.5	−0.4
11	357	64°, 20°	71%	−0.5	64°, 20°	72%	−0.5	−0.5
12	577	64°, 30°	79%	−0.5	55°, 74°, 35°	77%	−0.6	−0.6
13	597	64°, 40°	78%	−0.5	55°, 74°, 35°	78%	−0.5	−0.5
14	508	69°, 20°	52%	−0.3	55°, 69°, 25°	65%	−0.3	−0.3
15	204	55°, 40°	63%	−0.4	55°, 74°, 25°	57%	−0.4	−0.4
16	69	55°, 20°	83%	−0.3	55°, 74°, 35°	87%	−0.3	−0.3
17	102	50°, 30°	83%	−0.5	55°, 74°, 35°	79%	−0.4	−0.4
18	170	69°, 20°	95%	−0.5	55°, 74°, 35°	64%	−0.6	−0.6
19	594	59°, 30°	63%	−0.4	55°, 64°, 30°	63%	−0.5	−0.5
20	486	69°, 35°	32%	−0.3	55°, 74°, 40°	37%	−0.3	−0.3
21	333	59°, 50°	78%	−0.3	55°, 69°, 40°	82%	−0.4	−0.4
22	574	69°, 0°	87%	−0.7	50°, 74°, 10°	82%	−0.6	−0.6
23	479	64°, 350°	56%	−0.4	50°, 69°, 0°	58%	−0.4	−0.4
24	339	55°, 0°	91%	−0.3	50°, 74°, 0°	89%	−0.5	−0.5
25	344	55°, 10°	56%	−0.4	50°, 74°, 5°	69%	−0.5	−0.5

*Applies to "southern Tonga" bending models only (events 7 and 12 – 25).

**$\partial v_p/\partial T$ calculated from bending models (events 1 – 2, 7 – 25) or straight models (events 3 – 6) with 420-km and 650-km phase changes.

TABLE 3. BEST-FITTING PARAMETERS FOR MODELS INCLUDING ADVECTIVE DEFORMATION

	Broken Slab Models			Thickened Slab Models		
Event	dip1, strike	R	$\partial v_p/\partial T$	dip1, dip2*, strike	R	$\partial v_p/\partial T$
4	74°, 10°	60%	−0.8	64°, 5°	68%	−0.6
9	74°, 15°	75%	−0.5	64°, 15°	80%	−0.5
12	69°, 30°	71%	−0.6	55°, 69°, 35°	90%	−0.6
13	69°, 35°	82%	−0.5	55°, 74°, 35°	78%	−0.5
22	74°, 10°	80%	−0.6	50°, 74°, 5°	85%	−0.5
23	69°, 0°	58%	−0.5	50°, 64°, 355°	61%	−0.4

*Applies to thickened models based on "southern Tonga" bending structures only (events 12, 13, 22 and 23).

Figure 3.1. Basemap showing the major tectonic features of the Tonga - New Hebrides arc complex. Contours indicate seafloor topography from the dbdb5 dataset at a 2500 m interval. Bold line with teeth shows location of Tonga-Kermadec Trench along which active subduction is ocurring. Arrow indicates relative plate motion vector between the Pacific and Australian plates.

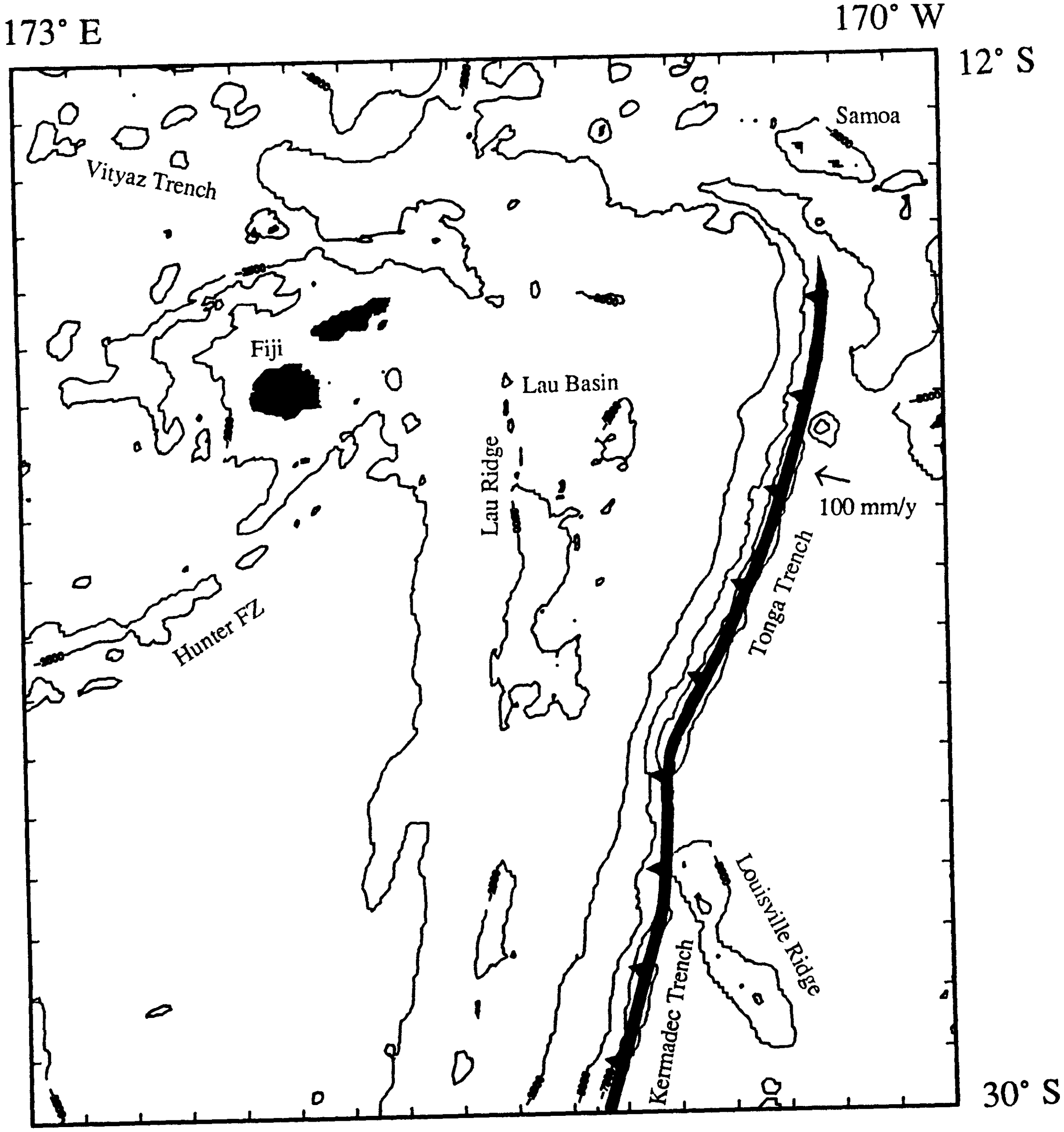
173° E
170° W
12° S
30° S
Samoa
Vityaz Trench
Fiji
Lau Basin
Lau Ridge
100 mm/y
Tonga Trench
Hunter FZ
Louisville Ridge
Kermadec Trench

Figure 3.1

Figure 3.2. Map of Tonga arc seismicity. Events below 300 km and south of 16° S are relocated hypocenters [*Giardini and Woodhouse,* 1984] and other data are from the ISC catalogue for depths greater than 10 km. Minimum event size is $m_b = 5.2$. Squares indicate locations for the 25 earthquakes modeled in this study. Profiles correspond to the structurally distinct arc segments shown in Figure 3.11.

Figure 3.2

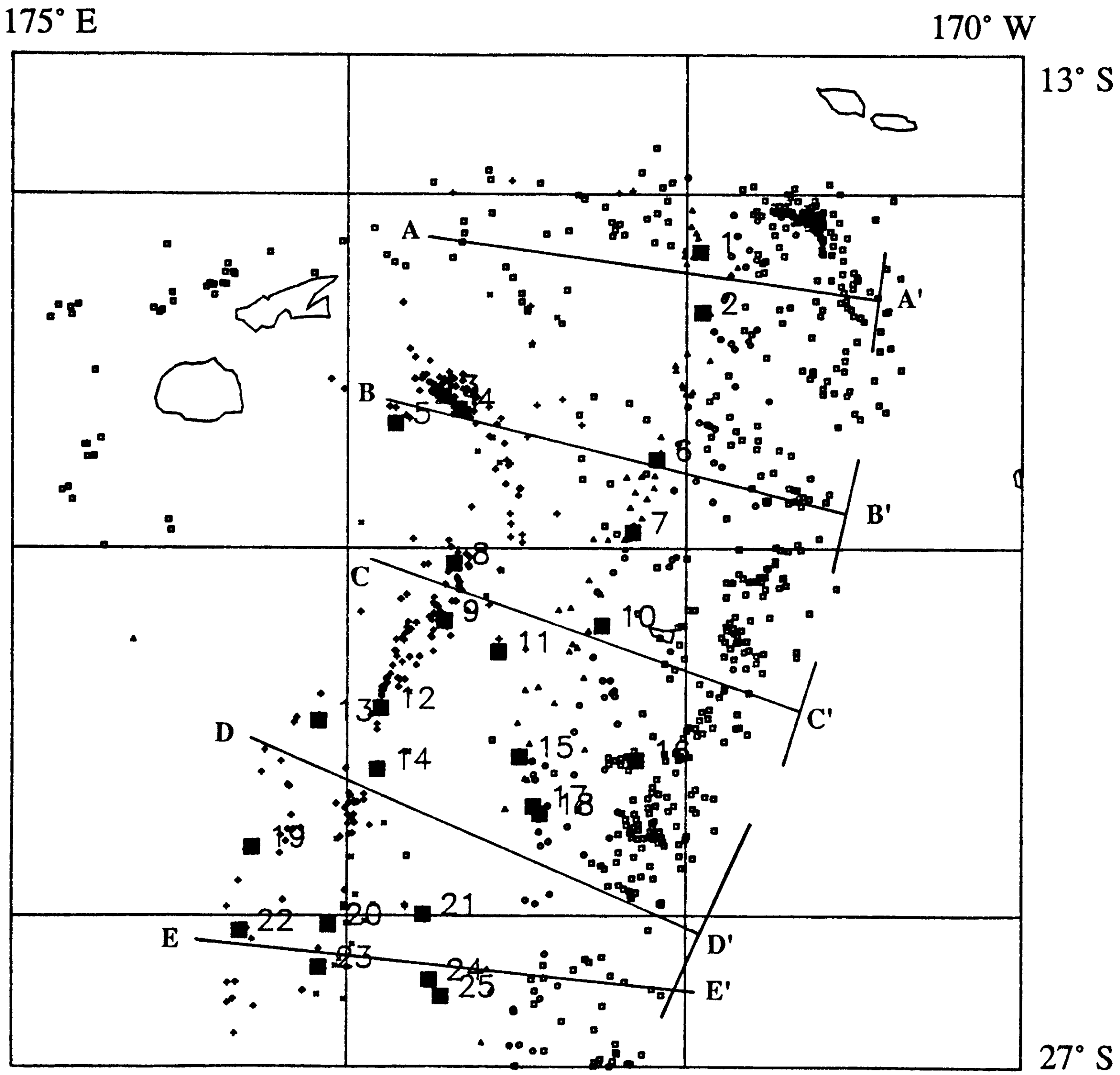
175° E
170° W
13° S
27° S
A
A'
B
B'
C
C'
D
D'
E
E'
1
2
3
4
5
6
7
8
9
10
11
12
13
14
15
16
17
18
19
20
21
22
23
24
25

Figure 3.3. *a* −*f)* Residual sphere projections of the observed travel times for event 17 which the ISC locates at 102 km depth (Table 1). *g* − *i)* Synthetic data which maximizes variance reduction for this event. Residual spheres are equal-area, lower hemisphere projections. Outer perimeter corresponds to the locus of rays with takeoff angles of 60° from vertical; data outside this range are not shown. Circles represent negative residuals; crosses are positive; the size of the symbol is proportional to residual, with 1-s residuals shown in upper box. Bold line running through smoothed and relocated theoretical residual sphere *(i)* represents plane tangent to the slab model from which it was calculated. Same plane shown in *(a)* Operators and corrections applied to the data are explained in the text.

Figure 3.3

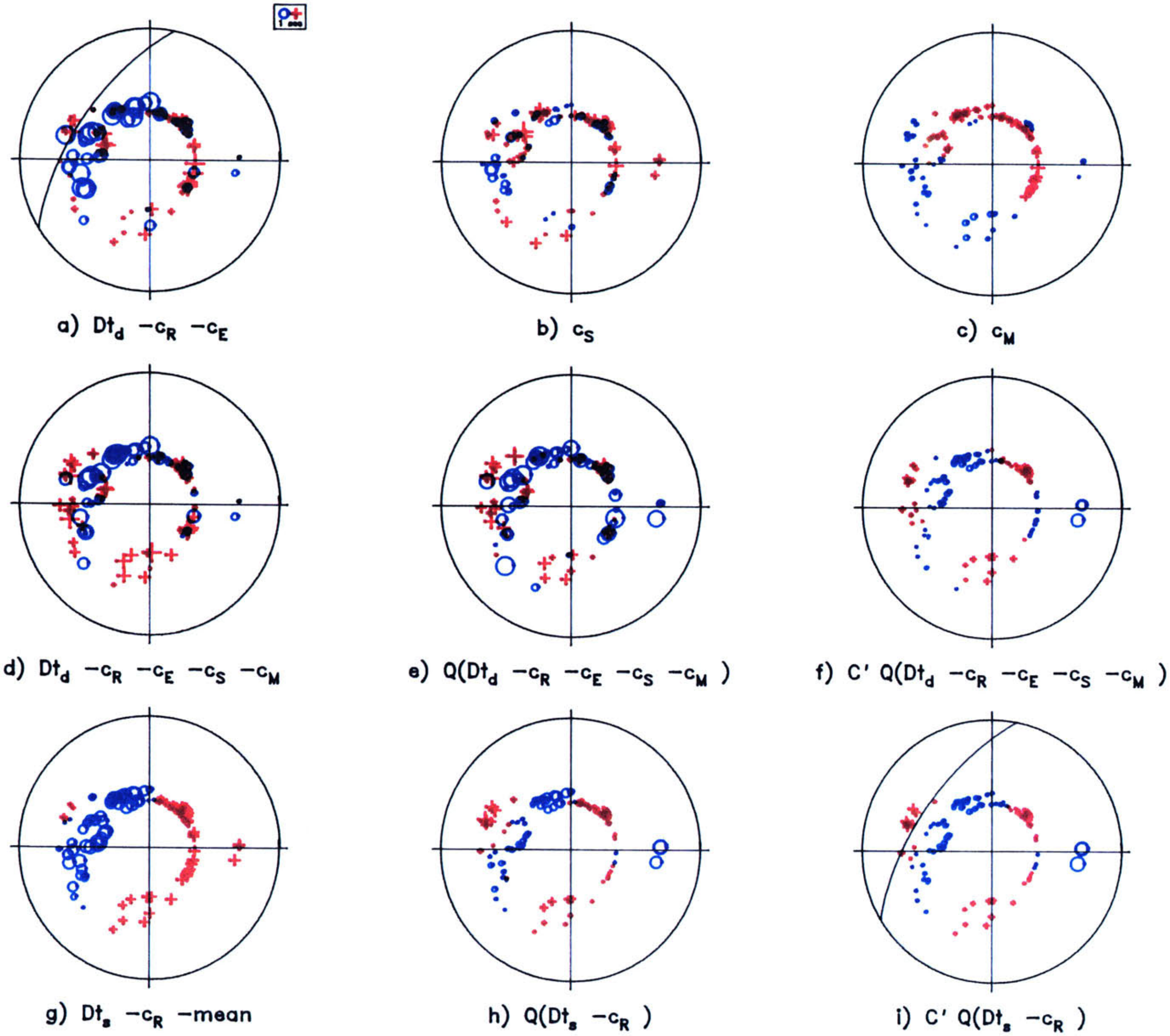

a) $Dt_d \; -c_R \; -c_E$

b) c_S

c) c_M

d) $Dt_d \; -c_R \; -c_E \; -c_S \; -c_M$

e) $Q(Dt_d \; -c_R \; -c_E \; -c_S \; -c_M \;)$

f) $C' \; Q(Dt_d \; -c_R \; -c_E \; -c_S \; -c_M \;)$

g) $Dt_s \; -c_R$ −mean

h) $Q(Dt_s \; -c_R \;)$

i) $C' \; Q(Dt_s \; -c_R \;)$

Figure 3.4. Residual sphere projections of "raw" observed travel times ($\mathbf{Dt_d} - \mathbf{c_R} - \mathbf{c_E}$) for the 25 events modeled in this study. The ISC depth for each earthquake is shown to the upper right of its residual sphere.

Figure 3.4

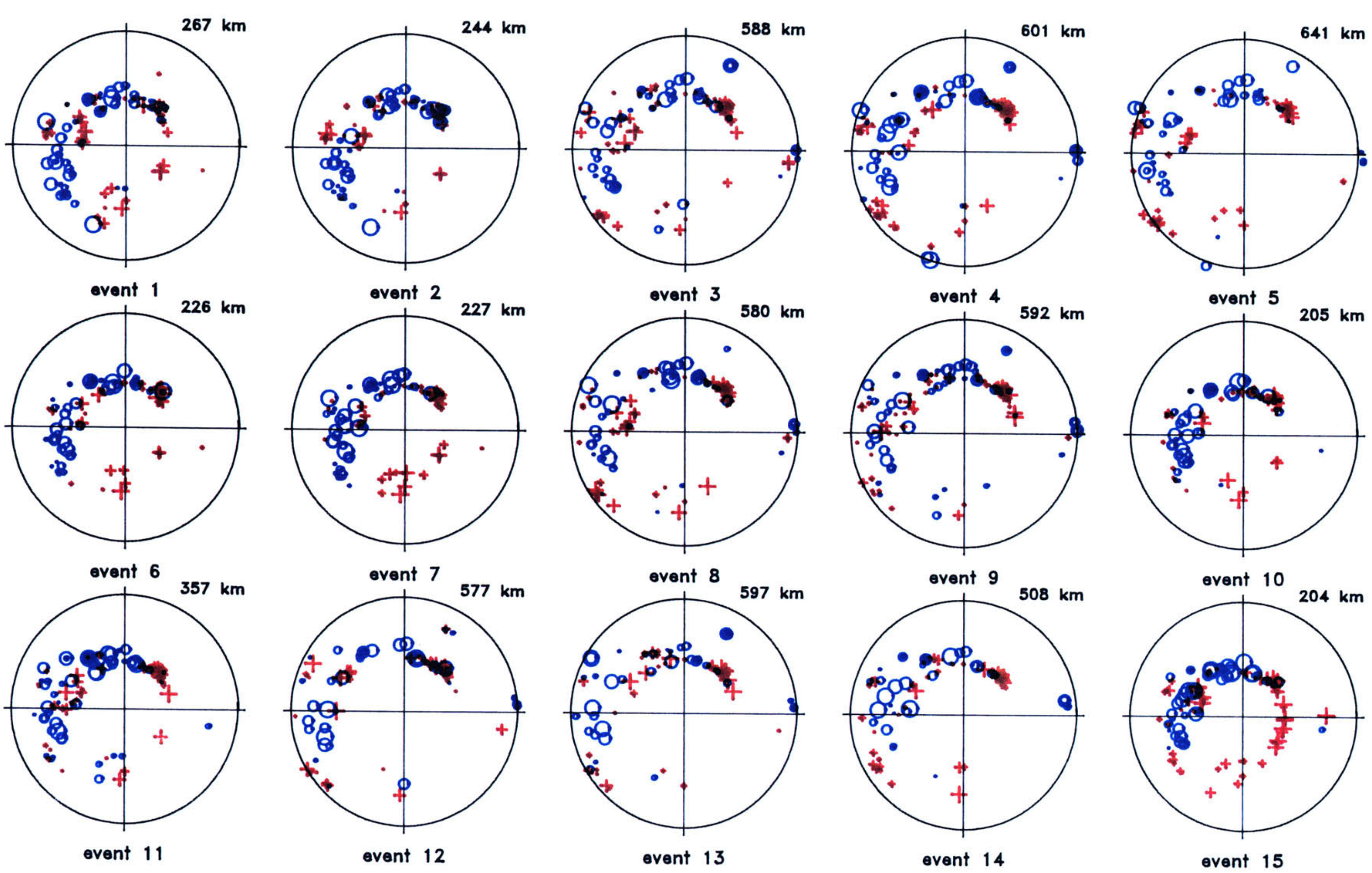

267 km
event 1
244 km
event 2
588 km
event 3
601 km
event 4
641 km
event 5
226 km
event 6
227 km
event 7
580 km
event 8
592 km
event 9
205 km
event 10
357 km
event 11
577 km
event 12
597 km
event 13
508 km
event 14
204 km
event 15

Figure 3.4

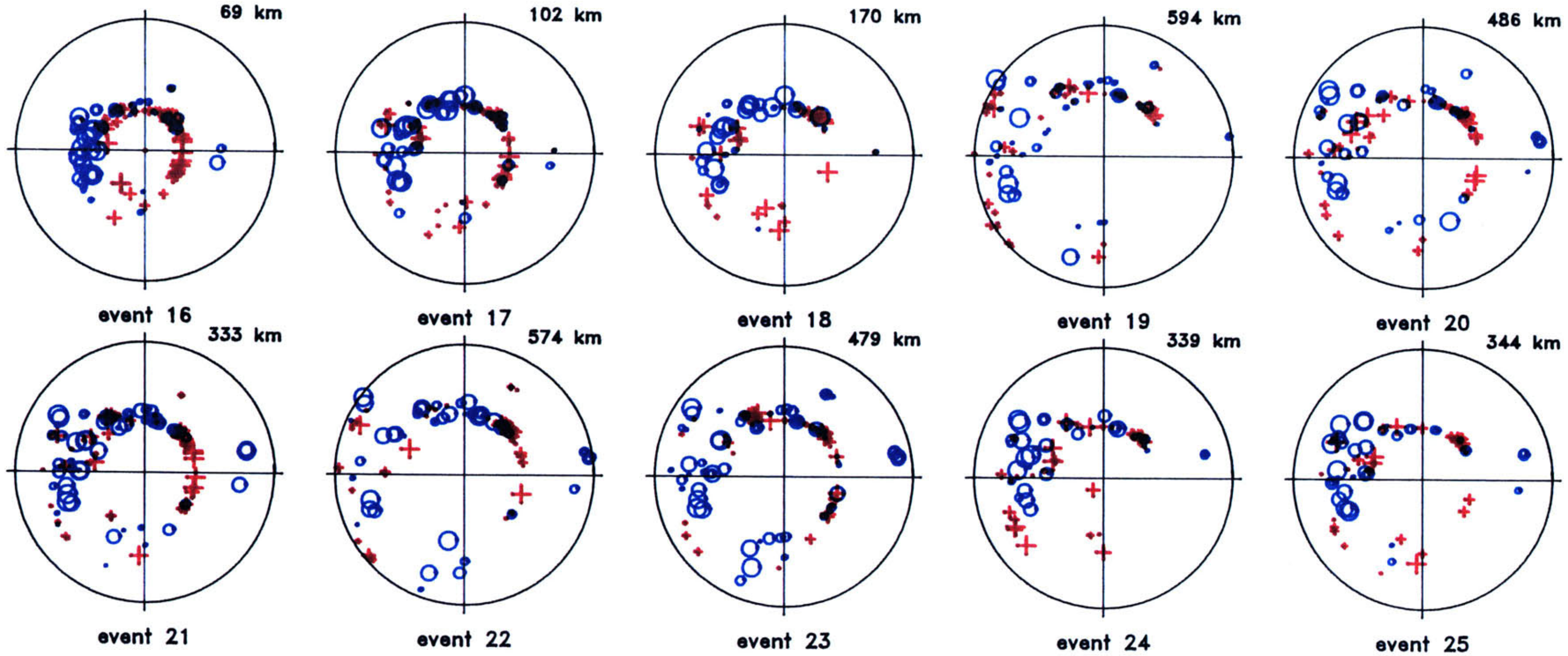
69 km
event 16
102 km
event 17
170 km
event 18
594 km
event 19
486 km
event 20
333 km
event 21
574 km
event 22
479 km
event 23
339 km
event 24
344 km
event 25

Figure 3.5. Residual sphere projections illustrating the effects of various smoothing operators on the data for deep-focus event 9. *Left-hand column)* Observed travel time residuals: *(top)* residual sphere has been relocated but not smoothed; *(middle)* relocated times smoothed with the intermediate filter ($\Delta t_d'$); *(bottom)* relocated and smoothed with the standard operator (its residuals may be denoted Δt_d). The intermediate filter with its larger number of degrees of freedom maintains a steeper down-dip gradient, but still diminishes many of the higher wave number travel time patterns. *Right hand column)* Relocated theoretical residual spheres for the best-fitting central Tonga slab model with no smoothing *(top)*, the intermediate filter *(*$\Delta t_s'$*, middle row)*, and the standard filter *(*Δt_s*, bottom)*. Since the unsmoothed theoretical times define a pattern that is already quite smooth, application of the intermediate and standard filters has relatively little impact.

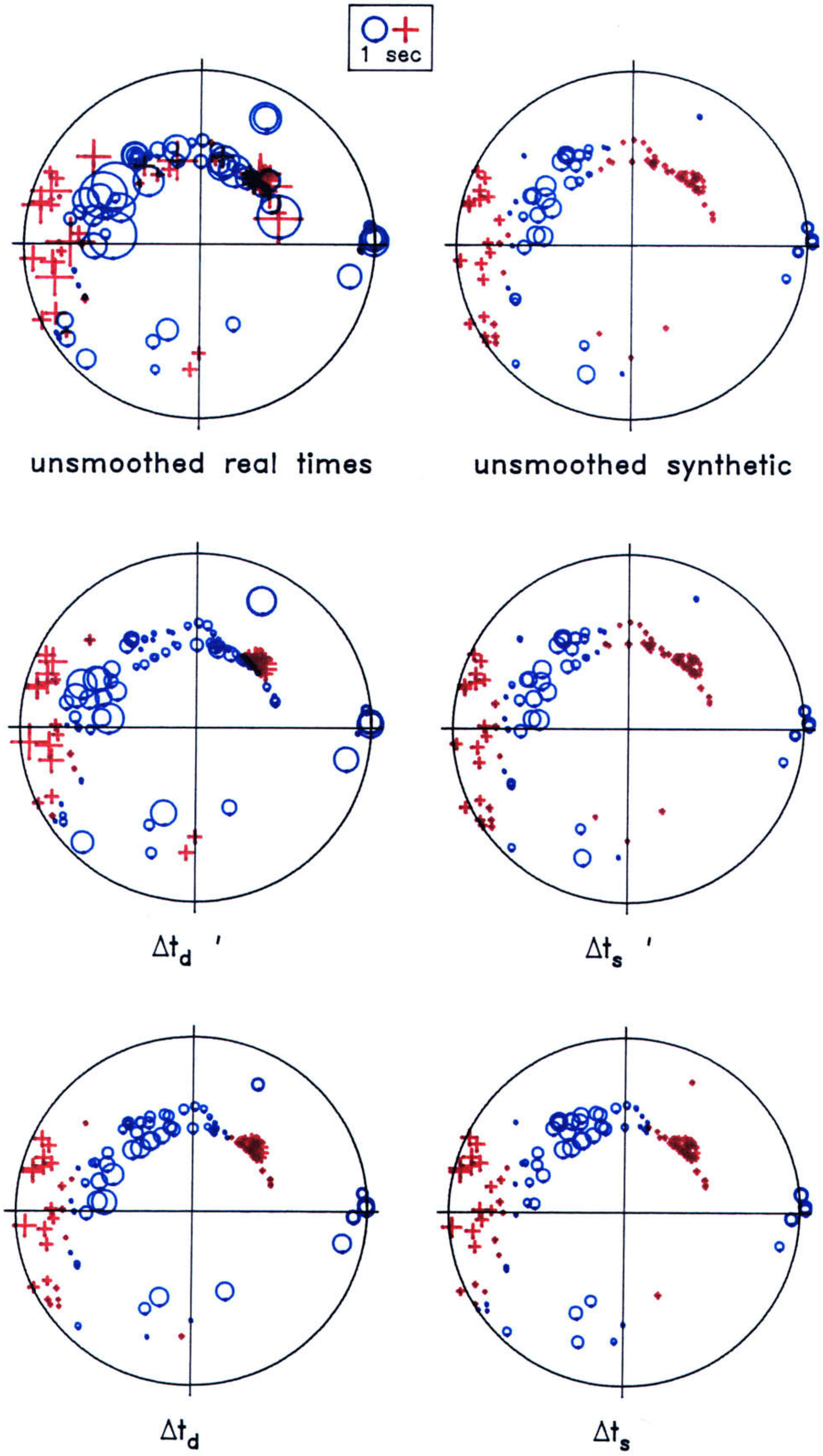

unsmoothed real times

unsmoothed synthetic

Δt_d '

Δt_s '

Δt_d

Δt_s

Figure 3.5

Figure 3.6. Residual sphere projections for all 25 events comparing the real data ($\Delta \mathbf{t_d}$) to the synthetic times ($\Delta \mathbf{t_s}$) from the best-fitting bending slab models (Table 1) The ISC depth for each earthquake is shown to the upper right of its residual sphere. Bold line running through residual spheres represents plane tangent to the slab model from which they were calculated.

Figure 3.6

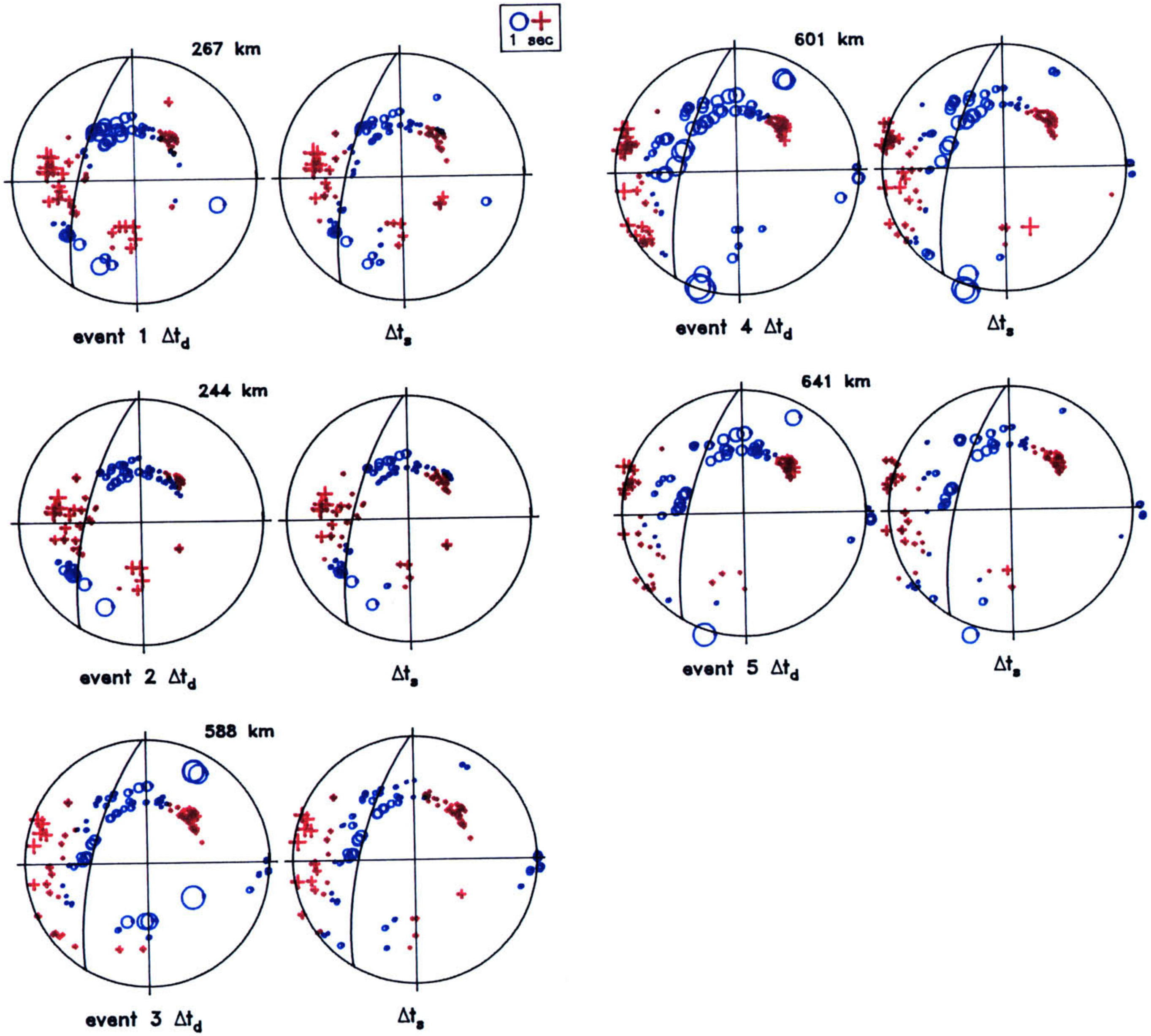
1 sec
267 km
event 1 Δt_d
Δt_s
601 km
event 4 Δt_d
Δt_s
244 km
event 2 Δt_d
Δt_s
641 km
event 5 Δt_d
Δt_s
588 km
event 3 Δt_d
Δt_s

Figure 3.6

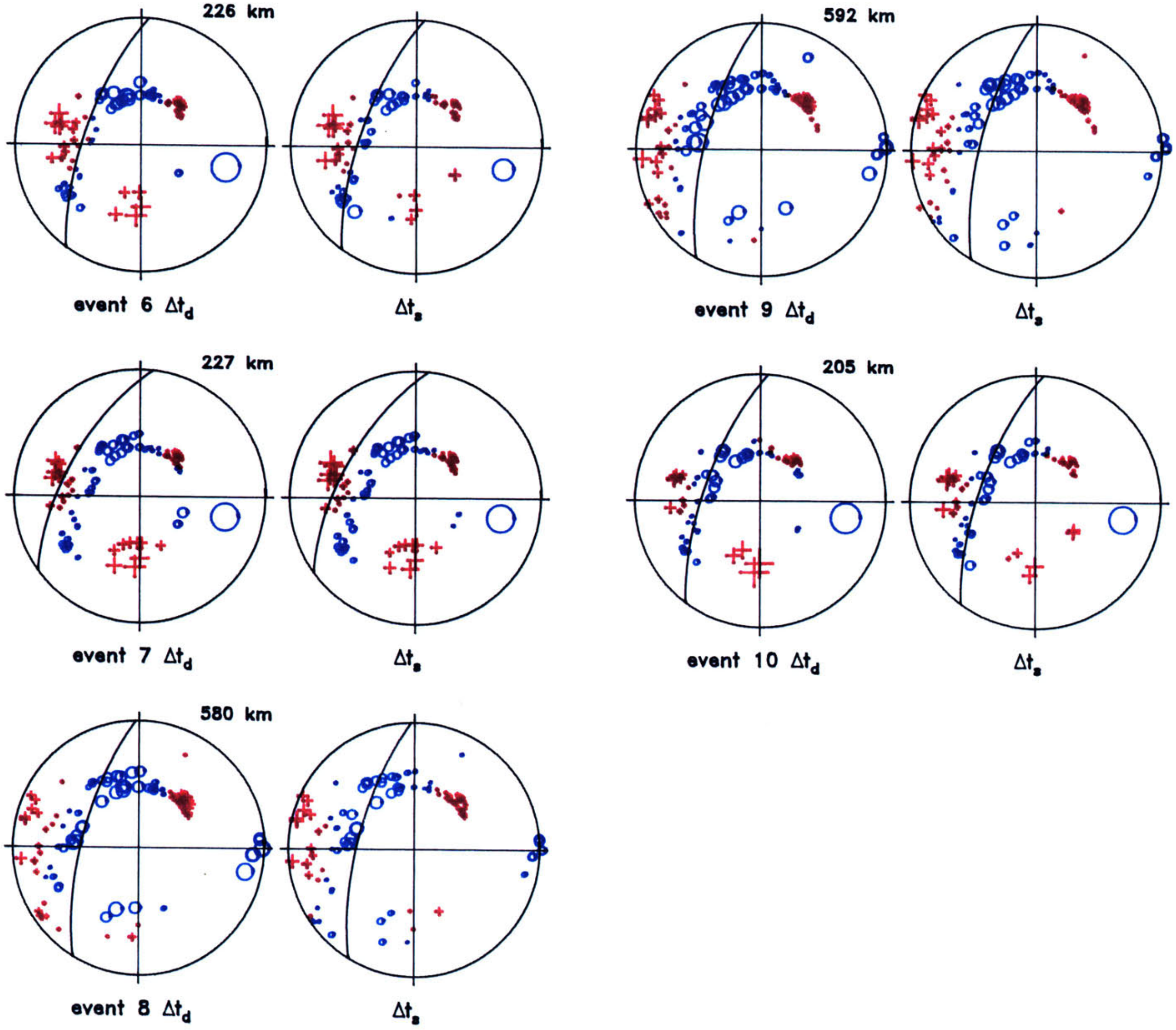
226 km
event 6 Δt_d
Δt_s
592 km
event 9 Δt_d
Δt_s
227 km
event 7 Δt_d
Δt_s
205 km
event 10 Δt_d
Δt_s
580 km
event 8 Δt_d
Δt_s

Figure 3.6

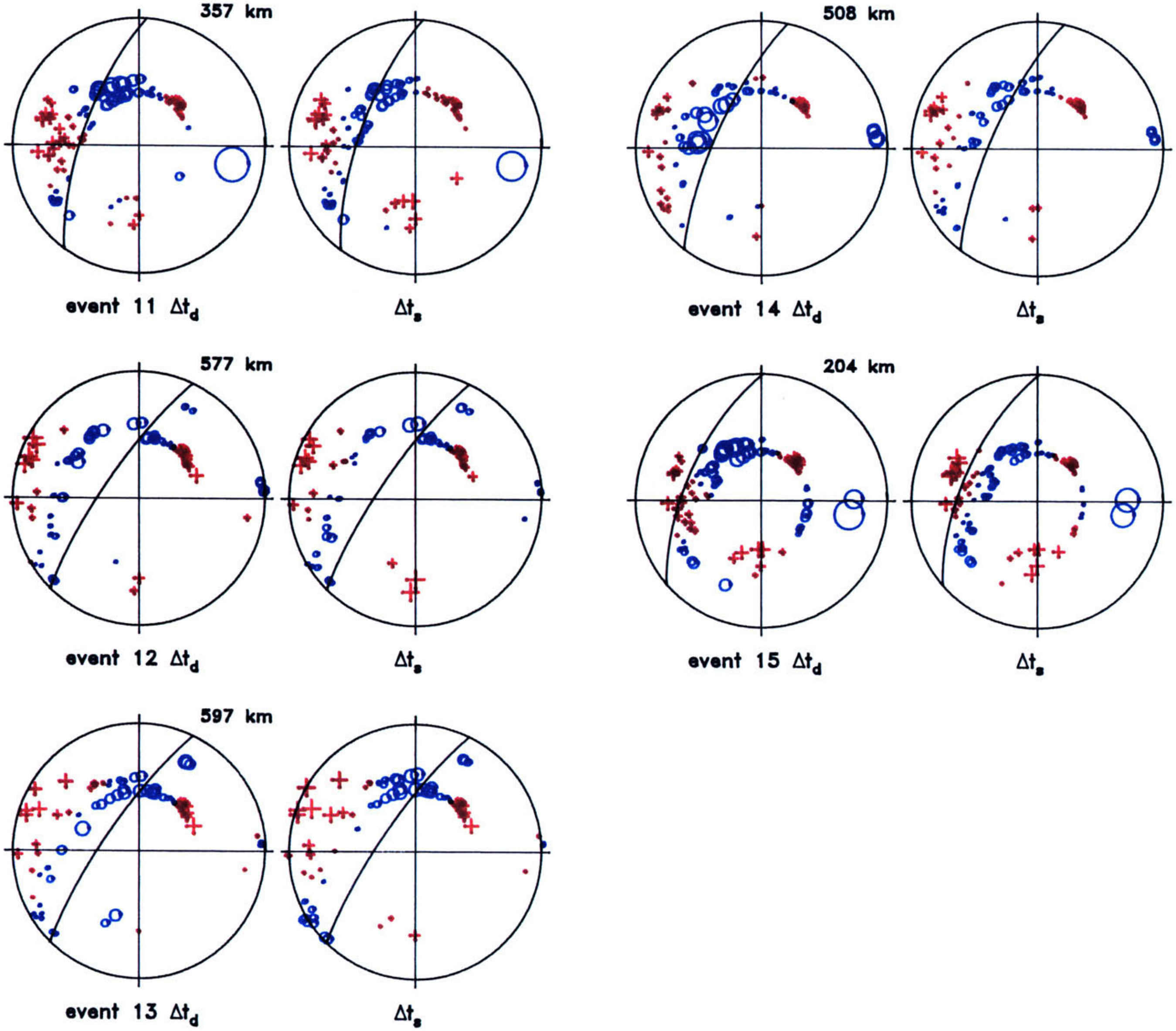
357 km
event 11 Δt_d
Δt_s
508 km
event 14 Δt_d
Δt_s
577 km
event 12 Δt_d
Δt_s
204 km
event 15 Δt_d
Δt_s
597 km
event 13 Δt_d
Δt_s

Figure 3.6

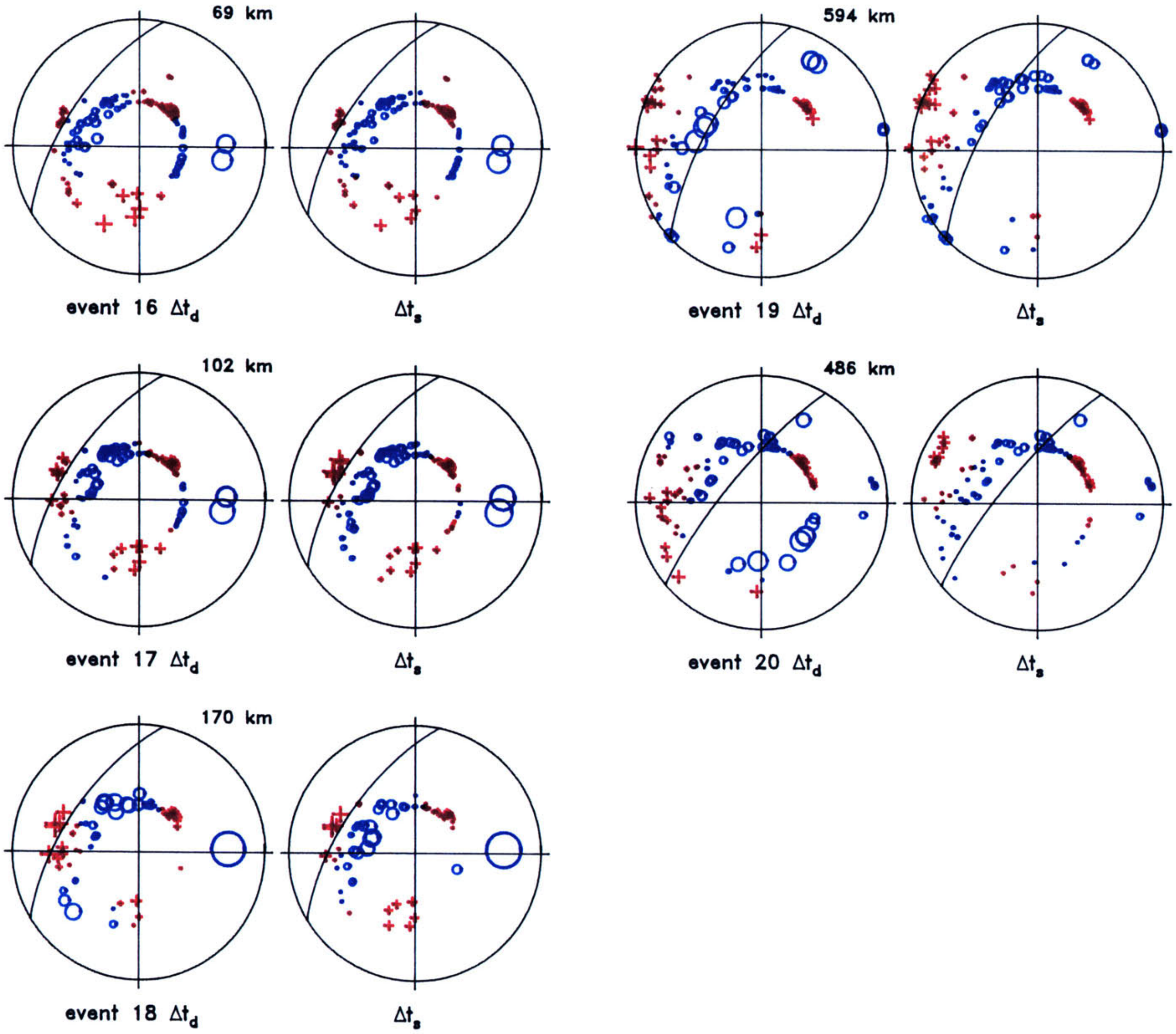
69 km
event 16 Δt_d
Δt_s
594 km
event 19 Δt_d
Δt_s
102 km
event 17 Δt_d
Δt_s
486 km
event 20 Δt_d
Δt_s
170 km
event 18 Δt_d
Δt_s

Figure 3.6

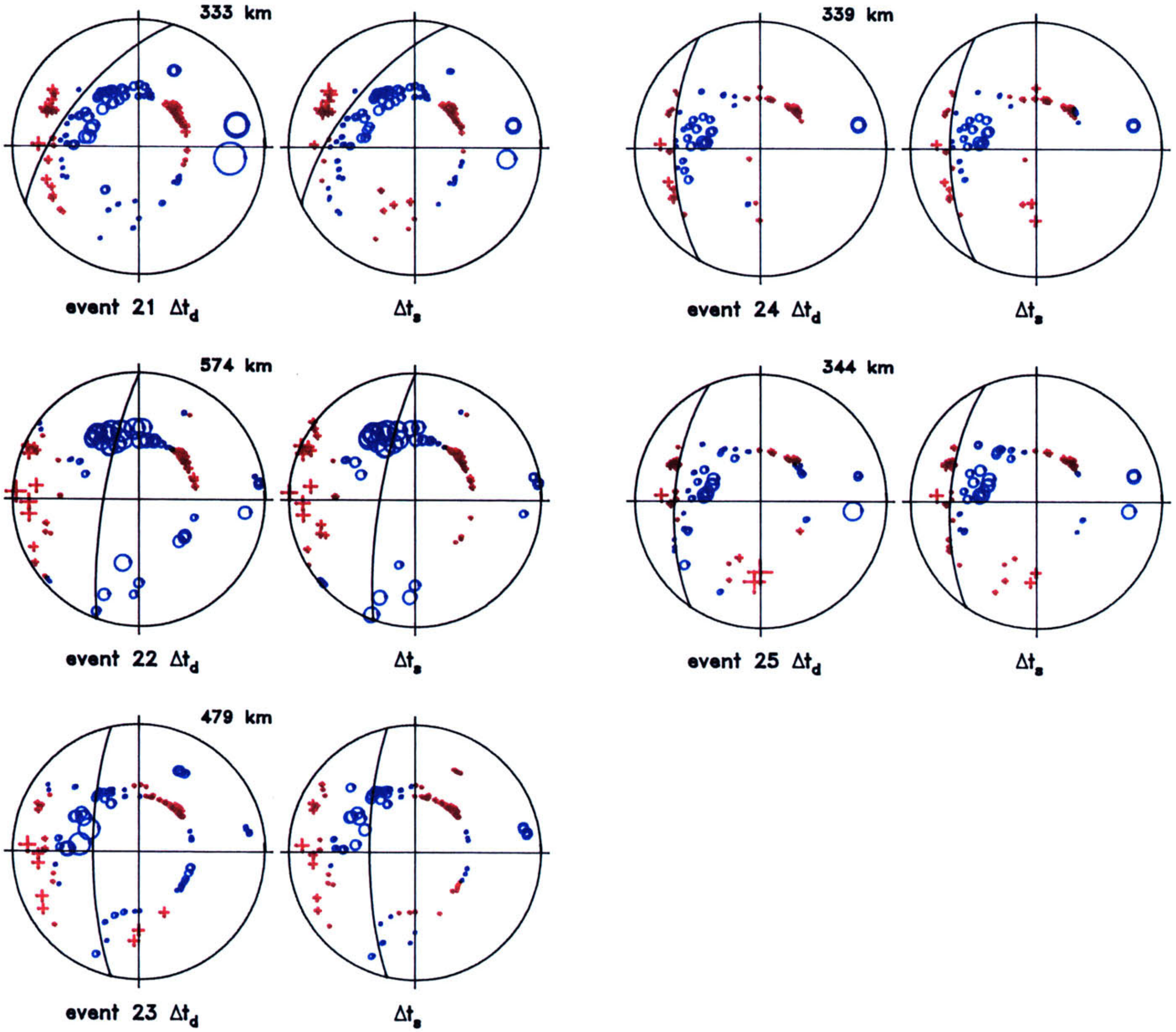
333 km
event 21 Δt_d
Δt_s
339 km
event 24 Δt_d
Δt_s
574 km
event 22 Δt_d
Δt_s
344 km
event 25 Δt_d
Δt_s
479 km
event 23 Δt_d
Δt_s

Figure 3.7. *left)* R values as a function of slab penetration depth for the bending slab parameterization in northern *(top)*, central *(middle)* and southern *(bottom)* Tonga. Each curve corresponds to a different earthquake. *right)* Thermal coefficient of velocity ($\partial v_p / \partial T$) as a function of penetration depth for the same models. Dashed lines indicate the 90% confidence level. Increasing slab length beyond 1000 km does not significantly improve the fit of a model to the data, but apart from events 1 and 2, decreasing slab length above 1000 km does produce a decrease in variance reduction. Slab models (except those for events 1 and 2) must extend to depths of 800 km – 900 km.

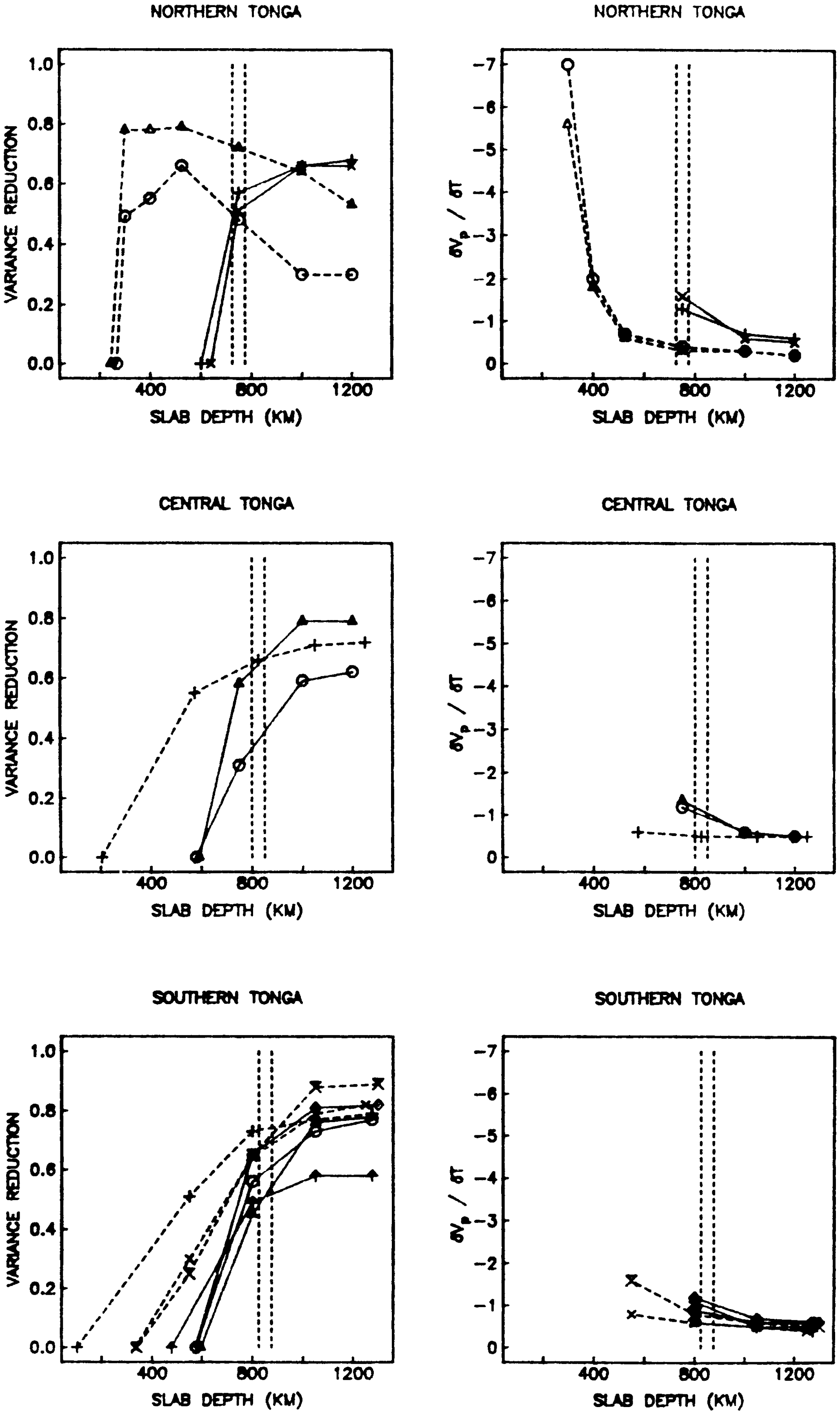
NORTHERN TONGA
NORTHERN TONGA
CENTRAL TONGA
CENTRAL TONGA
SOUTHERN TONGA
SOUTHERN TONGA
VARIANCE REDUCTION
δV_p / δT
0.0
0.2
0.4
0.6
0.8
1.0
0
−1
−2
−3
−4
−5
−6
−7
400
800
1200
SLAB DEPTH (KM)

Figure 3.7

Figure 3.8. Contours of seismic velocity (0.25 km/s) which delineate slab models with varying degrees of advective thickening in the transition zone: *a)* "bending," *b)* "broken," and *c)* "thickened" slabs. Slab dip corresponds to the best-fitting value for southern Tonga event 22 (Profile E – E'). Dots are observed seismicity from the same dataset shown in Figure 3.2.

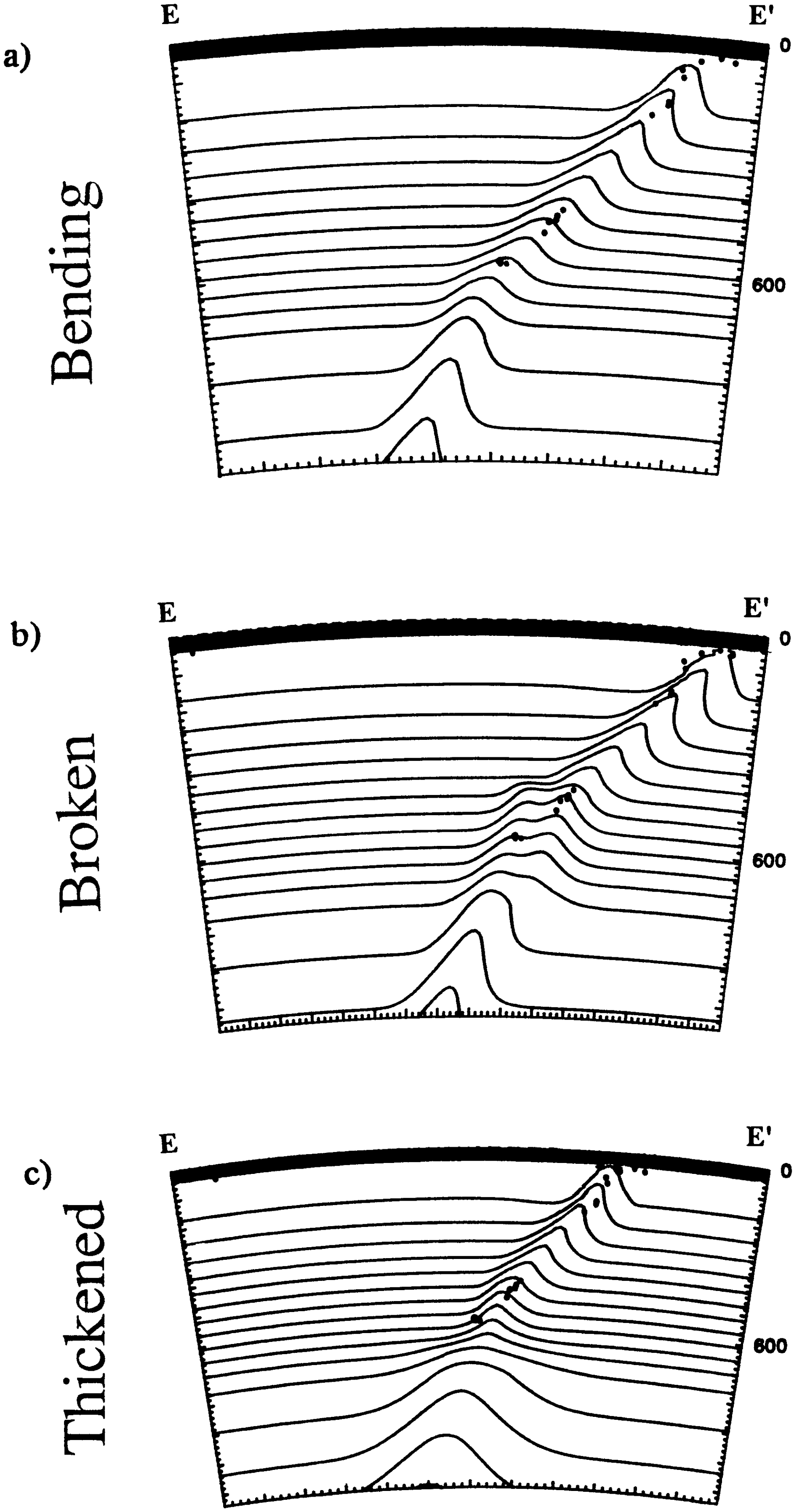

Figure 3.8

Figure 3.9. *a - g)* Plots of corrected, relocated, and smoothed travel time residuals as a function of azimuth on the residual sphere for six deep-focus events. *top panel)* $\Delta \mathbf{t_d}$ for the given earthquake. *second, third and bottom panels)* $\Delta \mathbf{t_d} - \Delta \mathbf{t_s}$ where $\Delta \mathbf{t_s}$ corresponds to either the bending, broken or thickened parameterization, respectively. The better the fit the smaller the amplitude in $\Delta \mathbf{t_d} - \Delta \mathbf{t_s}$ about zero.

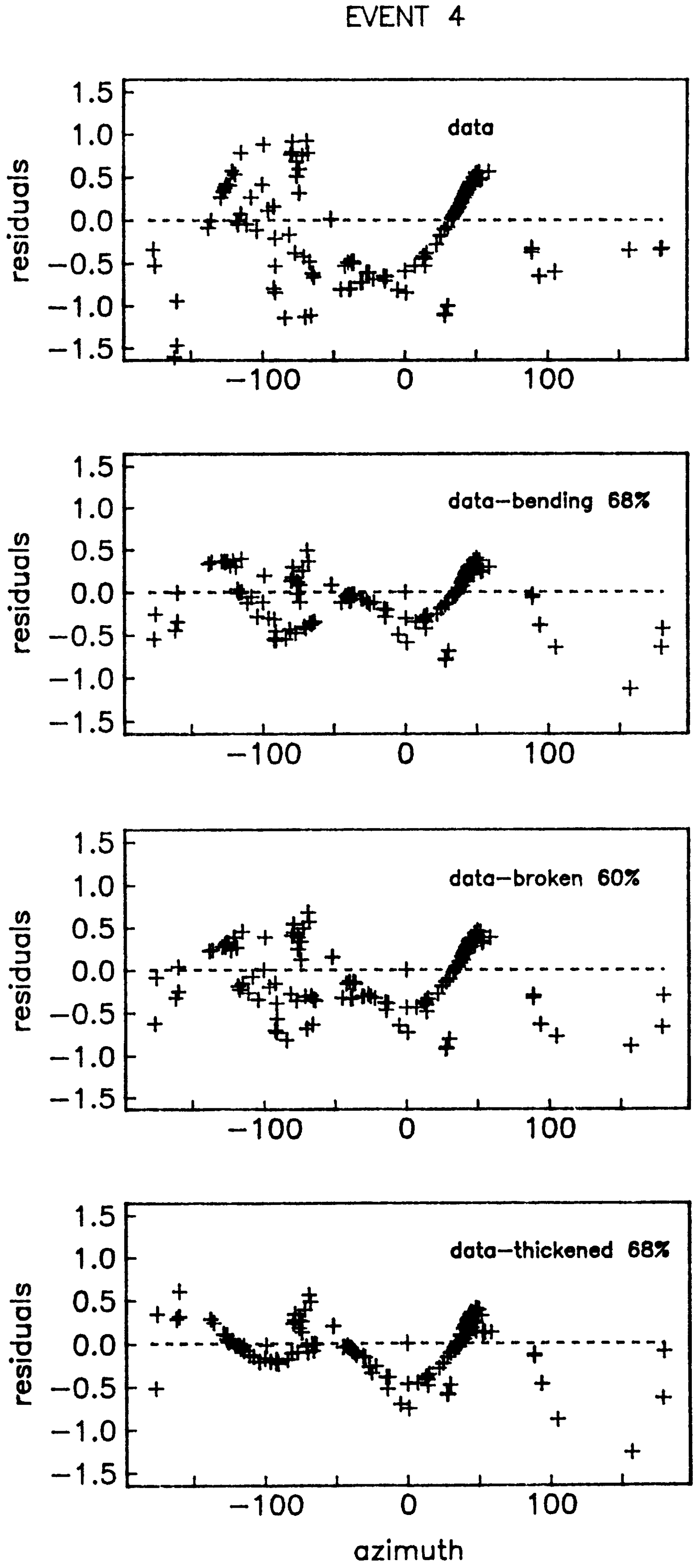
EVENT 4
data
data–bending 68%
data–broken 60%
data–thickened 68%
residuals
1.5
1.0
0.5
0.0
−0.5
−1.0
−1.5
−100
0
100
azimuth

Figure 3.9

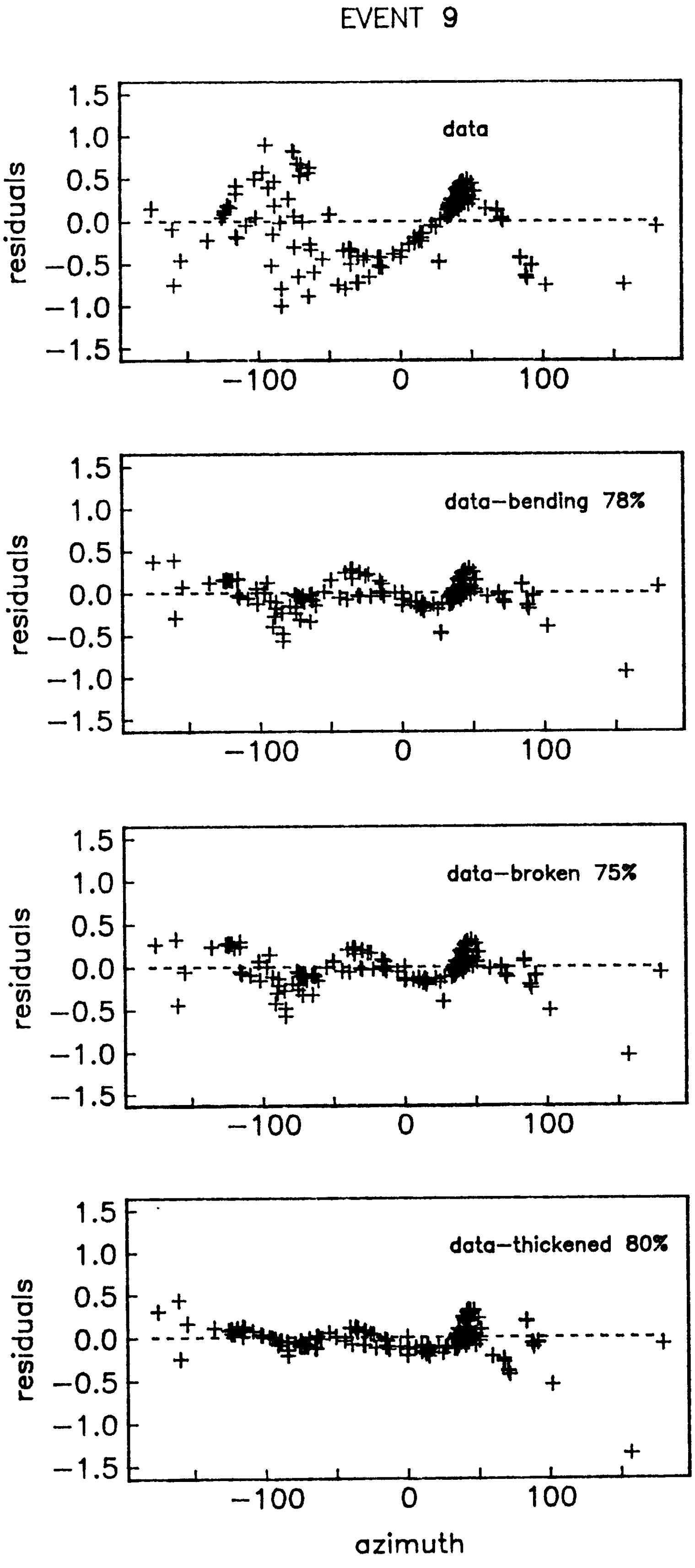
EVENT 9
residuals
1.5
1.0
0.5
0.0
−0.5
−1.0
−1.5
−100
0
100
data
data−bending 78%
data−broken 75%
data−thickened 80%
azimuth

Figure 3.9

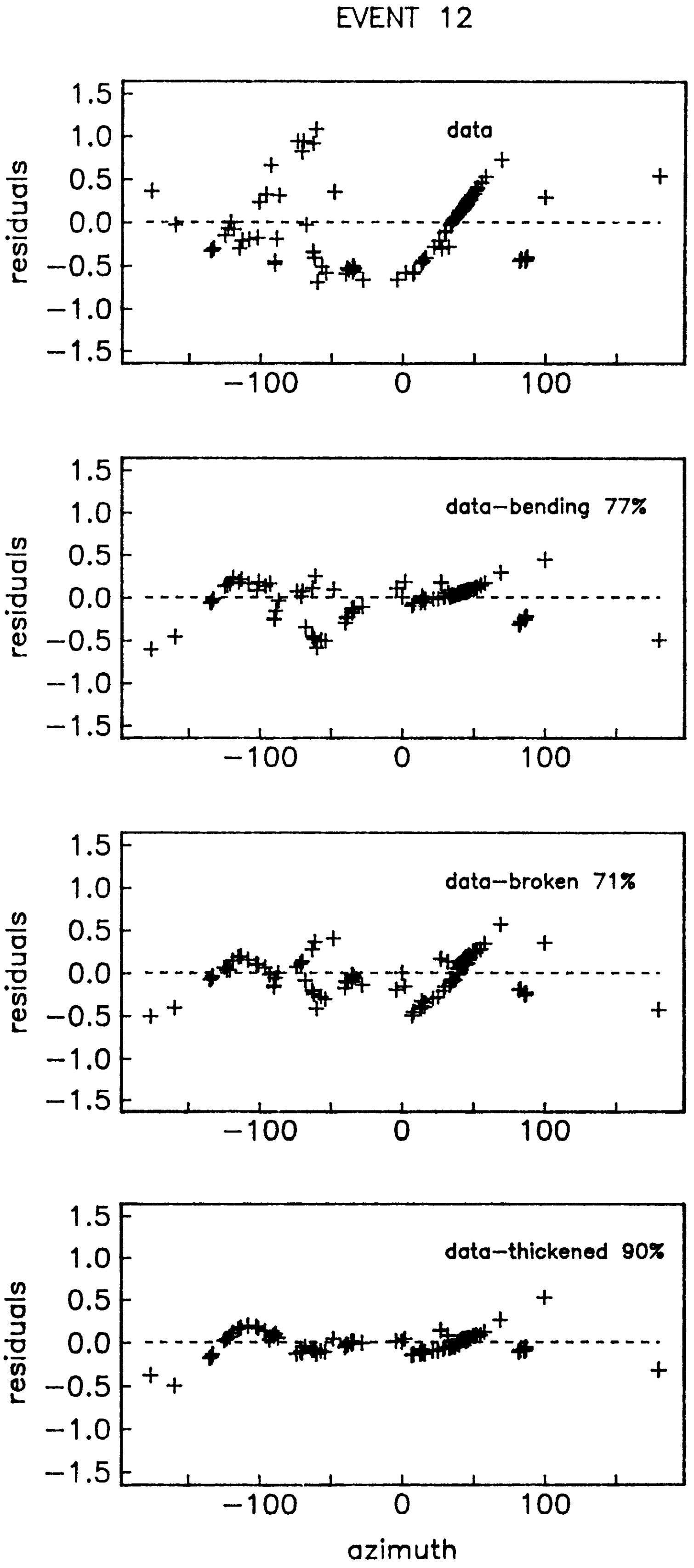

EVENT 12

Figure 3.9

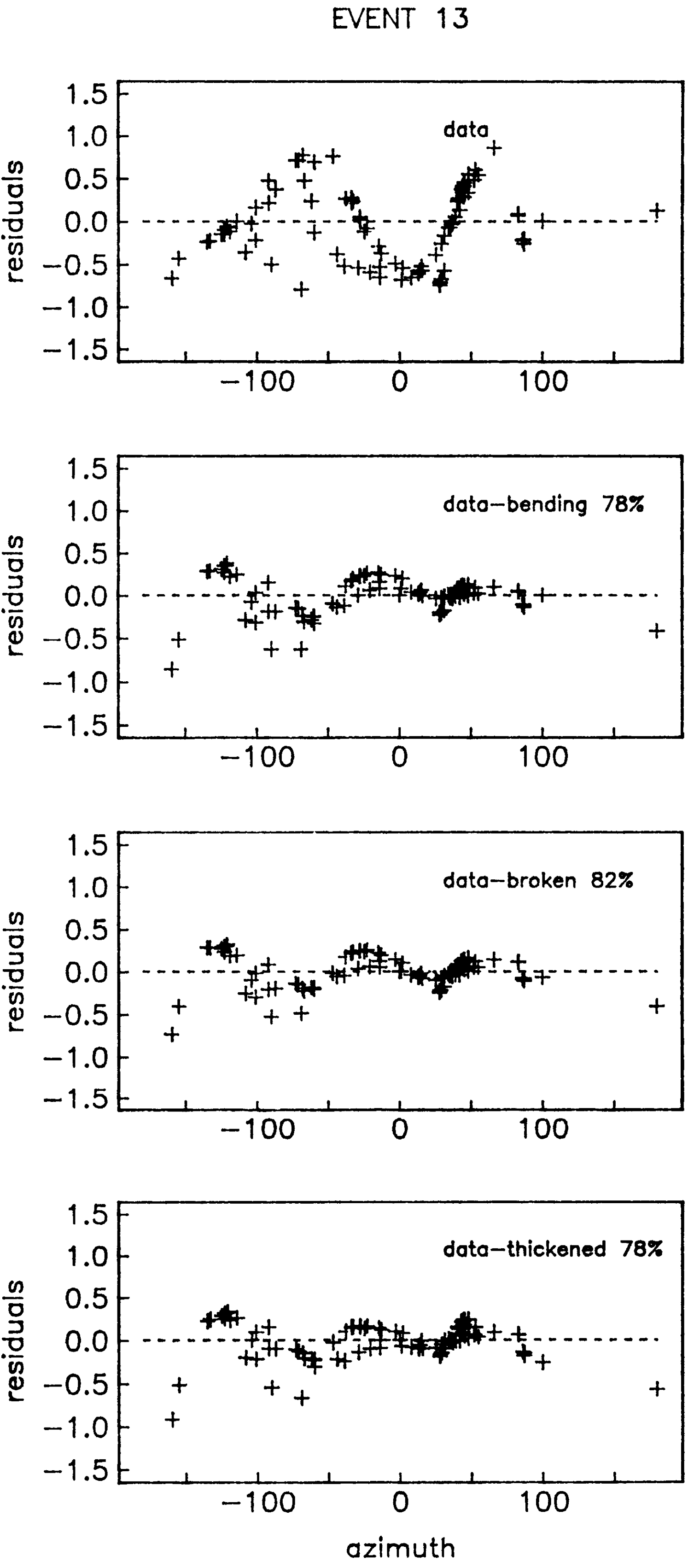
EVENT 13
data
data–bending 78%
data–broken 82%
data–thickened 78%
residuals
1.5
1.0
0.5
0.0
−0.5
−1.0
−1.5
−100
0
100
azimuth

Figure 3.9

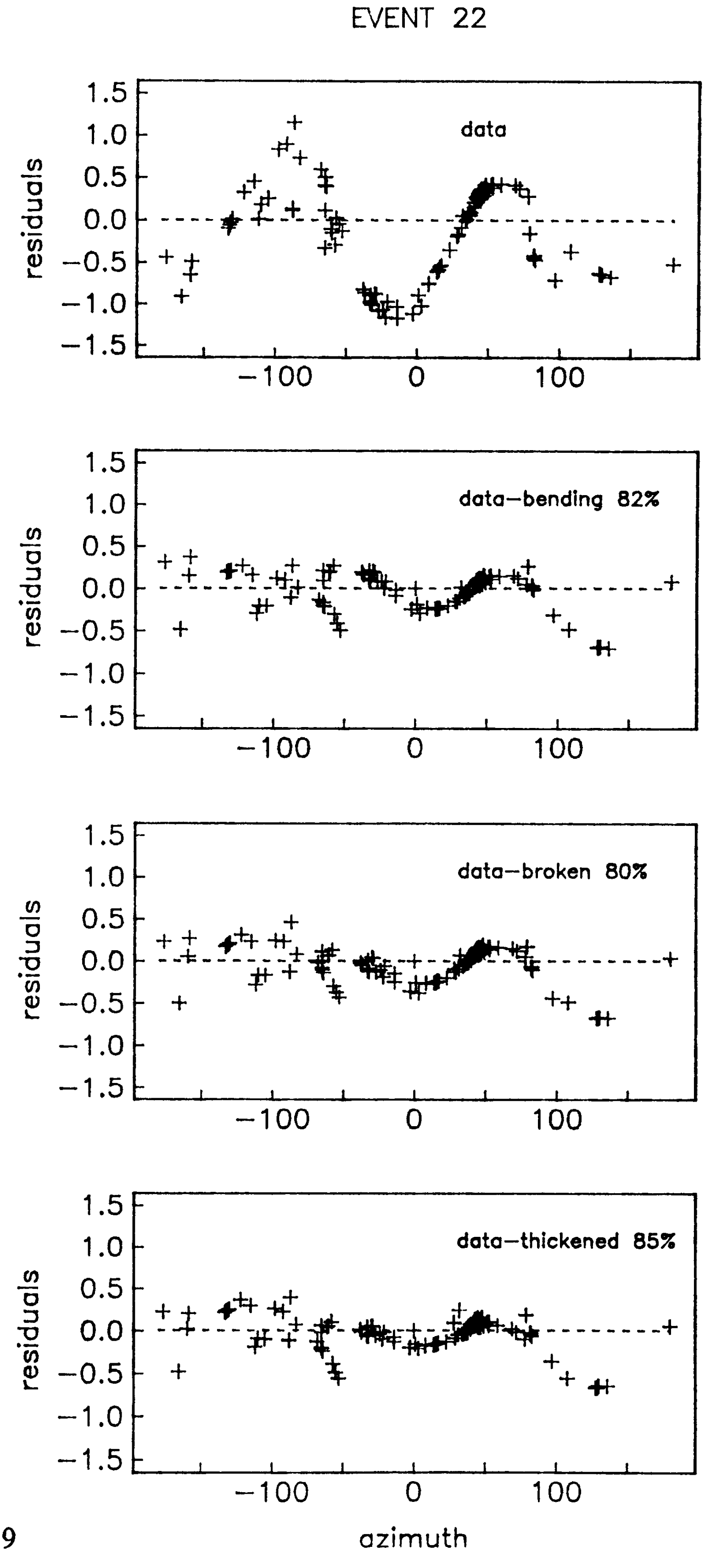
EVENT 22
data
data—bending 82%
data—broken 80%
data—thickened 85%
residuals
1.5
1.0
0.5
0.0
−0.5
−1.0
−1.5
−100
0
100
azimuth

Figure 3.9

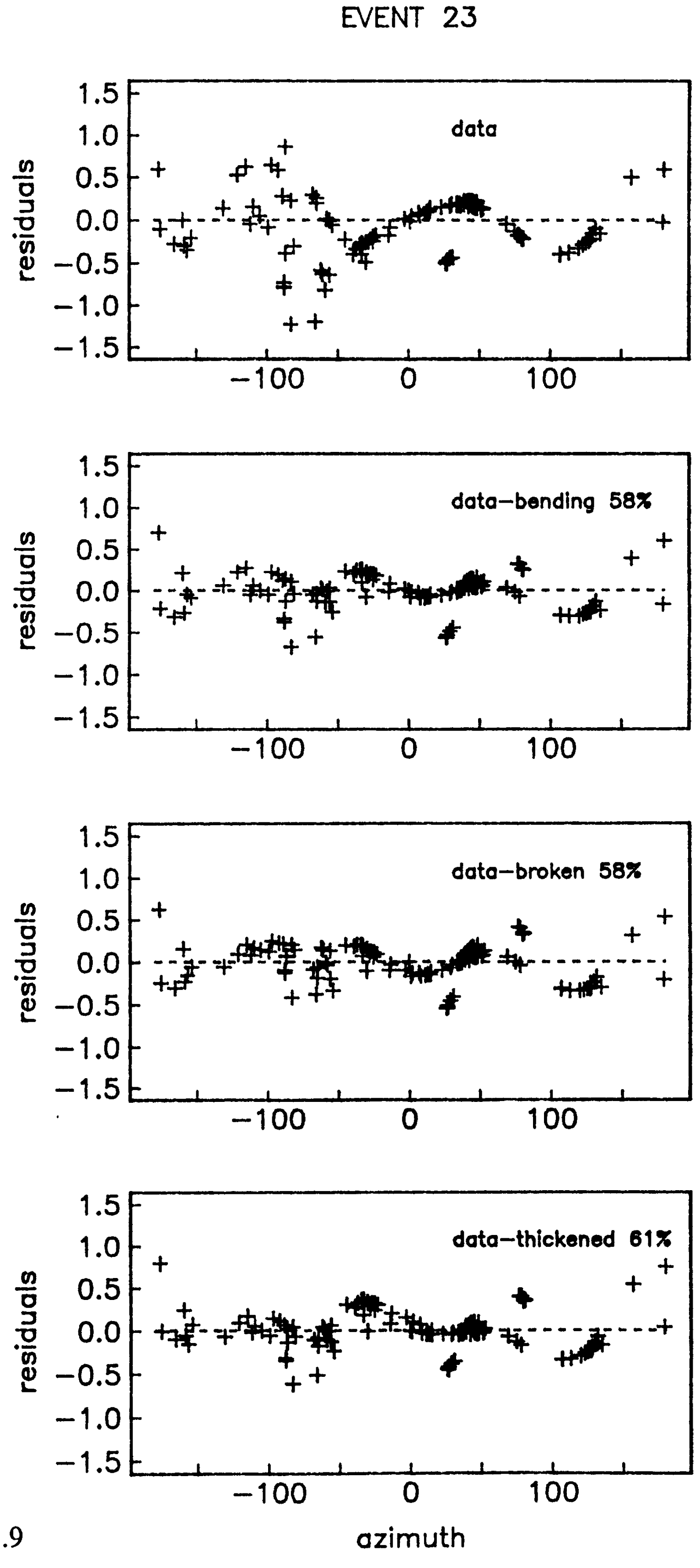
EVENT 23
data
data-bending 58%
data-broken 58%
data-thickened 61%
residuals
1.5
1.0
0.5
0.0
−0.5
−1.0
−1.5
−100
0
100
azimuth

Figure 3.9

Figure 3.10. Variation in local values of slab strike and dip demonstrated by residual sphere projections of $\mathbf{t_s} - \mathbf{c_R}$ minus a mean value for the bending model parameterization. The synthetic data are neither relocated nor smoothed and they are displayed on the residual sphere as a continuous function in azimuth and take-off angle. Regions reporting negative times are blue and those reporting positive times are red. White line in each residual sphere indicates the strike and dip values from Table 1. Hypocentral dataset in seismicity basemap is identical to that in Figure 3.2. Numbers indicate locations of 25 modeled events; earthquakes deeper than 400 km are shown in red, those between 10 km and 300 km in blue.

Figure 3.10

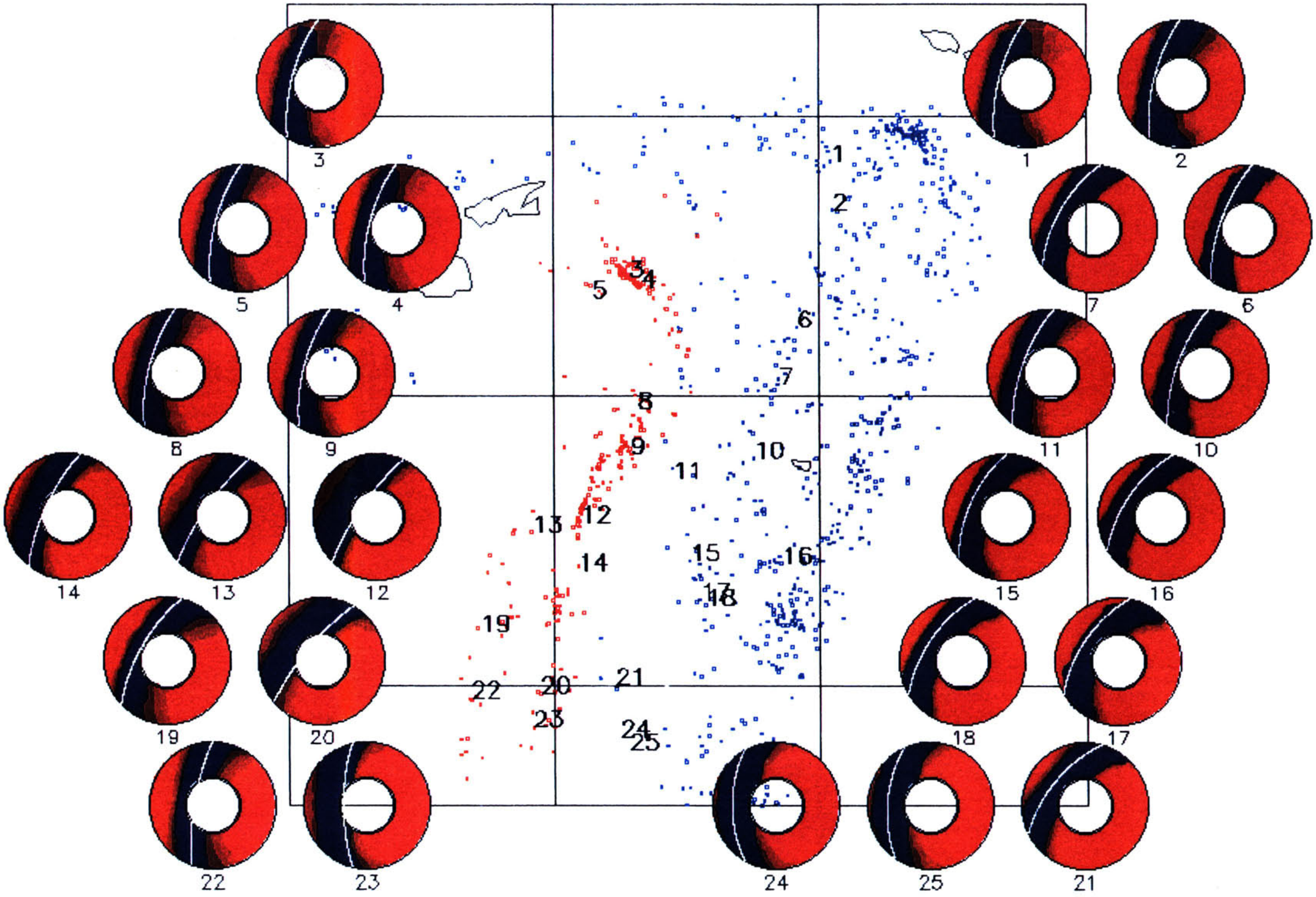
3
1
2
1
2
5
4
7
6
3
4
5
6
8
9
7
11
10
8
9
10
11
14
13
12
13
12
15
16
14
15
16
17
18
19
19
20
18
17
22
20
21
23
24
25
22
23
24
25
21

Figure 3.11. Contours of seismic velocity (0.25 km/s) for the best-fitting bending slab models in northern (A – A'; B – B'), central (C – C') and southern (D, E – D', E') Tonga. Profile locations and seismicity shown in map-view in Figure 3.2.

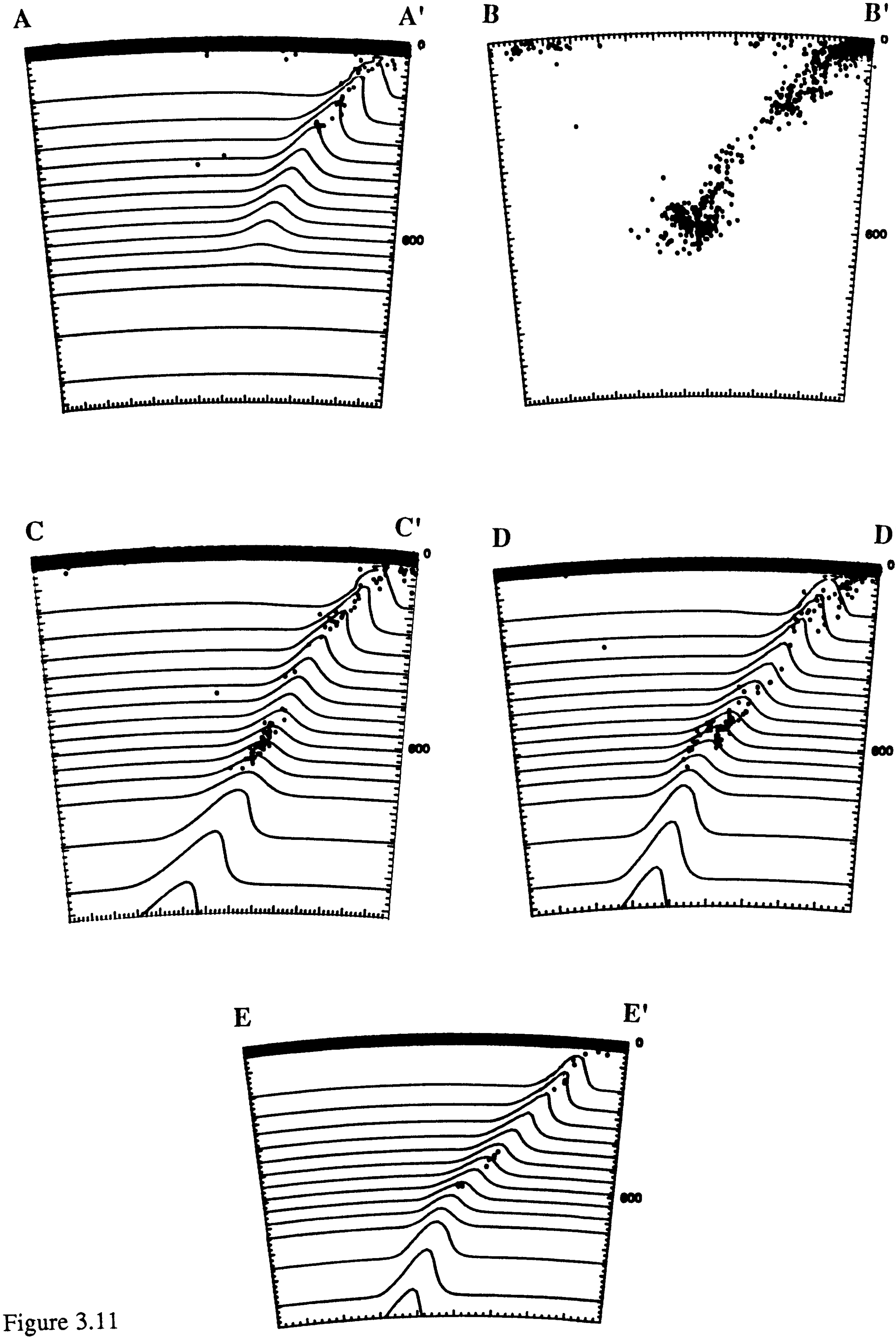

Figure 3.11

Figure 3.12. Schematic diagram showing proposed distribution of subducted lithosphere from *Hamburger and Isacks* [1987]. Lines represent 100 km contours to the top of the subducted lithosphere. Dashed lines sub-parallel to the trend of the ancestral Vityaz trench indicate subducted Vityaz slab. Dotted lines delineate other detached lithosphere.

Hamburger and Isacks: Deep Earthquakes in the Southwest Pacific

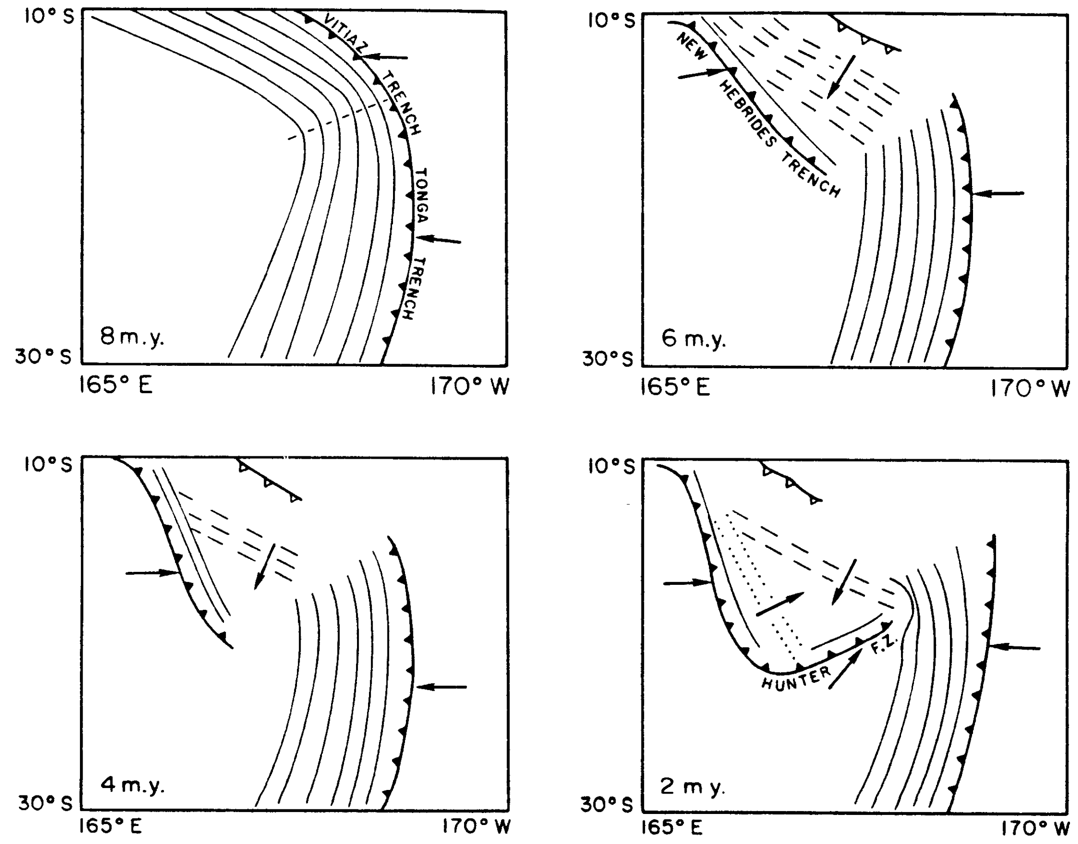

Figure 3.12

Figure 3.13. Schematic diagram of possible slab structure (shaded areas) overlain on observed seismicity in northern (A – A'; B – B'), central (C – C') and southern (D, E – D', E') Tonga. The degree of advective thickening perpendicular to the arc shown by the shading is consistent with, but not required by, travel time data. Hypocentral data and profile locations correspond to Figure 3.2. In profile B – B', Vityaz slab fragment (bold lines) intersects Tonga lithosphere below 450 km depth.

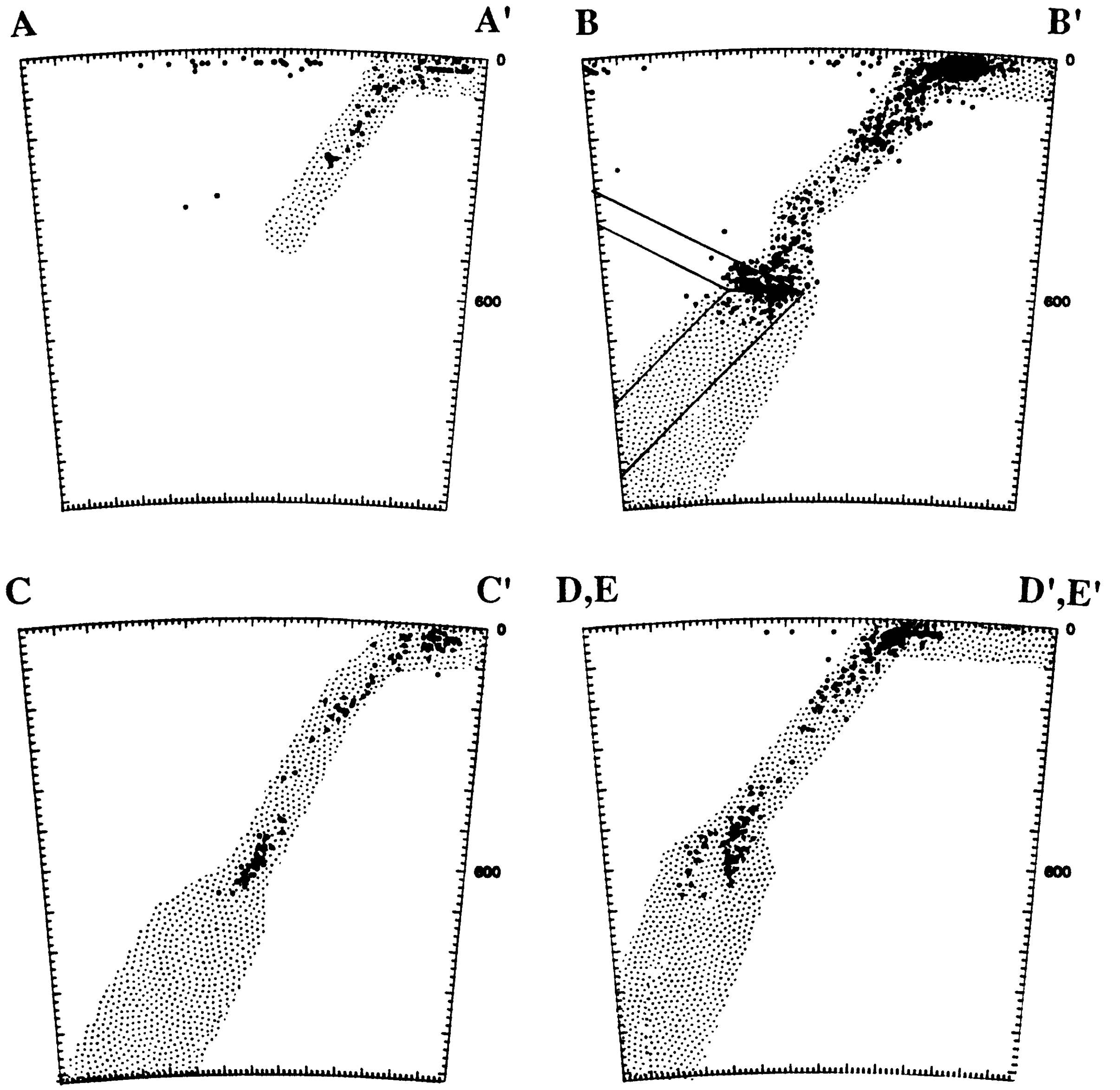

Figure 3.13

CHAPTER 4

SEISMIC STRAIN AND DEEP SLAB DEFORMATION

INTRODUCTION

Residual sphere analysis of travel time data from earthquakes in the Kuril-Kamchatka, Mariana [*Jordan,* 1977; *Creager and Jordan,* 1984, 1986] and Tonga [chapter 3] subduction zones requires that the descending lithosphere extends to depths of 800 km – 900 km or more. In all of these arcs, however, seismicity and source mechanism data indicate that the deep slab may be deforming as it penetrates the lower mantle. Much of this thesis [chapter 2 and chapter 3; *Fischer et al.,* 1988] is an analysis of the constraints which travel time data place on the morphology of the deep lithosphere. These results estimate slab deformation integrated over time, that is, finite strain. Earthquake source mechanisms, however, measure strain rate or infinitesmal strain. In this study we return to the source data in Tonga in an effort to further constrain the scale of advective deformation in the deep slab, and to elucidate the mode in which it may occur.

Down-dip compressional focal mechanisms suggest that the lithosphere encounters resistance at the 650-km discontinuity [*Isacks and Molnar,* 1969, 1971; *Richter,* 1979; *Vassiliou,* 1984; *Giardini,* 1984; *Giardini and Woodhouse,* 1984, 1986; *Apperson and Frohlich,* 1987], and an increase in viscosity between the upper and lower mantle is one mechanism that could cause the slab to slow and deform while passing through the 650-km discontinuity [*Gurnis and Hager,* 1988]. Compression of the deep slab must be balanced by outward flow of slab material, however. In the Tonga subduction zone, seismicity and earthquake moment tensor solutions suggest that in response to down-dip compression, lithospheric material is being laterally displaced perpendicular to the arc [*Giardini and Woodhouse,* 1984] and has undergone substantial shearing parallel to slab strike [*Giardini and Woodhouse,* 1986]. By examining lineations in the seismicity local to the hypocenter associated with a given source mechanism, *Giardini and Woodhouse* [1986] determined which of the two nodal planes is the more likely fault plane. The chosen slip vectors almost invariably dip to the north, which, given the predominantly down-dip compression axes, indicates that the older, deeper slab has been displaced southward relative to the shallow structure.

The pattern of flow suggested by the deep-focus earthquake source mechanisms is consistent with seismic estimates of finite strain. Residual sphere analysis of travel time data from the Tonga, Kuril-Kamchatka and Mariana arcs has yielded constraints on slab structure which are consistent with considerable advective deformation. In Kuril-Kamchatka and the Marianas, this deformation may take the form of advective thickening of the slab perpendicular to its strike [chapter 2; *Fischer et al.,* 1988], while in Tonga such a flow may be perpendicular or parallel to the arc [chapter 3]. The constraints which travel time data place on advective thickening of the slab perpendicular to its strike are fairly broad, due to the effects of three-dimensional ray bending. In chapter 2 we introduced the thickening factor γ, the total width of the thickened slab perpendicular to its strike divided by undeformed slab width. While travel time residuals from the Kuril-Kamchatka arc can tolerate γ's of up to three, Tonga data permit γ's of at least three, and Mariana data allow γ's of five or more. Travel times from all three arcs are also all fit by models which enter the lower mantle undeformed [*Fischer et al.,* 1988; chapter 2 and chapter 3].

In constrast, interpretations of slab structure and seismicity estimate shearing parallel to the strike of the Tonga slab to be on the order of 300 km – 500 km. Travel times from deep-focus events in northern Tonga require slab penetration into the lower mantle between 17° S and 26° S, but northward of 17° S intermediate-focus earthquake data rule out slab material much deeper than 500 – 600 km; this apparent shallowing of maximum slab depth is mirrored by a similar trend in the seismicity (Figure 4.1) documented by *Louat and Dupont* [1972] and *Giardini and Woodhouse* [1986]. The amount of along-arc shear in central Tonga (19°S – 21.5° S) may be somewhat larger. *Giardini and Woodhouse* [1984] suggest that a gap in the deep seismicity at 22° S – 23° S (Figure 4.1) represents the signature of the subducting Louisville Ridge, an aseismic seamount chain [*Larson and Chase,* 1972] whose surface expression intersects the Tonga trench at 25° S. The deep gap in seismicity lies some 500 km to the south of where tectonic reconstructions of down-dip displacement indicate the subducted Louisville Ridge ought to lie. The degree of shearing parallel to the arc in southern Tonga (21.5°S – 27° S) is unknown.

Although a model which includes along-arc shear and a roughly constant amount of cross-strike thickening at all latitudes in the deep slab is appealing in its simplicity, nothing in the seismicity nor in the structure determined from travel time data conclusively supports such a pattern of deformation. In fact, as we saw in chapter 3, the structure of the deep Tonga slab varies considerably along the arc. In northern Tonga (13°S – 19° S), a westward hook in the deep seismicity (Figure 3.2) may be explained by the collision of the northward striking Tonga slab with a remnant slab fragment located in the lower mantle to its west. In contrast, the strike and dip of seismicity and slab structure in central Tonga are relatively constant with depth and latitude, and, in southern Tonga, travel time data require that slab dip increases below roughly 500 km, and deep seismicity is imbricated into two parallel planes separated by roughly 100 km in the cross-strike direction (Figure 3.13).

Since an earthquake source mechanism estimates local strain rate, summing the total seismic slip in particular volumes of slab allows us examine variations in the pattern of flow throughout the subducting lithosphere. A primary goal of this study is to determine the amounts of moment release which go into flow perpendicular versus parallel to strike. We also examine the relationship of the strain rate data to estimates of finite strain in the Tonga lithosphere, investigating possible flow models for the deep slab and the degree to which deformation may be aseismic.

INFINITESMAL SEISMIC STRAIN

Our goal in this section is to map variations in seismic strain rate throughout the deep Tonga slab. Given that travel time data reveal a structure for the Tonga slab which varies considerably along the arc, the deforming flow may also. The problem may be divided into two parts. We determine a spatially varying description of the geometry of observed strain rate, that is, the relative sizes of the strain rate components, and we constrain the scalar value of strain rate as a function of latitude.

Constraining average strain rate geometry

A first step in this analysis is to find a description of seismic strain which can be easily related to the morphology of the deep slab. A moment tensor is a 3 × 3 matrix whose components describe the source function of a given earthquake, and the Harvard Centroid Moment Tensor Catalog provides a compilation of these source functions obtained by inversion of wavefrom data [*Dziewonski, et al.*, 1981]. The orientations of the compression (maximum shortening) and tension (maximum extension) axes for the individual Harvard CMT solutions in the deep Tonga slab yield a qualitative sense of the seismic strain throughout the subduction zone (Figure 4.2 shows the data for 1977 – 1986; *Dziewonski and Woodhouse*, 1983; *Dziewonski et al.*, 1983abc, 1984abc, 1985abcd, 1986abc, 1987abcdefg, 1988abcd; *Giardini*, 1984). However, while certain trends, such as the roughly northwest (approximately down-dip) orientation of the pressure axes are discernible, a more quantitative mapping of seismic strain is clearly necessary if we are to estimate the ratio of cross-strike to along-arc deformation.

Several formulations for averaging individual earthquake data have been presented in the literature. Some examples are summing fault slip according to *Brune's* [1968] relation; combining polarity data [*Schneider and Sacks*, 1987]; and determining the principal axes which best fit suites of nodal plane orientations [*Gephart and Forsyth*, 1984; *Gephart*, 1985].

However, *Kostrov* [1974] suggests a complete and mathematically simple expression of average seismic strain:

$$2\mu T V\dot{\bar{\varepsilon}} = \sum_{i=1}^{N} \mathbf{M}_i \tag{4.1}$$

where $\dot{\bar{\varepsilon}}$ is the 3×3 tensor describing the average strain rate in a volume V over a time interval T, $\mathbf{M}$ are the moment tensors for the N events ocurring in that volume and time, and μ is the shear modulus. This approach and variations upon it have been adopted by several authors in continental regions where a problem of particular interest is comparing seismic strain with relative surface plate motions [*Chen and Molnar,* 1977; *Molnar,* 1983; *McKenzie and Jackson,* 1983; *Molnar and Qidong,* 1984; *Jackson and McKenzie,* 1988].

The relationship of average strain rate to local strain rate, $\dot{\varepsilon}$, is elucidated by writing

$$\dot{\varepsilon} = 1/2\,(\mathbf{L} + \mathbf{L}^{\mathrm{T}}) \tag{4.2}$$

where $\mathbf{L}$ is the velocity gradient tensor

$$L_{ij} = \partial v_i \,/\, \partial x_j \qquad i,j = 1,2,3 \tag{4.3}$$

v is the Eulerian particle velocity and x represents the spatial coordinates. This notation is based on that of *Malvern* [1969] and *Jackson and McKenzie* [1988]. $\dot{\varepsilon}$ is known at every point in the deforming volume and integrating it over this volume yields $\dot{\bar{\varepsilon}}$:

$$\int_V \dot{\varepsilon}'\, dV = V\dot{\bar{\varepsilon}} = \mathbf{E}' \tag{4.4}$$

The relative sizes of the components of **E** govern the ratio of cross-strike to along-arc strain rate. In order to examine this flow geometry meaningfully, however, we also must determine how well constrained these components are. We make the assumption that the error in average strain rate is described by an unbiased estimate of the standard error in the mean of the moment tensor data which make up **E**. We do not separate out that component of the dispersion which is caused by errors in the moment tensor solutions themselves. We simplify the error analysis with the vector isomorphism of *Silver and Jordan* [1982]. The 3 × 3 tensor **E** becomes the 6 element vector **e** where:

$$e_1 = E_{11},\ e_2 = E_{22},\ e_3 = E_{33} \qquad (4.5)$$

$$e_4 = \sqrt{2}E_{12},\ e_5 = \sqrt{2}E_{13},\ e_6 = \sqrt{2}E_{23}$$

In this analysis we must account for the fact that **e** is computed from tensors of varying scalar moment, M_o :

$$\mathbf{e} = \int \mathbf{e}(M_o)\, dM_o \qquad (4.6)$$

and is dominated by the contributions from the largest earthquake sources. If we knew our data were complete for the largest deep-focus events, a weighting for M_o could be included in the error analysis. However, the Harvard CMT Catalog spans the years 1977 – 1986, too short an interval to accurately represent the largest events. We therefore introduce the approximation that the average strain rate vectors obtained by summing intermediate size events accurately represent strain rate for the entire range of observed M_o. That is, we assume that **e** is not a strong function of M_o. Fortunately, the Harvard Catalog is quite complete for intermediate moments [*Ekstrom and Dziewonski*, 1988]. It contains a strong peak in the range 1×10^{17}N m $\leq M_o \leq 1 \times 10^{18}$N m (Figure 4.3), and we choose to approximate the average strain rate vector with **e** computed for this moment interval alone. We will return to the validity of this simplification somewhat later in this section.

Under this assumption we redefine **e**:

$$\mathbf{e} = \sum_{i=1}^{N} \hat{\mathbf{m}}_i \tag{4.7}$$

where $\hat{\mathbf{m}}$ is the vector isomorphic to **M** normalized so that

$$\hat{\mathbf{m}}_i^T \cdot \hat{\mathbf{m}}_i = 1 \tag{4.8}$$

We make the assumption that each $\hat{\mathbf{m}}$ may be considered as a sample of a random and independently distributed stochastic process whose probability density function can be approximated as a Gaussian distribution on a plane tangent to the vector $\hat{\mathbf{m}}_0$. The mean of this distribution is

$$\langle \hat{\mathbf{m}} \rangle = \hat{\mathbf{m}}_0 \tag{4.9}$$

and its variance equals

$$\mathbf{V}_{\hat{\mathbf{m}}} = \langle (\hat{\mathbf{m}}_i - \hat{\mathbf{m}}_0)\ (\hat{\mathbf{m}}_i - \hat{\mathbf{m}}_0)^T \rangle \tag{4.10}$$

[*Silver and Jordan,* 1982]. The expected value of **e** is therefore

$$\langle \mathbf{e} \rangle = N\, \hat{\mathbf{m}}_0 \tag{4.11}$$

and

$$\langle \mathbf{e}\, \mathbf{e}^T \rangle = N\, \mathbf{V}_{\hat{\mathbf{m}}} + N^2\, \hat{\mathbf{m}}_0\, \hat{\mathbf{m}}_0^T \qquad (4.12)$$

which yields the normalized variance matrix:

$$\mathbf{V}_{\hat{\mathbf{e}}} = \frac{1}{N^2}\,(\mathbf{I} - \hat{\mathbf{m}}_0\, \hat{\mathbf{m}}_0^T)\, \mathbf{V}_{\mathbf{e}}\, (\mathbf{I} - \hat{\mathbf{m}}_0\, \hat{\mathbf{m}}_0^T) = \frac{1}{N}\, \mathbf{V}_{\hat{\mathbf{m}}} \qquad (4.13)$$

In order to obtain $\tilde{\mathbf{V}}_{\hat{\mathbf{e}}}$, we estimate the mean and the variance of the process $\hat{\mathbf{m}}$ based on our finite number of observations:

$$\tilde{\mathbf{m}}_0 = \frac{1}{n} \sum_{k=1}^{n} \hat{\mathbf{m}}_k \qquad (4.14)$$

$$\tilde{\mathbf{V}}_{\hat{\mathbf{m}}} = \frac{1}{n-1} \sum_{k=1}^{n} (\hat{\mathbf{m}}_k - \tilde{\mathbf{m}}_0)\, (\hat{\mathbf{m}}_k - \tilde{\mathbf{m}}_0)^T \qquad (4.15)$$

$\tilde{\mathbf{V}}_{\hat{\mathbf{m}}}$ is an unbiased estimator; that is,

$$\langle \tilde{\mathbf{V}}_{\hat{\mathbf{m}}} - \mathbf{V}_{\hat{\mathbf{m}}} \rangle = 0 \qquad (4.16)$$

In practice, however, the dispersion of $\hat{\mathbf{m}}$ about $\tilde{\mathbf{m}}_0$ is not small, as evidenced by typical values of $\tilde{\mathbf{m}}_0$ in Tonga which are significantly less than unity. We therefore make the assumption that we can retain the Gaussian description of variance if we project the difference vectors $\hat{\mathbf{m}}_k - \tilde{\mathbf{m}}_0$ onto the tangent plane perpendicular to $\tilde{\mathbf{m}}_0$ with the operator $\mathbf{Q}$ (Figure 4.4).

$$\mathbf{Q} = \mathbf{I} - \mathbf{m}_0\, \mathbf{m}_0^T \qquad (4.17)$$

and $\widetilde{V}_{\hat{e}}$ is now written

$$\widetilde{V}_{\hat{e}} = \frac{1}{n(n-1)} \sum_{k=1}^{n} \mathbf{Q}\,(\hat{\mathbf{m}}_k - \widetilde{\mathbf{m}}_0)\;(\hat{\mathbf{m}}_k - \widetilde{\mathbf{m}}_0)^T\,\mathbf{Q} \tag{4.18}$$

If the distribution of $\hat{\mathbf{m}}$ is Gaussian, $\hat{\mathbf{m}}_k - \widetilde{\mathbf{m}}_0$ by definition lies in the tangent plane perpendicular to $\widetilde{\mathbf{m}}_0$. The operator **Q** then has no effect and equation 4.18 reduces to 4.15.

Equations 4.7 and 4.18 provide us with the quantitative tools to describe the average strain rate caused by the earthquakes in a given volume of slab. Given our task of comparing observed seismic strain rate to variations in deep slab structure, we must compute **e** over volumes small enough to resolve the major morphologic variations between northern, central and southern Tonga, 13° S – 19° S, 19° S – 21.5° S, and 21.5° S – 27° S, respectively. The volumes must be large enough, however, to contain enough individual moment tensors to meaningfully constrain the six-element vector **e**. We identify the moment tensor solutions reported in the Harvard CMT Catalog which lie in the Tonga subduction zone between 500 and 700 km depth and bin them in volumes whose remaining dimensions are 1° latitude by 1° or 2° longitude (bin locations are shown in Figure 4.5). From 16° S – 22° S the bins were defined to include all of the deep-focus seismicity. Between 22° S – 26° S, however, only events in the eastern band of the imbricated deep seismicity are included. Three bins containing fewer than five CMT solutions were discarded, and for the remaining six we calculate **e** and $\widetilde{V}_{\hat{e}}$ which are displayed in Figure 4.5 using the moment tensor formalism of *Riedesel and Jordan* [1988].

Riedesel and Jordan [1988] develop a system of describing individual moment tensors based on linear combinations of their eigenvectors and eigenvalues. This analysis may be applied to strain rate tensors if one bears in mind that rather than describing an individual source mechanism, we now are looking at the sum of source mechanisms throughout a volume. For instance, if a moment tensor is best descibed as a compensated linear vector dipole (CLVD), that fact reflects the source process of the earthquake. If a strain rate tensor is close to a CLVD, however, the individual moment tensors comprising it may each have a significant CLVD component, or they may be individually largely double-couple but sum to a CLVD. The latter case is what we observe in Tonga. For example, if two double-couple moment tensors with the same principal axes occur in the same volume of slab, they yield a double-couple strain rate tensor. If the null and tension axes of one of the moment tensors is rotated by 90° about the compression axis, however, their sum is a CLVD.

Following *Riedesel and Jordan* [1988] we define

$$
\begin{aligned}
\hat{\lambda} &= \sum_{i=1}^{3} \lambda_i \hat{\Psi}_i \\
\hat{\mathbf{d}} &= (\hat{\Psi}_1 - \hat{\Psi}_3)/\sqrt{2} \qquad\qquad (4.19) \\
\hat{\mathbf{i}} &= \sqrt{\tfrac{2}{3}}\left(\tfrac{1}{2}\hat{\Psi}_1 - \hat{\Psi}_2 + \tfrac{1}{2}\hat{\Psi}_3\right)
\end{aligned}
$$

λ_i and $\hat{\Psi}_i$ are the eigenvalues and eigenvectors, respectively, of the tensor isomorphic to **e**, and $\lambda_1 \geq \lambda_2 \geq \lambda_3$. $\hat{\lambda}$ characterizes the type of source mechanism implied by **e**. If the source mechanism is largely double-couple, then $\hat{\lambda}$ lies close to $\hat{\mathbf{d}}$ on the lower focal hemisphere plots in Figure 4.5, and if it is a compensated linear vector dipole, $\hat{\lambda}$ approximates $\hat{\mathbf{i}}$. $\hat{\mathbf{P}}$, $\hat{\mathbf{T}}$ and $\hat{\mathbf{N}}$ show the directions of $\hat{\Psi}_3$, $\hat{\Psi}_1$ and $\hat{\Psi}_2$, respectively. If the source mechanism describing strain rate is a double-couple, then $\hat{\mathbf{P}}$, $\hat{\mathbf{T}}$ and $\hat{\mathbf{N}}$ correspond to the compression, tension and null axes. $\hat{\mathbf{d}}$ and $\hat{\mathbf{i}}$ lie on the dashed great circle which represents the vector-space of all deviatoric mechanisms, and since moment tensors in the Harvard Catalog are constrained to have zero trace, $\hat{\lambda}$ will also always lie on this great circle.

Marginal error ellipses for $\hat{\mathbf{P}}$, $\hat{\mathbf{T}}$, $\hat{\mathbf{N}}$ and $\hat{\lambda}$ [*Riedesel and Jordan*, 1988] are constructed from the normalized variance matrix for the complete strain rate vector, $\tilde{\mathbf{V}}_{\hat{e}}$, the error ellipses in Figure 4.5 correspond to the 95% confidence level. Since the marginal uncertainties displayed do not account for trade-off among errors in the eigenvectors, these error ellipses are only significant in evaluating discrepancies between **e** and strain rate vectors with the same eigenvectors. This limitation does not effect our ability to determine whether **e** is a double-couple at the 95% confidence level, or whether it also contains a significant CLVD component.

Before discussing the observed average strain rate tensors in detail, however, let us use the *Riedesel and Jordan* [1988] formalism to re-examine the assumption that **e** is not a strong function of M_O on which the above error analysis is in part based. Simply, if this assumption is valid, average strain rate vectors for the same volume, but computed from events in different magnitude bands, should look the same. Of the nine volumes in which we computed **e**, only one (20° – 21° S) contained enough earthquakes to yield estimates of strain rate for moment bands outside the standard range of 1×10^{17}N m $\leq M_O \leq 1 \times 10^{17}$N m. Figure 4.6 shows **e** computed for events in this slab volume in the moment bands 1×10^{16}N m $\leq M_O \leq 1 \times 10^{17}$N m and 1×10^{18}N m $\leq M_O \leq 1 \times 10^{19}$N m, in addition to the standard strain rate vector also shown in Figure 4.5. The similarity between these different strain rate estimates indicates that **e** is quite independent of the size of the earthquakes from which it is calculated, and supports our assumption that **e** is not a strong function of M_O.

The direction of maximum shortening

The strain rate vectors for the deep Tonga slab may be characterized by two first order features. First, the direction of maximum shortening, $\hat{\mathbf{P}}$, lies in the northwest quadrant of the lower focal hemisphere, with the exception of bin N1. Second, the northern Tonga bins (N1 and N2) contain a significant CLVD component, but the geometry of strain rate becomes progressively more double-couple to the south. Before we interpret the extensional strain rate components, we compare $\hat{\mathbf{P}}$ with the down-dip azimuth and plunge of the slab to determine whether the lithosphere is compressing parallel to its trajectory. The strike and dip values summarized in Table 1 describe the geometry of the upper mantle portion of the Tonga slab determined in chapter 3. While certain slab models were found to satisfy the travel time data for intermediate-focus earthquakes between 17° S and 19° S, no simple parameterization matched the seismicity as well, hence for these latitudes we leave slab dip in the upper mantle untabulated; an average value of greater than 50° is likely, however.

From 18° S to 25° S $\widehat{\mathbf{P}}$ lies within 20° of the down-dip azimuth and plunge of the slab, and shifting the observed $\widehat{\mathbf{P}}$ axes to an exactly down-dip orientation would vary the other strain rate components by less than 10%. That is, for the purposes of analyzing the relative sizes of the other components, $\widehat{\mathbf{P}}$ may be described as down-dip. However, given the error ellipses associated with the $\widehat{\mathbf{P}}$ axes in Figure 4.5 and the fact that the travel time estimates of slab strike and dip in Table 1 have uncertainties of ± 10° and ± 5°, respectively, a small component of compression oblique to slab structure is resolved in three of the five bins. In central Tonga, volumes C1 and C2 (20° – 22° S), the azimuth of $\widehat{\mathbf{P}}$ is slightly too far north and its plunge too shallow to be described as exactly down-dip, and in bin S1 (22° – 23° S) $\widehat{\mathbf{P}}$ lies at an azimuth E of down-dip. While no obvious explantion exists for the central Tonga data, the fact that S1 lies at the transition between the relatively planar seismicity of central Tonga and the imbricated deep-focus zone in southern Tonga suggests that this feature may indicate a shift in the flow pattern. Clearly the dynamics of deep subduction in southern Tonga are complex. Individual source mechanisms in the western branch of the double zone vary consistently from those in the east, leading us to exclude them from bins S1 and S2. The strain rate vectors in each of the two bands from 22° S to 26° S (Figure 4.7) illustrate that while the deep slab is compressing on average parallel to its trajectory in the eastern band, in the western band $\widehat{\mathbf{P}}$ dips to the east back under the subducting lithosphere. The individual compression axes for 21 out of 22 events in the eastern band dip to the east, but in the western band, only 2 out of 6 do. The imbricated bands appear to sample different points in a spatially varying flow-field and perhaps delineate separate slab fragments.

Of all the slab volumes studied, the direction of maximum shortening in N1 (17° – 18° S) deviates the most from the down-dip plunge and azimuth of the slab. While the dip of the upper mantle lithosphere in these latitudes is not well constrained, it is certainly greater than 50° (chapter 3), leaving a discrepancy of at least 5° in plunge and 15° in azimuth between $\widehat{\mathbf{P}}$ and the dip of the slab structure. This result may reflect the same tectonic complexity in northern Tonga which was invoked in chapter 3 to explain deviations between slab structure inferred from travel time data and the shape of the downgoing seismicity. One of the most noted features in Tonga seismicity is the westward hook in the deep-focus zone at the northern end of the arc (Figure 4.5). However, while previous authors have taken this feature to indicate a bend in slab structure [*Sykes,* 1966; *Billington and Isacks,* 1975; *Billington,* 1980; *Giardini and Woodhouse,* 1984, 1986; *Hamburger and Isacks,* 1987], residual spheres for five earthquakes within the hook indicate that the northern end of the slab in fact strikes east of north. The trend of the deep seismicity therefore cuts across the deep structure, and an appealing explanation for the orientation of this band of events is that it marks the intersection of the downgoing lithosphere and a remnant slab fragment from the ancestral Tonga-Vityaz subduction zone configuration [*Isacks and Barazangi,* 1977; *Hamburger and Isacks,* 1987]. According to the *Hamburger and Isacks* [1987] reconstruction an upper corner of the Vityaz slab hits the Tonga lithosphere with an along-arc strike that roughly matches the most northern Tongan deep-focus events, W 35° N, perpendicular to the azimuth of $\widehat{\mathbf{P}}$ in bin N1. In the N1 region, therefore, earthquake travel time data appear to reflect the strike and dip of the Tonga slab, while strain rate data are more consistent with the geometry of the Vityaz slab fragment. This result may indicate that the events lie within Vityaz lithosphere, but raypaths emanating from them preferentially sample the Tonga slab, a geometry which would require a shallow dip (< 30°) for the Vityaz fragment.

Along-arc versus cross-strike strain rate

The second first order feature in the observed strain rate vectors is that while the error bars for $\hat{\lambda}$ intersect $\hat{\mathbf{d}}$ in the southern Tonga slab volumes (S1 and S2), $\hat{\lambda}$ lies in between $\hat{\mathbf{l}}$ and $\hat{\mathbf{d}}$ in central Tonga (C1 and C2), and nearer to $\hat{\mathbf{l}}$ in northern Tonga (N1 and N2). That is, at the 95% confidence level average strain rate in southern Tonga may be described as double-couple, the CLVD component increases in central Tonga, and the northern Tonga data are purely CLVD. The moment tensor solutions which comprise the strain rate vectors in Figure 4.5 are very close to double-couple on an individual basis, and in general their compression axes lie roughly down-dip. The central and northern Tonga strain rate tensors must therefore be comprised of individual mechanisms whose null and tension axes vary, while in southern Tonga the individual tension axes in general lie in the cross-strike direction and the null axes along-strike. A simple physical explanation of this phenomenon is that while compression of the slab in southern Tonga is balanced by thickening in the cross-strike direction, the relative size of the along-arc strain rate component increases south to north.

Modeling seismic strain rate vectors

In order to quantify the variation in strain rate geometry, we model observed strain rate, $\mathbf{e}$, with theoretical strain rate vectors ($\mathbf{e}'$) in which down-dip compression is balanced by cross- and along- strike strain rate in varying proportions:

$$\begin{aligned} e_1' &= \sin\left(\frac{\pi\alpha}{2}\right) \\ e_2' &= \cos\left(\frac{\pi\alpha}{2}\right) \\ -e_3' &= e_1' + e_2' \qquad\qquad (4.20) \\ e_i' &= 0, \; i = 4, 5, 6 \end{aligned}$$

Compression of the descending slab lithosphere along the x_3 axis is balanced by flow in the x_1 and x_2 directions.

Writing **e'** for this model in its tensor form elucidates the physical significance of α, the factor which denotes the proportion of strain rate paralle to x_1 versus x_2.

$$\mathbf{E}' \propto \sin\left(\frac{\pi\alpha}{2}\right)\begin{bmatrix}1 & 0 & 0\\ 0 & 0 & 0\\ 0 & 0 & -1\end{bmatrix} + \cos\left(\frac{\pi\alpha}{2}\right)\begin{bmatrix}0 & 0 & 0\\ 0 & 1 & 0\\ 0 & 0 & -1\end{bmatrix} \tag{4.21}$$

e' is the sum of two double couples. If $\alpha = 0$, all the divergent strain rate goes into thickening the slab along x_2 (Figure 4.8a), but if $\alpha = 1$, compression is balanced by strain-rate parallel to x_1 (Figure 4.8b). $\alpha = 1/2$ indicates a purely CLVD strain rate tensor with equal components in the along-arc and cross-strike directions.

We compute **e'** for a variety of α values, allowing the geographical orientation of the x_i axes to vary (Figure 4.9). Given the same x_i coordinates, **e'** for $\alpha = 0$ (Figure 4.9b) and $\alpha = 1$ (Figure 4.9d) have the same $\hat{\mathbf{P}}$ axis, but the positions of their $\hat{\mathbf{N}}$ and $\hat{\mathbf{T}}$ are reversed. As α decreases from 1/2 to 0 (Figures 4.9e, 4.9f and 4.9b) $\hat{\lambda}$ moves from a position at $\hat{\mathbf{l}}$ to one at $\hat{\mathbf{d}}$. In practice we find that the best fits are obtained when x_2 lies within 5° – 10° of $\hat{\mathbf{P}}$, which means that for $\alpha = 0$ (Figure 4.9, lefthand column), x_1 and x_2 are aligned with $\hat{\mathbf{N}}$ and $\hat{\mathbf{T}}$, respectively. In northern and central Tonga x_1 may remain horizontal, since $\hat{\mathbf{N}}$ in these regions is sub-horizontal. In southern Tonga, however, the data require that x_1 plunges at roughly 20°. (Figure 4.9c shows the best-fitting **e'** for bin S1.)

We evaluate the fit that **e'** provides to **e** with the quantity k^2 where

$$k^2 = (\hat{\mathbf{e}} - \hat{\mathbf{e}}')^T \; V_{\hat{\mathbf{e}}}^{-1} \; (\hat{\mathbf{e}} - \hat{\mathbf{e}}') \tag{4.22}$$

[*Jordan and Sverdrup*, 1981]. If $k^2 \leq \kappa_\alpha^2$, κ_α^2 being the critical chi-squared value for 95% probability and appropriate number of degrees of freedom, then the hypothesis that $e' = e$ cannot be rejected at the 95% confidence level. If $\hat{\mathbf{N}}$ is constrained to be horizontal (northern and central Tonga) the problem contains two degrees of freedom. $\tilde{\mathbf{V}}_{\hat{e}}$ has four non-zero eigenvalues due to the deviatoric constraint on the Harvard CMT solutions and the effects of the projection operator $\mathbf{Q}$. If, however, the plunge of $\hat{\mathbf{N}}$ is allowed to vary, then only one degree of freedom exists (southern Tonga).

The range of acceptable α values each of the six slab volumes is delineated by the boxes in Figure 4.10. We find, as in the qualitative examination of Figure 4.5, that the proportion of along-arc strain rate increases south to north in the deep Tonga slab. α decreases from values between 0.37 – 0.83 in bins N1 and N2 to a range of 0.10 – 0.52 in central Tonga. It reaches a minimum of 0.00 – 0.11 in southern Tonga where the observed strain rate vectors are nearly pure double couples.

The scalar value of seismic strain rate

The above parameterization quantitatively maps the geometry of seismic strain rate in the deep Tonga slab. In order to fully describe instantaneous strain, however, we also must estimate the scalar value of strain rate. In particular, if the scalar value is constant throughout the deep subduction zone, e_3 (equal to $\partial v_3 / \partial x_3$) is also. That is, the rate of slab compression is constant at a given depth. Taking the scalar value of each side of equation 4.1 demonstrates that scalar strain rate scales linearly to the rate of seismic moment release. The latter may be obtained by summing observed earthquake moment over the entire volume of the deep Tonga slab and dividing this value by the time interval in which the earthquakes occured.

We approximate total seismic moment with a procedure similar to that of *Richter* [1979], always bearing in mind whether our method biases us to a maximum or minimum value. For every event in the 1964–1984 International Seismological Center (ISC) catalog between 500 and 700 km depth with $5.0 \leq m_b \leq 6.0$, we calculate its seismic moment assuming a linear relation between m_b and the logarithm of M_o [*Gutenberg and Richter,* 1955, 1956; *Hanks and Kanamori,* 1979]. We then sum the moments over this magnitude range, scale the total to an upper moment cutoff of 2.0×10^{22} N m (2.0×10^{29} dyn cm, corresponding to $m_b = 8$) assuming a b value of unity, and divide by the time interval to get an average rate of seismic moment release, $\dot{M}_{seismic}$ ($\dot{M} = \partial M_o / \partial t$).

For all deep-focus earthquakes in the Tonga arc this summation yields $\dot{M}_{seismic} = 2.7 \times 10^{20}$ N m/yr, a value consistent with *Richter's* [1979] estimate. This rate, however, is likely an overestimate for two reasons. First, it is sensitive to the upper moment cutoff and the largest deep focus earthquake documented by *Abe and Kanamori* [1979] has an estimated moment of 2.2×10^{21} N m, about an order of magnitude less than our assumed cutoff value. Unless the largest deep-focus events are significantly undersampled in the 70-year interval considered by *Abe and Kanamori* [1979], the above value of $\dot{M}_{seismic}$ is significantly too large. Second, in a recent paper *Giardini* [1988] suggests a b value for deep earthquakes in the Tonga subduction zone which is significantly greater than unity. Substituted into the above calculation, this b value yields a smaller $\dot{M}_{seismic}$. *Ekstrom and Dziewonski* [1988] point out that M_o values obtained by scaling m_b from catalogs such as the ISC may be too large or too small by as much as a factor of four. As a source of bias, however, this effect is relatively insignificant when compared with the order of magnitude over-estimation outlined above.

Calculating $\dot{M}_{seismic}$ as a function of latitude reveals that the scalar value of seismic strain rate is roughly constant as a function of latitude. For bins N1 and N2, $\dot{M}_{seismic} = 7.2 \times 10^{19}$ N m/yr, and for C1– C2 and S1– S2 its values are 8.7×10^{19} N m/yr and 1.0×10^{20} N m/yr, respectively. Since this result requires that the rate of slab compression (e_3) is constant at a given depth, the increase in α from south to north in the deep slab indicates that the absolute size of the along-arc strain rate component also grows to the north, while the cross-strike component decreases.

FINITE DEFORMATION OF THE DEEP SLAB

Clearly the description of strain rate yielded by the moment tensor data provides only a snapshot of deformation in the deep Tonga slab, while large-scale structural features, such as substantial advective thickening or 300 – 500 km of along-arc shear, develop over millions of years. If we are willing to assume that strain rate in the Tonga lithosphere is steady-state, however, we can postulate a variety of flow models which relate the strain rate data to estimates of finite strain. The steady-state asuumption is difficult to verify completely, but models of surface plate motions are consistent with a constant rate of compression over the last 20 my [*Minster and Jordan,* 1978; *Minster et al.,* 1974; *Molnar et al.,* 1975; *Billington,* 1980]. Since the moment tensor data only sample seismic strain rate, we must also make an assumption regarding aseismic flow. For the sake of simplicity we define the geometry of aseismic strain rate to be identical to the seismic estimate.

Along-arc versus cross-strike strain

First we consider simplified flow models in which equation 4.20 describes strain rate and α is constant throughout the deep slab. A set of possible particle paths for such a flow geometry are shown in Figure 4.11. Down-dip velocity, v_3, is continuous at the top and bottom boundaries of the depth range, ζ, and its initial value is equal to the rate of subduction. Discontinuities in the other velocity components and $\partial v_i / \partial x_i$ are allowed, but we assume they occur over small depth ranges and are not reflected in the strain rate data. A possible physical justification for discontinuous flow at the upper boundary is the phase change at 450 km which may substantially weaken the lithosphere at that depth.

Since our analysis of the moment tensor data does not constrain the rotational, or asymmetric, part of the flow, we must assume whether strain along a particular axis thickens or shears the slab. In the two-dimensional view of Figure 4.11a deformation perpendicular to slab strike occurs as advective thickening. Δx_2 is undeformed slab thickness and γ

describes the ratio of undeformed to deformed slab thickness. Possible particle paths for along-arc flow indicate southward or northward shear of the deep slab (Figures 4.11b and 4.11c, respectively). β parameterizes the relative displacement of particles at different locations along the arc. The fault plane identifications [*Giardini and Woodhouse,* 1986], the apparent shallowing of maximum slab and seismicity in northernmost Tonga (Figure 4.1), and the hypothesized signature of the subducted Louisville Ridge [*Giardini and Woodhouse,* 1986], argue for southward displacement of the deep lithosphere. If these data are discounted, however, both models are equally plausible.

The seismic strain rate vectors coupled with estimates of scalar strain rate indicate that the rate of slab compression, e_3, does not vary with latitude, but that e_1 decreases north to south while e_2 increases. This variation in e_2 , $\partial v_2 / \partial x_2$, produces larger γ factors as a function of latitude. The effect of a southerly decrease in e_1, or $\partial v_1 / \partial x_1$, is more subtle and is indicated by the dashed particle paths in Figure 4.11b. While the magnitude of v_1 increases to the south, as is the case with constant α, the curvature of the particle trajectories diminishes. If $\partial v_1 / \partial x_1 = 0$, then the particle paths are straight lines. (The slab element originating at point C follows such a trajectory over ζ). A three-dimensional view of the particle paths caused by the $e_2 - e_1$ trade-off is shown in Figure 4.12, assuming southward shear of the deeper lithosphere. γ grows to the south as the along-arc curvature of the particle trajectories decreases. The dashed lines outline what slab morphology would be if no thickening was ocurring.

Figure 4.12 also conveys the tectonic reconstruction on which the estimates of along-arc finite strain are based. The northern edge of the Tonga slab (Figure 4.1) appears to have a shape something like the particle path originating at Point A, Figure 4.12, and the material now at roughly 700 km and 17° S may have entered the trench at 14.5° S. The azimuth of the unsubducted Louisville Ridge suggests that the Louisville Ridge seismic gap (700 km and 22.5° S) originated at 18° S (Point B, Figure 4.12). If these values are accurate, β, averaged over northern and central Tonga, is on the order of 1.5.

Constraints on γ?

Given the estimates of β and α, we should be able to obtain a rough lower bound on the cross-strike thickening factor in northern and central Tonga. *McKenzie and Jackson* [1983] show that the relationship of an instantaneous Eulerian flow field to finite strain may be obtained by solving:

$$\frac{\mathbf{DF}}{\mathbf{Dt}} = \left(\frac{\partial}{\partial t} + \mathbf{v}\cdot\nabla\right)\mathbf{F} = \mathbf{LF} \tag{4.23}$$

where **F** is the deformation gradient tensor which describes the deformation of any vector which joins two particles in the fluid, over a time interval t. Simple solutions to 4.23 exist only if the advective terms vanish [*McKenzie and Jackson,* 1983], that is, if the elements of **L** are constant throughout the deforming region. Given the variations in α with latitude, a numerical solution to equation 4.23 is required to model the Tonga data accurately.

Given the uncertainty in the β estimate, however, such precision is hardly warranted. We approximate α in northern and central Tonga with a constant value of 1/2, which, according to equation 4.23, yields a γ value on the order of 1.5, that is, thickening of the slab by 50%. Due to the possibility of aseismic deformation, this value is a lower bound on the amount of thickening. If accurate, it improves upon the resolution of slab width provided by travel time observations since the latter are consistent with lithospheric models which enter the lower mantle without deforming.

In order to examine the amount, if any, of aseismic deformation that the strain rate data require, we calculate the scalar rate of seismic moment release implied by an α of 1, and a γ and β of 1.5, $\dot{M}_{flow}$, by integrating **e'** over the deforming slab volume. This volume is defined by the depth range, ζ, and by the particle paths corresponding to particular values of arclength and Δx_2, undeformed slab width. Δx_2 = 25 km corresponds to a lower bound on the width of deep seismicity, and $\Delta x_2 = 100$ km represents total undeformed slab thickness. $\dot{M}_{flow}$ values for $\Delta x_2 = 25$ km therefore reflect strain rate in the portion of the deep slab cold enough to be seismically deformable, and $\dot{M}_{flow}$ for $\Delta x_2 = 100$ km includes the warmer, aseismic outer regions of the lithosphere. In bins N1, N2, C1 and C2 (17° S – 22° S) $\dot{M}_{seismic}$, the observed rate of moment release, is just large enough to account for $\dot{M}_{flow}$ in the seismogenic core of the slab ($\Delta x_2 = 25$ km). Any deformation in the warmer, more ductile outer regions of the slab must be aseismic, particularly since $\dot{M}_{seismic}$ may overestimate the actual rate of moment release.

CONCLUSIONS

Observed strain rate vectors in the deep Tonga slab are consistent with slab deformation models in which the lithosphere encounters resistance to penetration at the 650-km discontinuity. Compression of the slab is balanced by strain rate components in both the cross-strike and along-arc directions. Strain rate vectors which sample lithospheric volumes from 18° S to 25° S indicate that the axis of maximum shortening lies within 20° of the down-dip azimuth and plunge of the Tonga slab. Compression oblique to the slab trajectory does occur, particularly in the western trending band of events between 17° S and 18° S which may mark the intersection of the subducting Tonga lithosphere with a remnant slab fragment. The proportion of along-arc strain rate decreases from northern Tonga to southern Tonga. Since estimates of the scalar rate of seismic strain are constant with latitude, the rate of slab compression is also. Therefore, the magnitude of along-arc strain rate also decreases to the south while cross-strike strain rate increases.

Strain rate data may be related, non-uniquely, to estimates of finite strain based on seismicity and travel time data, and they require that the degree of cross-strike advective thickening increases to the south. Offsets in both the distribution of deep-focus hypocenters and the northern terminus of lithospheric structure suggest that along-arc strain occurs as southward displacement of the deeper lithosphere relative to shallow structure. Assuming that aseismic and seismic flow have the same geometry and that along-arc strain rate exclusively produces southward shear, corss-strike thickening of at least 50% thickening may be required in central Tonga. Due to the possibility of aseismic deformation, this value is a lower bound on total thickening, but it improves upon the resolution of slab width provided by travel time observations. The latter are consistent with lithospheric models which enter the lower mantle without deforming. The estimated rate of seismic moment release is large enough to account for the scalar strain rate implied by 50% thickening in the seismogenic core of the slab. More substantial deformation must be aseismic.

TABLE 1. PARAMETER VALUES FOR OBSERVED AND THEORETICAL STRAIN VECTORS

Slab volume	Label	Slab strike,dip	$\hat{\mathbf{P}}$ azimuth,plunge
17°S – 18° S	N1	15°, *	248°, 32°
18°S – 19° S	N2	15°, *	272°, 47°
20°S – 21° S	C1	15°, 64°	306°, 54°
21°S – 22° S	C2	15°, 64°	304°, 50°
22°S – 23° S	S1	30°, 55°	285°, 52°
24°S – 25° S	S2	35°, 50°	316°, 40°

*Slab dip unconstrained; see text for discussion.

Figure 4.1. Three-dimensional view of Tonga subduction zone seismicity viewed from an azimuth perpendicular to strike. Events below 300 km and south of 16° S are relocated hypocenters [*Giardini and Woodhouse,* 1984] and other data are from the ISC catalog (1964 – 1984) for depths greater than 10 km. All earthquakes have $m_b \geq 5.2$. Line segments at left indicate the northern termination of the best-fitting slab models determined from travel time data, and arrow points to subducted Louisville Ridge seismicity gap at a depth of 650 km. The five events to the left of the northern termination of the slab are associated with the Vityaz slab.

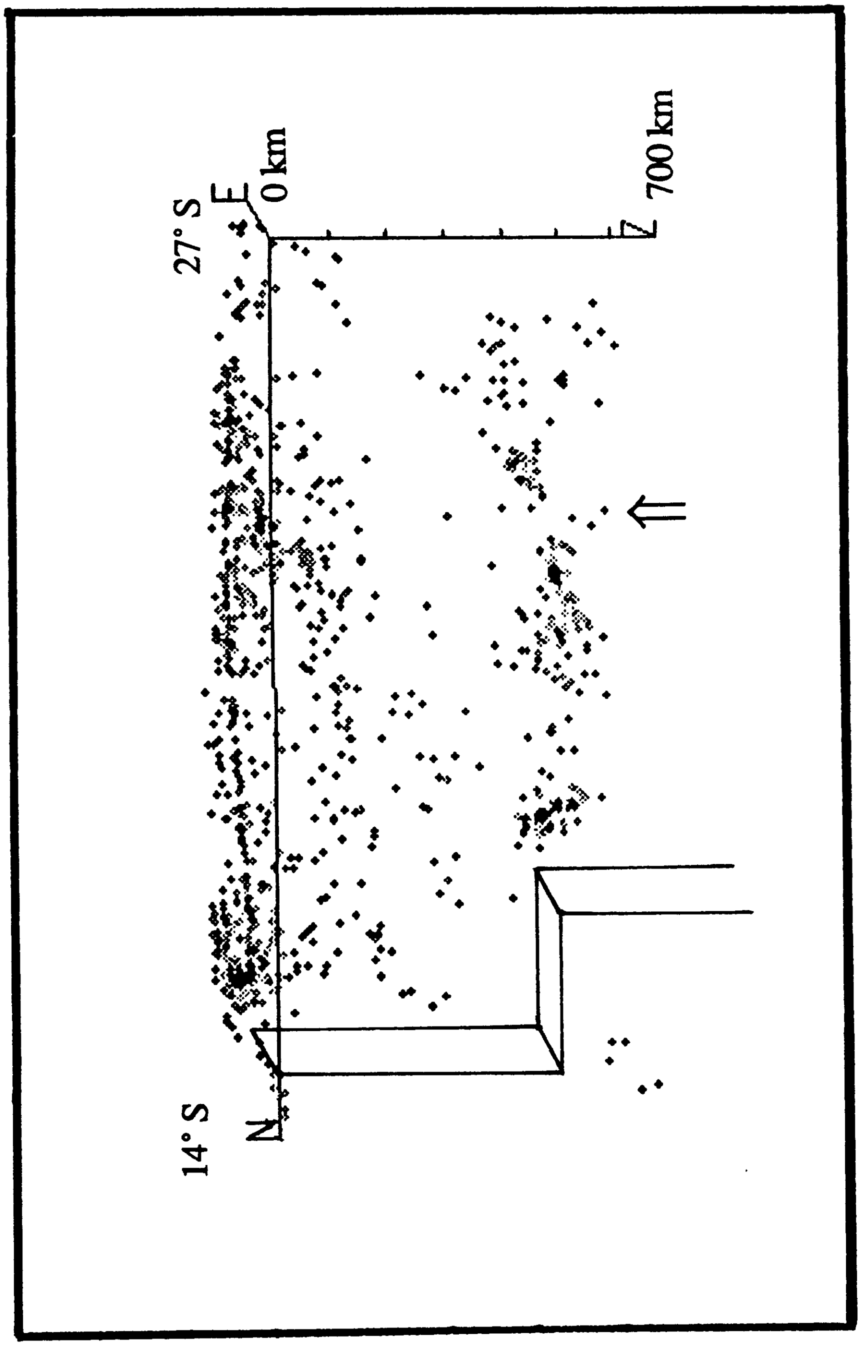

Figure 4.1

Figure 4.2. Compression and extension axes for CMT solutions from the Harvard catalog, 1977–1986 for the Tonga arc between 500 km and 700 km depth (*Dziewonski and Woodhouse,* 1983; *Dziewonski et al.,* 1983abc, 1984abc, 1985abcd, 1986abc, 1987abcdefg, 1988abcd; *Giardini,* 1984). Views are from an azimuth perpendicular (above) and parallel (below) to slab strike. The along-arc view contains all solutions reported for the Tonga subduction zone; the cross-strike view contains data from 17°S – 18° S only. The orientations of the axes maximum shortening extension for the individual Harvard CMT solutions in the deep Tonga slab yield a qualitative sense of the seismic strain throughout the subduction zone.

Figure 4.2

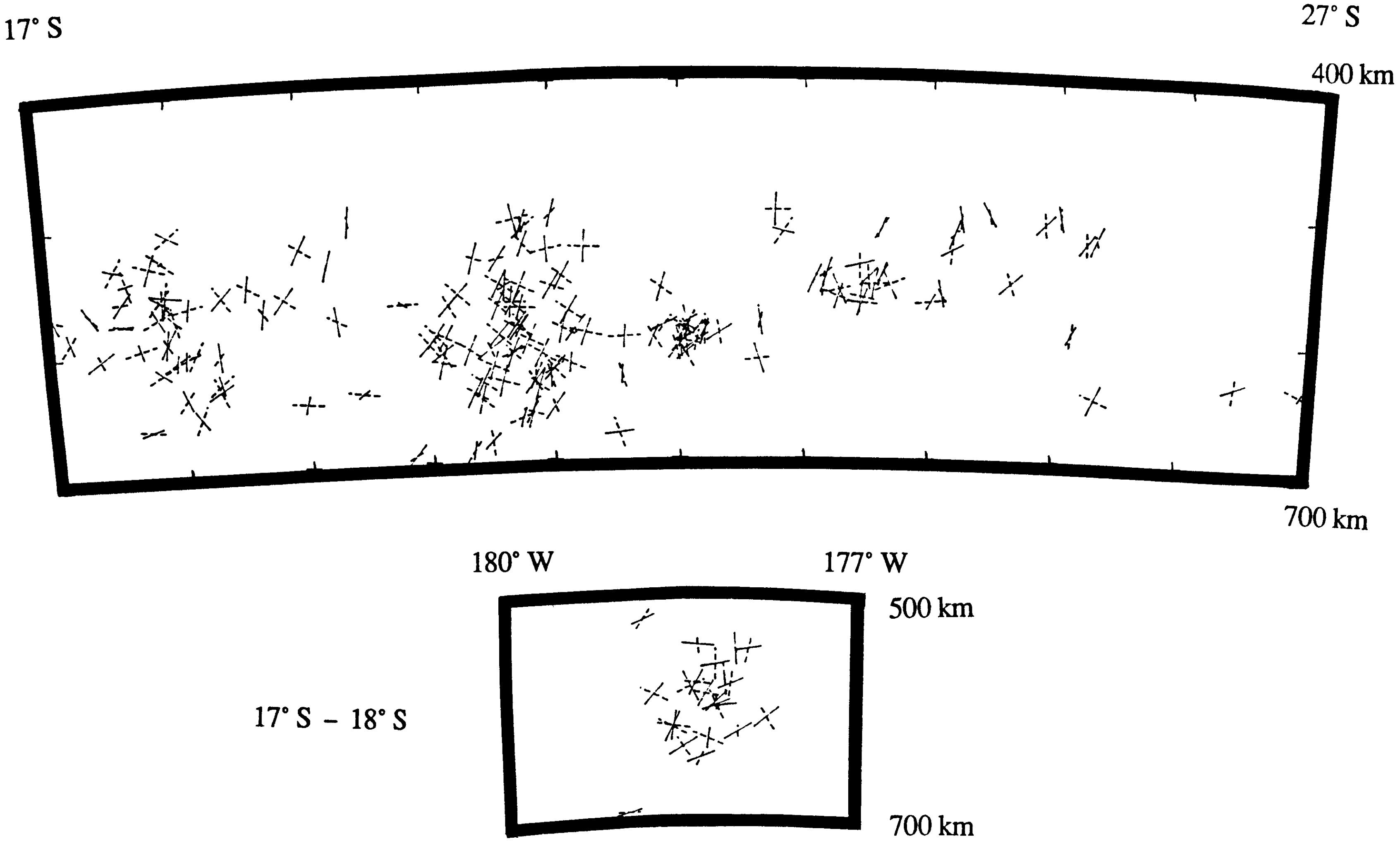

Figure 4.3. Number of CMT solutions in the Harvard catalog for earthquakes below 500 km in the Tonga arc as a function of M_o.

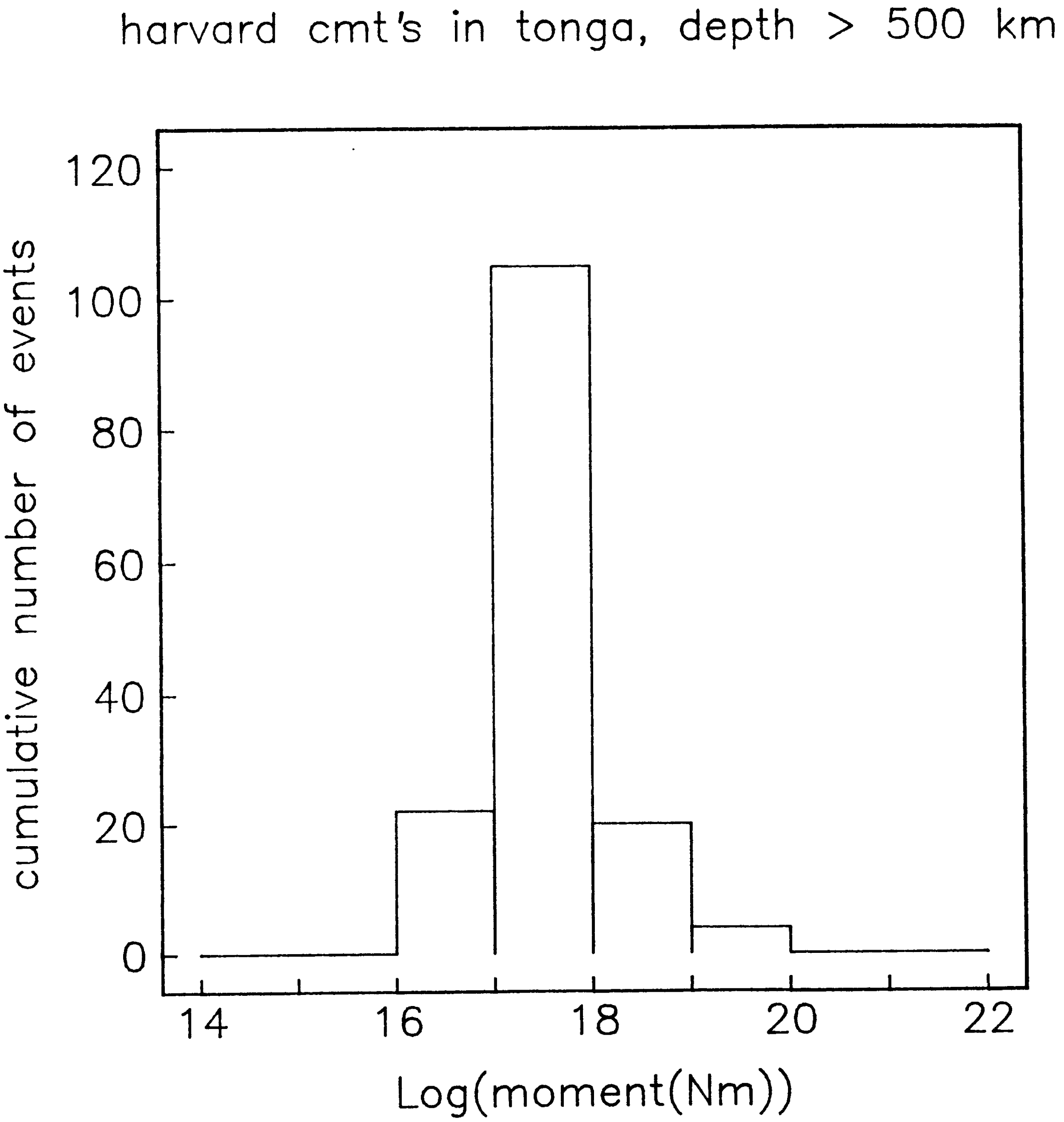
harvard cmt's in tonga, depth > 500 km
cumulative number of events
0
20
40
60
80
100
120
14
16
18
20
22
Log(moment(Nm))

Figure 4.3

Figure 4.4. Illustration of the projection operator $\mathbf{Q}$. Since the distribution of $\hat{\mathbf{m}}_k$ is not Gaussian, we make the assumption that we can retain the Gaussian description of variance if we project the difference vectors $\hat{\mathbf{m}}_k - \tilde{\mathbf{m}}_0$ onto the tangent plane perpendicular to $\tilde{\mathbf{m}}_0$ with the operator $\mathbf{Q}$. If the distribution of $\hat{\mathbf{m}}$ is Gaussian, $\hat{\mathbf{m}}_k - \tilde{\mathbf{m}}_0$ by definition lies in the tangent plane perpendicular to $\tilde{\mathbf{m}}_0$.

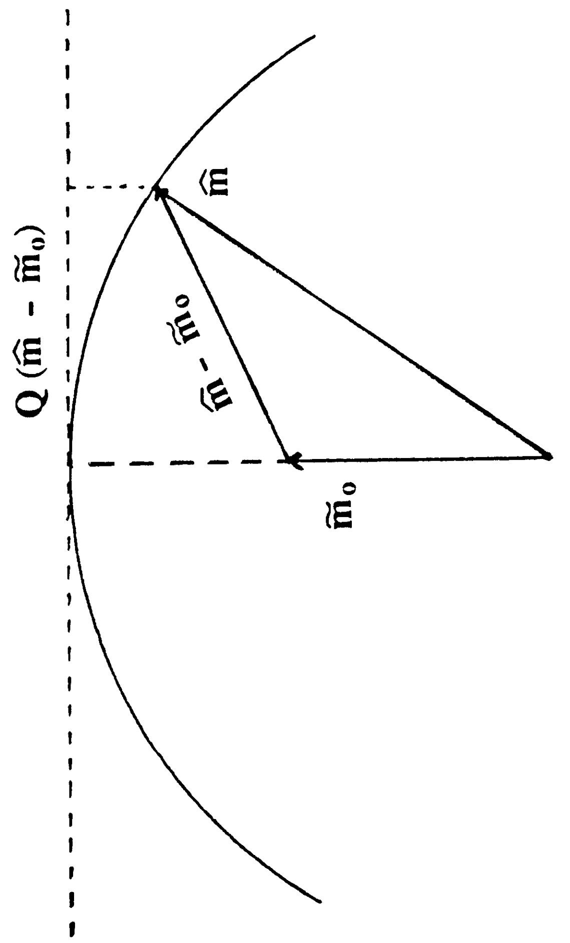

Figure 4.4

Figure 4.5. Observed strain rate vectors, **e**, for the six volume bins in the deep Tonga slab surrounding a map of Tonga subduction zone seismicity (hypocenters are identical to those in Figure 4.1). Boxes in map delineate the geographical range of the six slab volumes, which north to south are N1, N2, C1, C2, S1 and S2. Squares indicate the hypocenters of the 25 deep- and intermediate-focus earthquakes modeled in chapter 3. The strain rate vector projection is onto the lower focal hemisphere, and the value underneath each plot indicates the number of summed CMT solutions. $\hat{\boldsymbol{\lambda}}$ is the source mechanism vector which describes the eigenvalues and eigenvectors of **e** and characterizes the type of source mechanism **e** implies. If the source mechanism is largely double-couple, then $\hat{\boldsymbol{\lambda}}$ lies close to $\hat{\mathbf{d}}$, and if it is a compensated linear vector dipole, $\hat{\boldsymbol{\lambda}}$ approximates $\hat{\mathbf{l}}$. $\hat{\mathbf{P}}$, $\hat{\mathbf{T}}$ and $\hat{\mathbf{N}}$ show the directions of maximum shortening and extension, and the null axis, respectively. The dashed great circle represents the vector-space of all deviatoric mechanisms. Marginal error ellipses for $\hat{\mathbf{P}}$, $\hat{\mathbf{T}}$ and $\hat{\mathbf{N}}$ and $\hat{\boldsymbol{\lambda}}$ [*Riedesel and Jordan,* 1988] are constructed from the normalized variance matrix for the complete strain rate vector, and correspond to the 95% confidence level.

Figure 4.5

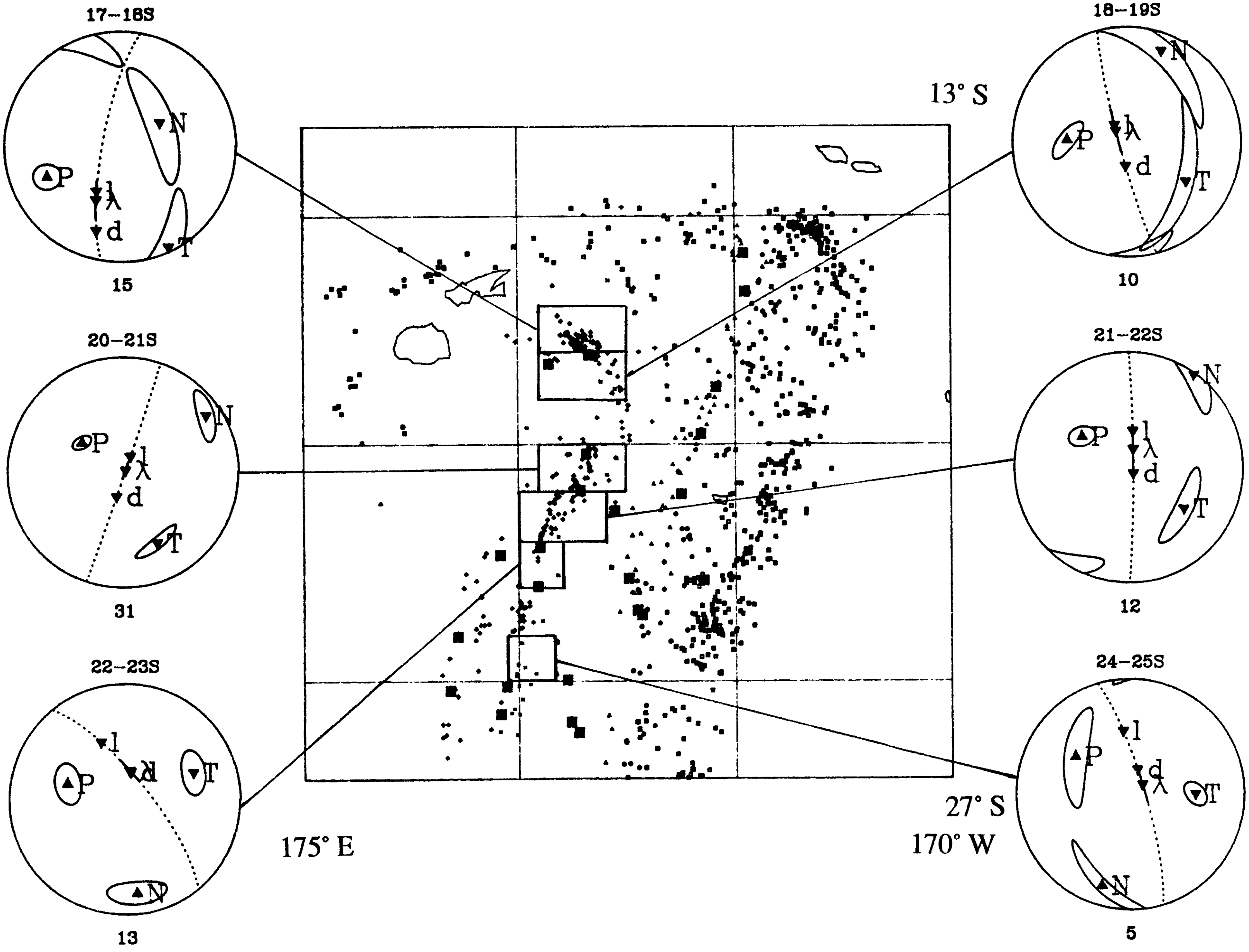

17–18S
P
N
l
λ
d
T
15
20–21S
P
l
λ
d
N
T
31
22–23S
l
P
λ
d
T
N
13
13° S
27° S
175° E
170° W
18–19S
N
l
λ
P
d
T
10
21–22S
N
P
l
λ
d
T
12
24–25S
l
P
d
λ
T
N
5

Figure 4.6. Source mechanism plots similar to Figure 4.5 showing **e** as a function of M_o in the slab volume C1 between 20°S – 21°S. **e** is computed for three moment ranges: 1×10^{16}N m $\leq M_o \leq 1 \times 10^{17}$N m, 1×10^{17}N m $\leq M_o \leq 1 \times 10^{18}$N m and 1×10^{18}N m $\leq M_o \leq 1 \times 10^{19}$N m. **e** for 1×10^{17}N m $\leq M_o \leq 1 \times 10^{18}$N m is the standard strain rate vector also shown in Figure 4.5. The similarity between these different estimates of strain rate indicates that e is quite independent of the size of the earthquakes from which it is calculated.

Figure 4.6

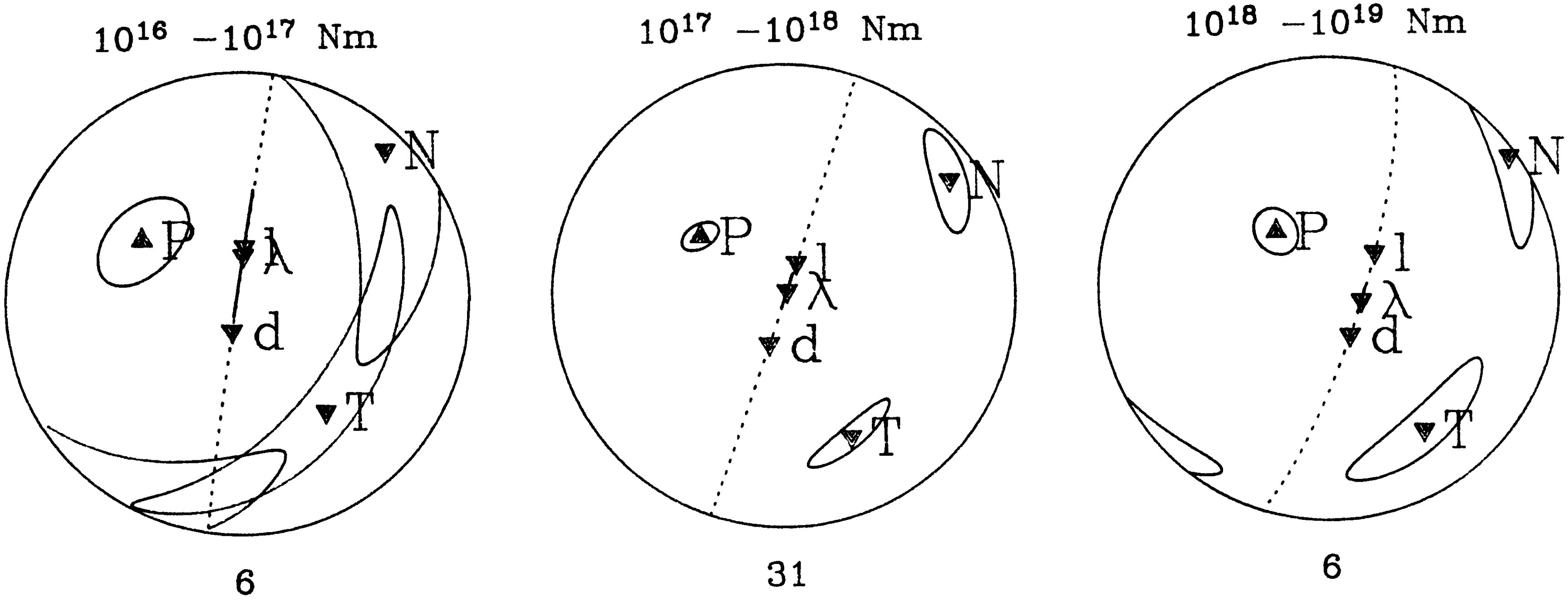
10^{16} -10^{17} Nm

6

10^{17} -10^{18} Nm

31

10^{18} -10^{19} Nm

6

Figure 4.7. Source mechanism plots similar to Figure 4.5 comparing strain rate vectors for the eastern *(right)* and western *(left)* bands of the imbricated southern Tonga seismic zone from 22° S to 26° S. While in the eastern band the deep slab is on average compressing parallel to its trajectory, in the western band $\widehat{\mathbf{P}}$ dips to the east back under the subducting lithosphere. The individual compression axes for 21 out of 22 events in the eastern band dip to the east, but in the western band, only 2 out of 6 do. Individual source mechanisms in the western branch of the double zone are excluded from bins S1 and S2.

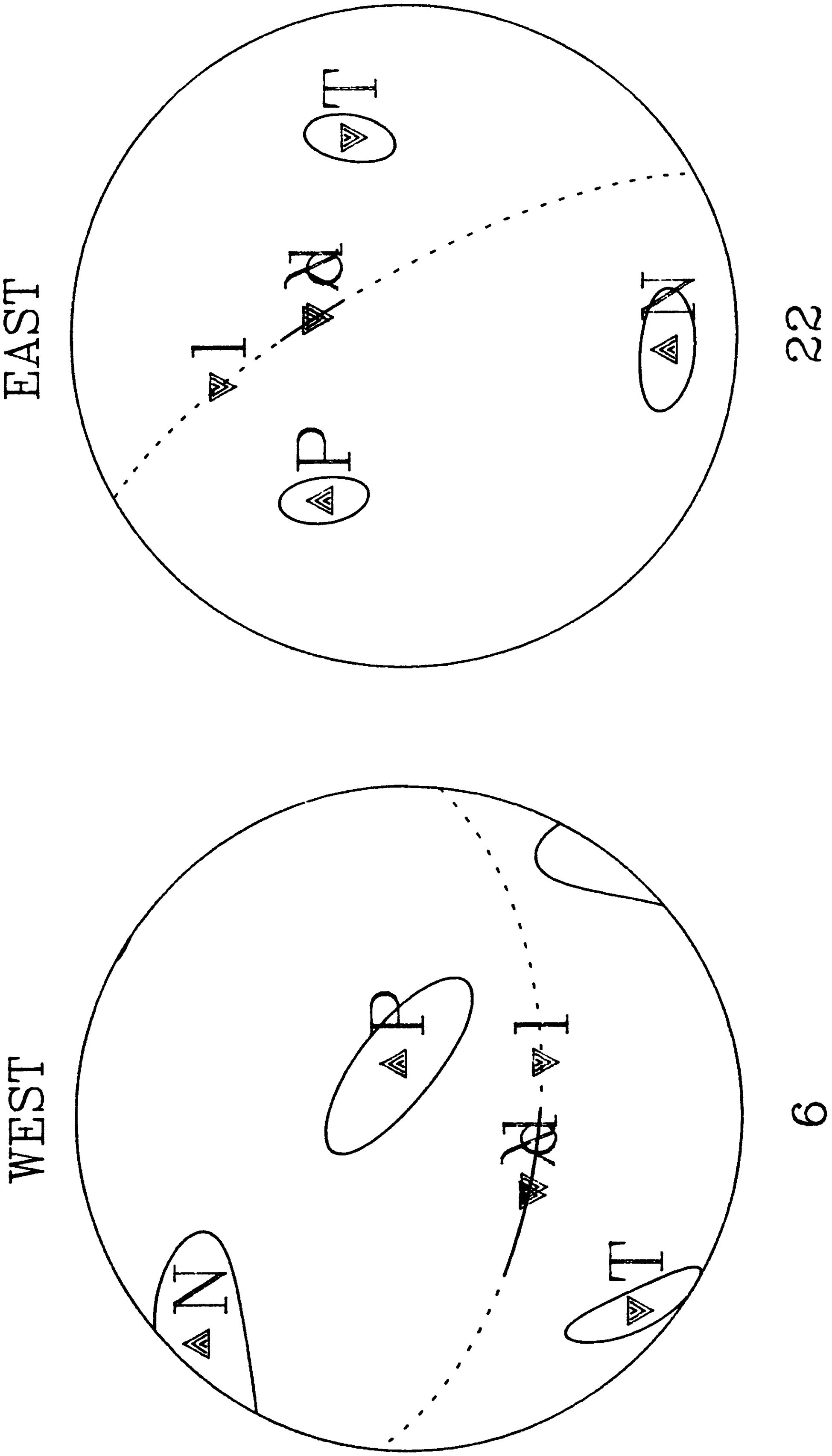

Figure 4.7

Figure 4.8. *a)* Schematic view of the source mechanism corresponding to $\alpha = 0$. The direction of maximum compression is parallel to x_3 and maximum extension is aligned with x_2. Slip is assumed to occur on both conjugate fault planes. *b)* Schematic view of the source mechanism corresponding to $\alpha = 1$. The direction of maximum compression is parallel to x_3 and maximum extension is aligned with x_1. Given finite strain estimates in northern and central Tonga, slip is assumed to occur on only one fault plane, resulting in southward shear of the deeper lithosphere.

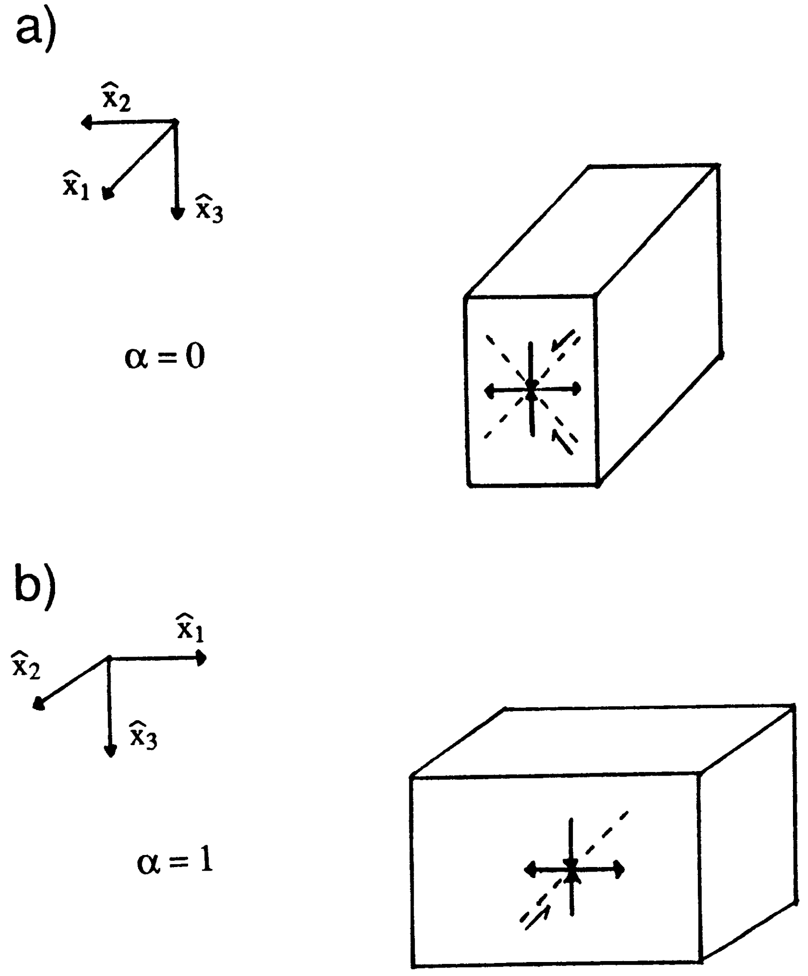

Figure 4.8

Figure 4.9. Source mechanism plots similar to Figure 4.5 for theoretical strain rate vectors corresponding to a variety of α values and x_i orientations. *a)* $\alpha = \infty$ with $\widehat{\mathbf{P}}$ vertical, but $\widehat{\mathbf{N}}$ horizontal and south and $\widehat{\mathbf{T}}$ horizontal and east *b)* $\alpha = \infty$ with $\widehat{\mathbf{P}}$ rotated to a plunge of 50° and an azimuth of 345° *c)* $\alpha = \infty$ with $\widehat{\mathbf{N}}$ rotated about a easterly axis to a plunge of 20° and $\widehat{\mathbf{P}}$ rotated to a plunge of 50° and an azimuth of 345° (the best-fitting **e'** for bin S1) *d,e,f)* same x_i rotations as in *b)* but for $\alpha = 0$, 1 and 3, respectively.

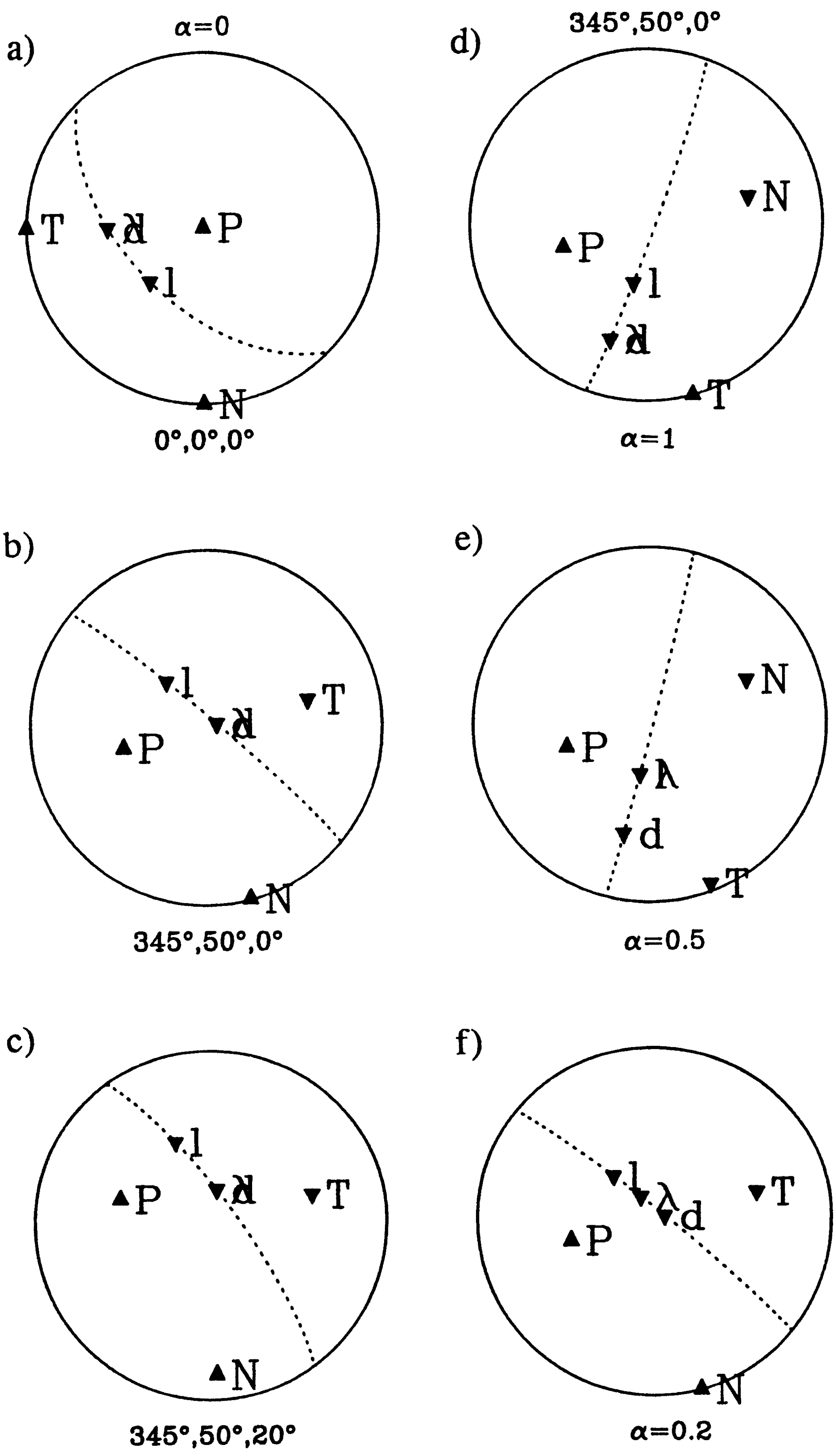
a)
α=0
T
λ
d
P
l
N
0°,0°,0°
d)
345°,50°,0°
N
P
l
λ
d
T
α=1
b)
l
λ
d
T
P
N
345°,50°,0°
e)
N
P
λ
d
T
α=0.5
c)
l
P
λ
d
T
N
345°,50°,20°
f)
l
λ
d
T
P
N
α=0.2

Figure 4.9

Figure 4.10. The range of acceptable α values for each of the six slab volumes (delineated by boxes), plotted as a function of their latitude.

Figure 4.10

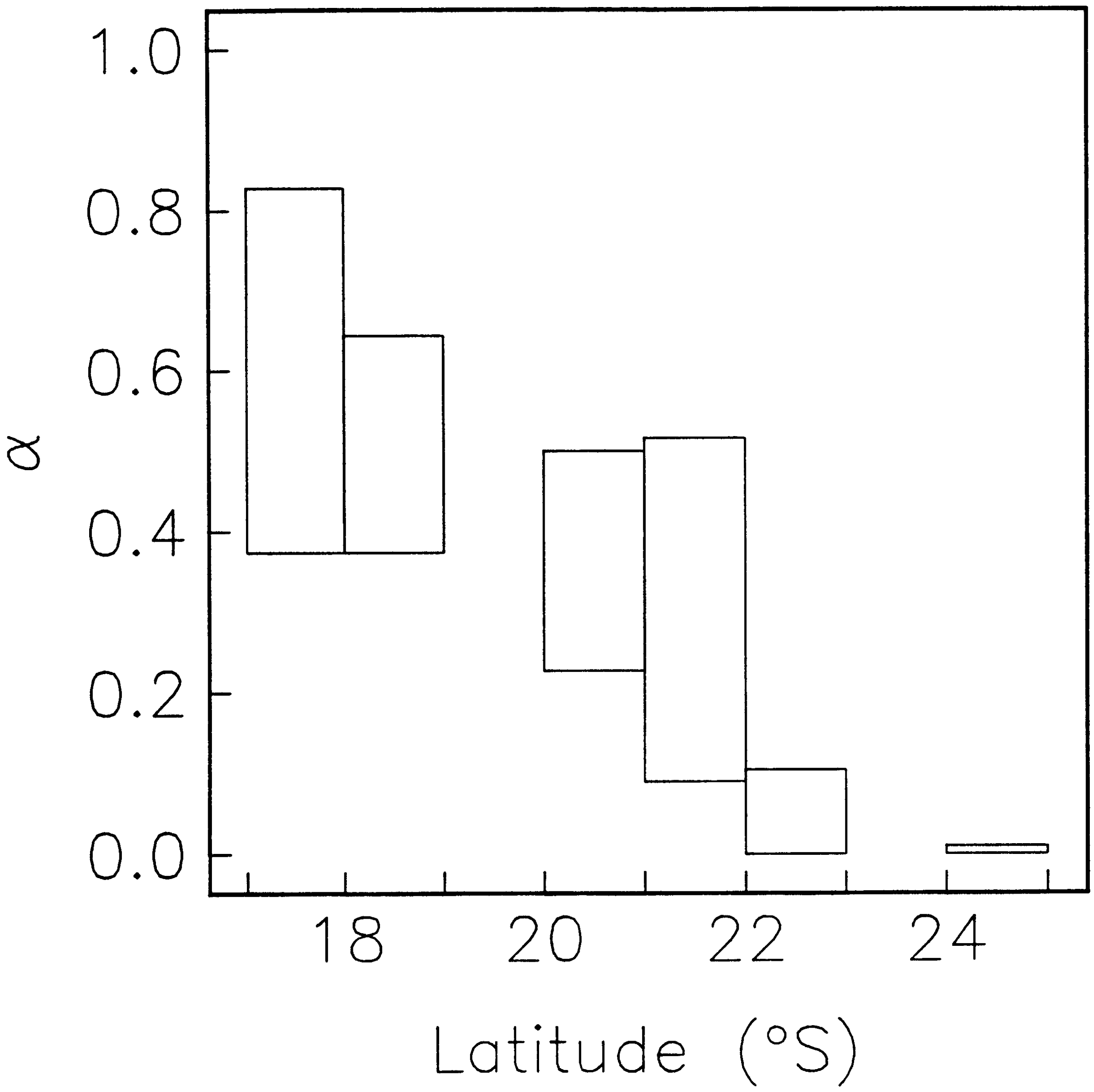

Figure 4.11. Two-dimensional views of particle paths consistent with the strain rate model in equation 4.20. Down-dip velocity, v_3, is continuous at the top and bottom boundaries of the depth range, ζ, and its initial value is equal to the rate of subduction. Discontinuities in the other velocity components and $\partial v_i / \partial x_i$ are allowed. *a)* Deformation perpendicular to slab strike occurs as advective thickening. Δx_2 is undeformed slab thickness and γ describes the ratio of undeformed to deformed slab thickness. *b)* Along-arc flow occurs as southward shear of the deep slab. β parameterizes the relative displacement of particles at different locations along the arc. Solid lines indicate particle paths for constant α; dashed lines correspond to an α which decreases southward, causing the curvature of the particle trajectories to diminish. If $\alpha = 0$, the particle paths are straight lines. (The slab element originating at point C follows such a trajectory over ζ). *c)* Along-arc flow occurs as northward shear of the deep slab.

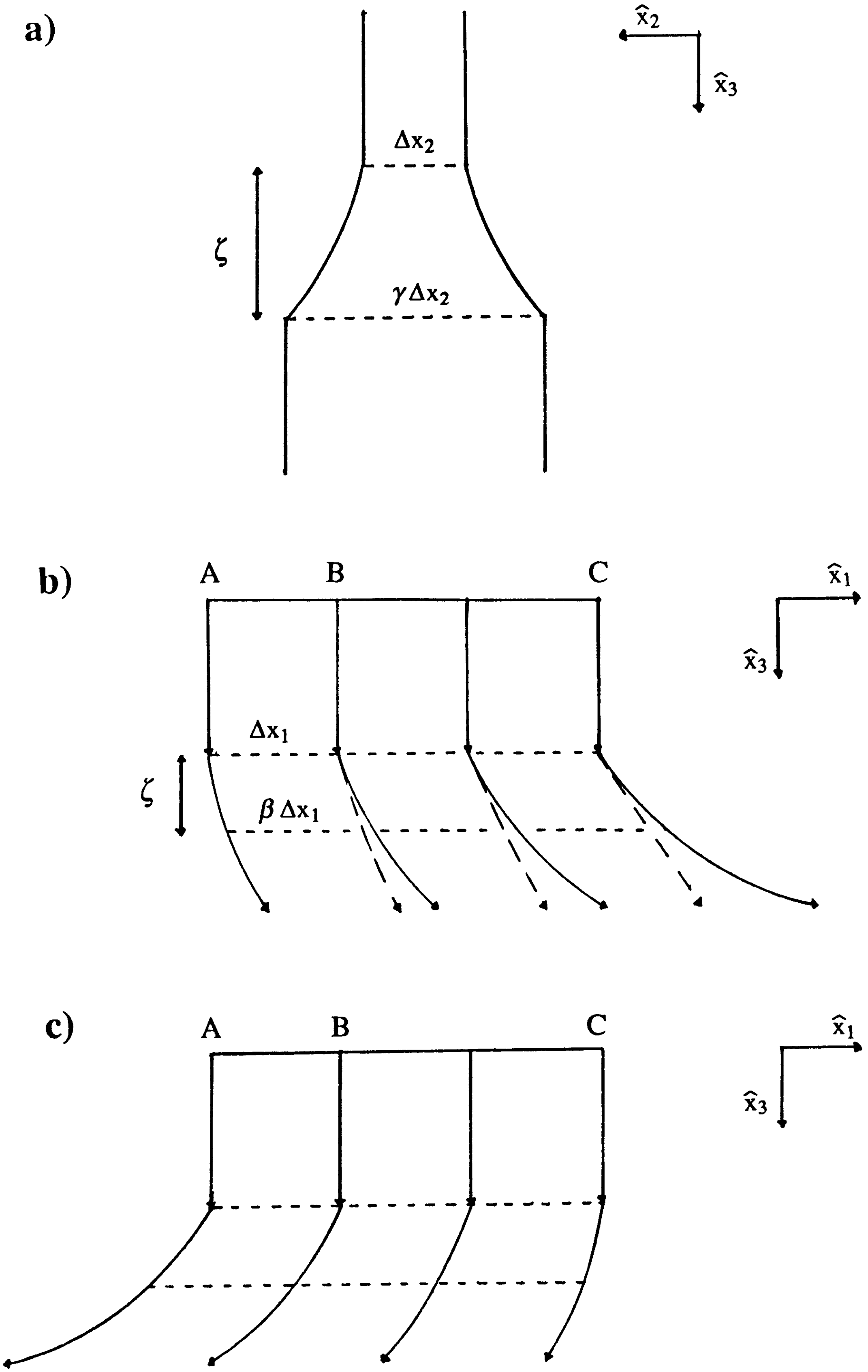
a)
$\hat{x}_2$
$\hat{x}_3$
Δx_2
ζ
$\gamma \Delta x_2$
b)
A
B
C
$\hat{x}_1$
$\hat{x}_3$
Δx_1
ζ
$\beta \Delta x_1$
c)
A
B
C
$\hat{x}_1$
$\hat{x}_3$

Figure 4.11

Figure 4.12. A three-dimensional view of the particle paths caused by a decrease in along-arc strain rate and an increase in cross-strike strain rate, north to south, assuming southward shear of the deeper lithosphere. γ grows to the south as the along-arc curvature of the particle trajectories decreases. The dashed lines outline what slab morphology would be if no thickening was ocurring. The northern edge of the Tonga slab appears to have a shape something like the particle path originating at Point A, and the material now at roughly 700 km and 17° S may have entered the trench at 14.5° S. The azimuth of the unsubducted Louisville Ridge suggests that the Louisville Ridge seismic gap (700 km and 22.5° S) originated at 18° S (Point B). If these values are accurate, β, averaged over northern and central Tonga, is on the order of 1.5.

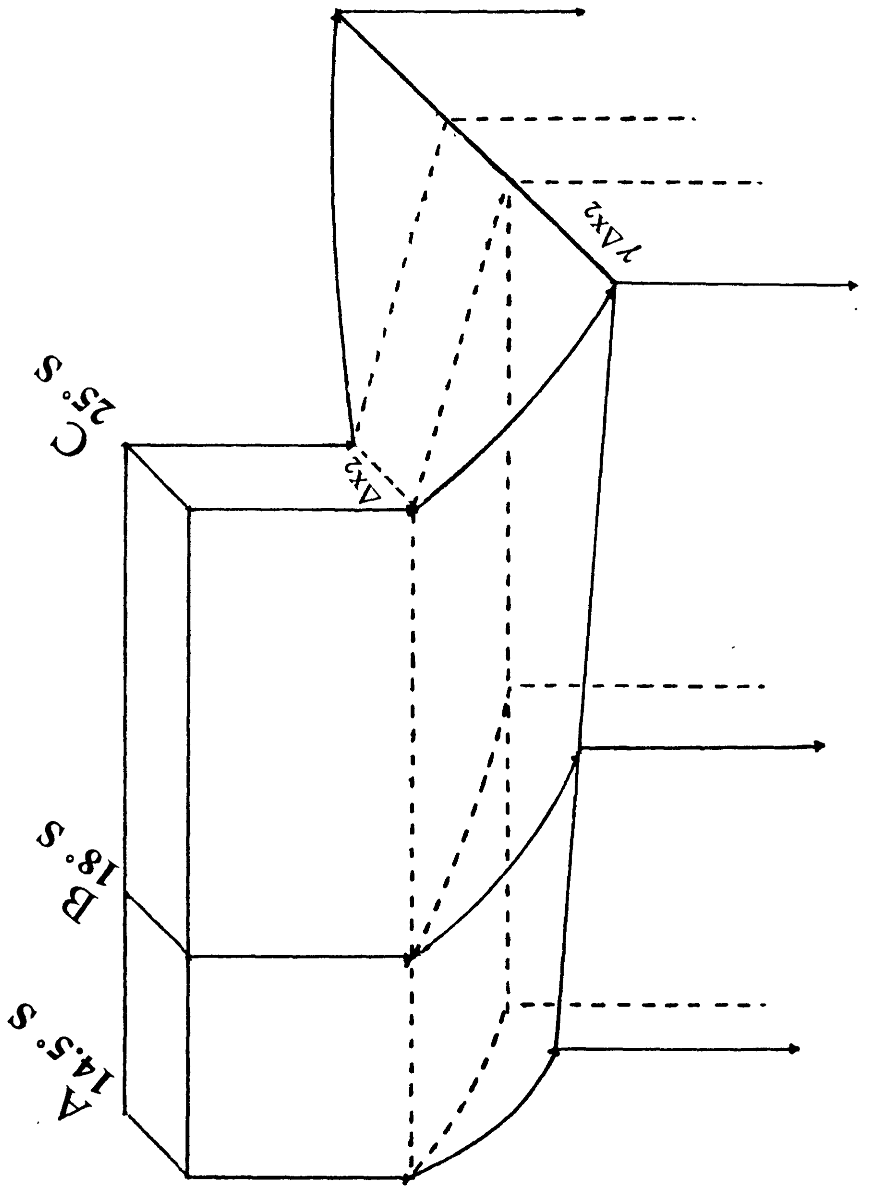

Figure 4.12

CHAPTER 5

CONCLUSIONS

While descending lithospheric slabs appear to penetrate the 650-km discontinuity, they may experience advective deformation in the vicinity of that depth. Residual sphere data from earthquakes in the Tonga, Mariana, and Kuril-Kamchatka arcs require that the descending slab extends to depths of 800 km–900 km or more, but down-dip compressional source mechanisms, and in Tonga the contorted deep seismic zone, suggest that the lithosphere encounters considerable resistance at the upper mantle-lower mantle boundary. Travel time data from all three of these arcs are consistent with lateral advection of slab material perpendicular to the arc. Tonga residuals are well fit by, and in fact may prefer, slab models which advectively thicken in the transition zone by factors of three or more, but simple thermal boundary layer models cannot be ruled out. Similarly, while more than a three-fold increase in slab width is not consistent with the Kuril-Kamchatka observations, travel time data in the Mariana arc allows advective thickening factors of 5 or more, and these residuals are also consistent with slab models that extend into the lower mantle without deforming. The insensitivity of the travel time data to slab width, relative to the tight constraints that they place on slab strike, dip, and depth extent, may be explained by the combined effects of three-dimensional ray bending and the geometrical weakness inherent in the station distributions about the Tonga and vertical Mariana slabs.

In addition to the possibility of cross-strike deformation, the structure of the lithosphere in Tonga contains considerable variation along the arc, and observed strain rate vectors in the deep Tonga slab are consistent with models in which compression of the slab parallel to its dip is balanced by not only thickening in the cross-strike direction but also along-arc shear. A combination of inferred morphology, trends in the seismicity and observed strain rate vectors, highlight certain features of slab flow and its relationship to regional tectonics. In general the hypocenter data matches the undulations in slab strike and dip mapped by travel time residuals down to small wavelength features such as the abrupt change in slab strike at 25° S, a strong argument that the residual spheres do reflect near-source heterogeneity. The data in southern Tonga require a bend to steeper dip in the deep slab, a feature also resolved in the Japan, Kuril-Kamchatka and Aleutian slabs [*Creager and Jordan,* 1986; *Boyd and Creager,* 1988], but the travel times in central and northern Tonga do not. If downward curvature of the slab profile is indeed a global feature of subduction flow [*Gurnis and Hager,* 1988] the absence of such a bend in northern and central Tonga is perhaps explained by disruption of subduction at the northern end of the arc due the Tonga lithosphere colliding with the remnant Vityaz slab fragment at depths of 450 km or more. The westward hook, the bench in dip and the oblique deep-focus band which appear in northern Tonga seismicity may also be explained by this peculiarity of regional tectonics, and the direction of maximum shortening inferred from the average strain rate vectors from this arc segment shows an anomalously shallow dip.

Other structures in the Tonga arc may be related to a component of along-strike shear in the deep slab. In northern Tonga, both the seismicity and the depth to which the slab must penetrate in order to match the travel time data shallow to the north, a feature which may be explained by southward shear of the deep lithosphere relative to shallow structure. These offsets, plus identification of fault planes from lineations in the seismicity [*Giardini and Woodhouse,* 1986], suggest that any component of along-arc strain rate at least in part displaces deeper lithosphere to the south, assuming that aseismic flow and seismic deformation have the same geometry.

Strain rate data indicate that the proportion of along-arc strain rate decreases south to north. Since estimates of scalar strain rate are constant with latitude, the degree of advective thickening perpendicular to the arc reaches a maximum in southern Tonga. If along-arc flow occurs largely as southward shear of the deeper lithosphere, vector descriptions of strain rate may require thickening factors of at least 1.5 in central Tonga. Given advective thickening on the order of 50%, strain in the seismically active core of the slab may be accounted for by the observed values of scalar strain release. Substantially greater deformation would be largely aseismic. Thickening factors greater than one may not be necessary to match strain rate data from the arcs of the northwest Pacific where the scalar values of strain rate are substantially smaller than in the deep Tonga slab.

While the large flux of lithospheric material into the lower mantle represented by the zones of documented slab penetration (100 km^3/y) argues against rigorously stratified convection, a discontinuity in the physical properties of the mantle, such as an increase in viscosity [*Vassiliou et al.*, 1984; *Kincaid and Olson,* 1987; *Gurnis and Hager,* 1988] or perhaps a small variation in mantle chemistry [*Silver et al.*, 1988] is completely plausible if it merely resists the descending slabs without acting as a complete barrier to flow. In this type of model the slab extends into the lower mantle, but how far it reaches or how much it deforms is a function of the type and degree of discontinuity. Therefore, the minimum amount of advective thickening required by the Tonga strain rate data, and the rejection of thickening factors greater than three in the Kuril-Kamchatka arc, provide direct observational constraints which must be incorporated into estimation of physical and chemical mantle parameters.

Clearly, however, a wider variety of data may be exploited to investigate lower mantle slab morphology. In arcs such as Tonga and the Marianas where observed travel time residuals allow the slab to thicken by factors of five or more, precise tectonic reconstructions for the early history of these regions may yield tighter bounds on the scale of cross-strike flow. Furthermore, the frequency dependent characteristics of seismic waveform data hold promise for finer resolution of slab width than ray-theory based studies of travel time data [*Vidale,* 1987; *Vidale and Garcia-Gonzalez,* 1988; *Cormier,* 1988]. Finally, given that the residual sphere method and certain regional tomographic studies lose resolution at depths of 900 km – 1000 km, data including deeper turning raypaths are also required. For instance, *Grand* [1987] traces a slab-like anomaly under eastern North America to depths of 2000 km, and lower mantle models obtained from global tomography suggest that subduction-related downwellings may extend even to the core-mantle boundary [*Woodhouse and Dziewonski,* 1987]. These results suggest future studies in which a full range of seismological data and techniques are exploited to map slab flow into the lower mantle, thus providing powerful constraints on global models of mantle circulation.

REFERENCES

Abe, K., and H. Kanamori, Temporal variation of the activity of intermediate and deep focus earthquakes, *J. Geophys. Res., 84*, 3589–3595, 1979.

Ansell, J. H., and D. Gubbins, Anomalous high-frequency wave propagation from the Tonga-Kermadec seismic zone to New Zealand, *Geophys. J. R. astr. Soc., 85,* 93–106, 1986.

Apperson, K. D. and C. Frohlich, The relationship between Wadati-Benioff zone geometry and P, T and B axes of intermediate and deep focus earthquakes, *J. Geophys. Res.*, *92*, 13,821–13,980, 1987.

Backus, G. and F. Gilbert, Uniqueness in the inversion of inaccurate gross earth data, *Philos. Trans. R. Soc. Ser. A., 266,* 123–192, 1970.

Barazangi, M., B. Isacks, and J. Oliver, Propagation of seismic waves through and beneath the lithosphere that descends under the Tonga island arc, *J. Geophys. Res., 77*, 952–958, 1972.

Beck, S. L., and T. Lay, Test of the lower mantle penetration hypothesis using broadband *S* waves, *Geophys. Res. Lett., 13,* 1007–1010, 1986.

Billington, S., The morphology and tectonics of the subducted lithosphere in the Tonga-Fiji-Kermadec region from seismicity amd focal mechanism solutions, Ph.D. dissertation, Cornell University, Ithaca, NY, 1980.

Billington, S., and B. L. Isacks, Identification of fault planes associated with deep earthquakes, *Geophys. Res. Lett., 2*, 63–66, 1975.

Bock, G., P wave travel times from deep and intermediate-depth earthquakes to local seismic stations and the subducted slab of oceanic lithosphere beneath the Tonga island arc, *J. Geophys. Res., 92*, 13,863–13,877, 1987.

Bock, G., The effect of the descending lithosphere beneath th Tonga island arc on P–wave travel-time residuals at the Warramunga seismic array, *Phys. Earth Planet. Int. 25*, 360–371, 1981.

Bock, G., and J. Ha, Short-period S–P conversion in the mantle at a depth near 700 km, *Geophys. J. R. astr. Soc., 77,* 593–615, 1984.

Boyd, T. M., and K. C. Creager, Kinematic and travl-time constraints on aseismic extensions of the Aleutian slab, *J. Geophys. Res.,* in review, 1988.

Brune, J. N. Seismic moment, seismicity, and rate of slip along major fault zones, *J. Geophys. Res., 73,* 777–784, 1968.

Cathles, L. M., III, *The Viscosity of the Earth's Mantle,* Princeton University Press, 386 pp., Princeton, N. J., 1975.

Cerveny, V., and J. Jansky, Ray amplitudes of seismic body waves in homogeneous radially symmetric media, *Stud. Geophys. Geod., 27,* 9–18, 1983.

Chen, W., and P. Molnar, Seismic moments of major earthquakes and the average rate of slip in central Asia, *J. Geophys. Res., 82*, 2945–2969, 1977.

Christensen, D. H. and T. Lay, Large earthquakes in the Tonga region associated with subduction of the Louisville Ridge, *J. Geophys. Res., 93,* 13,367–13,389, 1988.

Coleman, P. J., and G. H. Packham, The Melanesian borderlands and the Indian-Pacific plates boundary, *Earth-Sci. Rev., 83*, 4995–5003, 1978.

Cormier, V. F., Slab Diffraction of S waves, *J. Geophys. Res.*, in press, 1988.

Creager, K. C., Geometry, velocity structure, and penetration depths of descending slabs in the western Pacific, Ph.D. dissertation, Univ. of Calif., San Diego, La Jolla, 1984.

Creager, K. C., and T. H. Jordan, Slab penetration into the lower mantle, *J. Geophys. Res., 89*, 3031–3049, 1984.

Creager, K. C., and T. H. Jordan, Slab penetration into the lower mantle beneath the Mariana and other island arcs of the northwest Pacific, *J. Geophys. Res., 91,* 3573–3589, 1986.

Davies, D., and D. P. McKenzie, Seismic travel time residuals and plates, *Geophys. J. R. Astron Soc., 18,* 51–63, 1969.

Davies, G. F., Mechanics of subducted lithosphere, *J. Geophys. Res., 85,* 6304–6318, 1980.

Dziewonski, A. M., Mapping the lower mantle: Determination of lateral heterogeneity in *P* wave velocity up to degree and order 6, *J. Geophys. Res., 89,* 5929–5952, 1984.

Dziewonski, A. M., and D. L. Anderson, Travel times and station corrections for *P* waves at teleseismic distances, *J. Geophys. Res., 88,* 3295–3314, 1983.

Dziewonski, A. M., and F. Gilbert, The effect of small, aspherical perturbations on travel times and a re-examination of the corrections for ellipticity, *Geophys. J. R. Astron. Soc., 44,* 7–17, 1976.

Dxiewonski, A. M., and J. H. Woodhouse, An experiment in the systematic study of global seismicity: centroid-moment tensor solutions for 201 moderate and large earthquakes of 1981, *J. Geophys. Res., 88,* 3247–3271, 1983.

Dziewonski, A. M., and J. H. Woodhouse, Global images of the Earth's interior, *Science, 236,* 37–48, 1987.

Dziewonski, A. M., T. A. Chou, and J. H. Woodhouse, Determination of earthquake source parameters from waveform data for studies of global and regional seismicity, *J. Geophys. Res., 86,* 2825–2852, 1981.

Dziewonski, A.M., A. Friedman, D. Giardini, and J. H. Woodhouse, Global seismicity of 1982: Centroid-moment tensor solutions for 308 earthquakes, *Phys. Earth Planet. Int., 33,* 76–90, 1983a.

Dziewonski, A.M., A. Friedman, and J. H. Woodhouse, Centroid-moment tensor solutions for January - March 1983, *Phys. Earth Planet. Int., 33,* 71–75, 1983b.

Dziewonski, A.M., J. E. Franzen, and J. H. Woodhouse, Centroid-moment tensor solutions for April - June 1983, *Phys. Earth Planet. Int., 33,* 243–249, 1983c.

Dziewonski, A.M., J. E. Franzen, and J. H. Woodhouse, Centroid-moment tensor solutions for July - September 1983, *Phys. Earth Planet. Int., 34,* 1–8, 1984a.

Dziewonski, A.M., J. E. Franzen, and J. H. Woodhouse, Centroid-moment tensor solutions for October - December 1983, *Phys. Earth Planet. Int., 34,* 129–136, 1984b.

Dziewonski, A.M., J. E. Franzen, and J. H. Woodhouse, Centroid-moment tensor solutions for January - March 1984, *Phys. Earth Planet. Int., 34,* 209–219, 1984c.

Dziewonski, A.M., J. E. Franzen, and J. H. Woodhouse, Centroid-moment tensor solutions for April - June 1984, *Phys. Earth Planet. Int., 37,* 1–8, 1985a.

Dziewonski, A.M., J. E. Franzen, and J. H. Woodhouse, Centroid-moment tensor solutions for July - September 1984, *Phys. Earth Planet. Int., 38,* 203–213, 1985b.

Dziewonski, A.M., J. E. Franzen, and J. H. Woodhouse, Centroid-moment tensor solutions for October - December 1984, *Phys. Earth Planet. Int., 39,* 147–156, 1985c.

Dziewonski, A.M., J. E. Franzen, and J. H. Woodhouse, Centroid-moment tensor solutions for January - March 1985, *Phys. Earth Planet. Int., 40,* 249–258, 1985d.

Dziewonski, A.M., J. E. Franzen, and J. H. Woodhouse, Centroid-moment tensor solutions for April - June 1985, *Phys. Earth Planet. Int., 41,* 215–224, 1986a.

Dziewonski, A.M., J. E. Franzen, and J. H. Woodhouse, Centroid-moment tensor solutions for July - September 1985, *Phys. Earth Planet. Int., 42,* 205–214, 1986b.

Dziewonski, A.M., J. E. Franzen, and J. H. Woodhouse, Centroid-moment tensor solutions for October - December 1985, *Phys. Earth Planet. Int., 43,* 185–195, 1986c.

Dziewonski, A.M., G. Ekstrom, J. E. Franzen, and J. H. Woodhouse, Centroid-moment tensor solutions for January - March 1986, *Phys. Earth Planet. Int., 45,* 1–10, 1987a.

Dziewonski, A.M., G. Ekstrom, J. E. Franzen, and J. H. Woodhouse, Global seismicity of 1977: Centroid-moment tensor solutions for 471 earthquakes, *Phys. Earth Planet. Int., 45,* 11–36, 1987b.

Dziewonski, A.M., G. Ekstrom, J. E. Franzen, and J. H. Woodhouse, Centroid-moment tensor solutions for April - June 1986, *Phys. Earth Planet. Int., 45,* 229–239, 1987c.

Dziewonski, A.M., G. Ekstrom, J. E. Franzen, and J. H. Woodhouse, Centroid-moment tensor solutions for July - September 1986, *Phys. Earth Planet. Int., 46,* 305–315, 1987d.

Dziewonski, A.M., G. Ekstrom, J. E. Franzen, and J. H. Woodhouse, Global seismicity of 1978: Centroid-moment tensor solutions for 512 earthquakes, *Phys. Earth Planet. Int., 46,* 316–342, 1987e.

Dziewonski, A.M., G. Ekstrom, J. E. Franzen, and J. H. Woodhouse, Global seismicity of 1979: Centroid-moment tensor solutions for 524 earthquakes, *Phys. Earth Planet. Int., 48,* 18–46, 1987f.

Dziewonski, A.M., G. Ekstrom, J. E. Franzen, and J. H. Woodhouse, Centroid-moment tensor solutions for October - December 1986, *Phys. Earth Planet. Int., 48,* 5–17, 1987g.

Dziewonski, A.M., G. Ekstrom, J. H. Woodhouse, and G. Zwart, Centroid-moment tensor solutions for January - March 1987, *Phys. Earth Planet. Int., 50,* 116–126, 1988a.

Dziewonski, A.M., G. Ekstrom, J. E. Franzen, and J. H. Woodhouse, Global seismicity of 1980: Centroid-moment tensor solutions for 515 earthquakes, *Phys. Earth Planet. Int., 50,* 127–154, 1988b.

Dziewonski, A.M., G. Ekstrom, J. E. Franzen, and J. H. Woodhouse, Global seismicity of 1981: Centroid-moment tensor solutions for 542 earthquakes, *Phys. Earth Planet. Int., 50,* 155–182, 1988c.

Dziewonski, A.M., G. Ekstrom, J. H. Woodhouse, and G. Zwart, Centroid-moment tensor solutions for April - June 1987, *Phys. Earth Planet. Int., 50,* 215–225, 1988d.

Engdahl, E. R., and D. Gubbins, Simultaneous travel time inversion for earthquake location and subduction zone structure in the central Aleutian Islands, *J. Geophys. Res., 92,* 13,855–13,862, 1987.

Engdahl, E. R., J. E. Vidale, and V. F. Cormier, Wave propagation in subducted lithospheric slabs, Proceedings of the 6th Course: Digital Siesmology and Fine Modeling of the

Lithosphere, International School of Applied Geophysics, Majorana Center, Erice, Sicily, Plenum Publishing Company, in press, 1988.

Ekstrom, G., and A. Dziewonski, Evidence of bias in estimations of earthquake size, *Nature, 332,* 319–323, 1988.

Engdahl, E. R., Effects of plate structure and dilatancy on relative teleseismic P-wave residuals, *Geophys. Res. Lett., 2,* 420–422, 1975.

Engdahl, E. R., N. H. Sleep, and M.-T. Lin, Plate effects in north Pacific subduction zones, *Tectonophysics, 37,* 95–116, 1977.

Fischer, K. M., T. H. Jordan, and K. C. Creager, Seismic constraints on the morphology of deep slabs, *J. Geophys. Res., 93*, 4773–4783, 1988.

Fischer, K. M., K. C. Creager, and T. H. Jordan, Mapping the Tonga slab, *Eos Trans. AGU, 67,* 316, 1986.

Fitch, T. J., Compressional velocity in source regions of deep earthquakes: An application of the master earthquakes technique, *Earth Planet. Sci. Lett., 26,* 156–166, 1975.

Fitch, T. J., *In situ P*-wave velocities in deep earthquake zones of the southwest Pacific: Evidence for a phase boundary between the upper an lower mantle, *In* Island arcs, deep sea trenches, and back-arc basins, (M. Talwani and W. C. Pitman III, eds.) Amer. Geophys. Union, Washington, D.C., 123–136, 1977.

Frohlich, C., and M. Barazangi, A regional study of mantle velocity variations beneath eastern Australia and the southwestern Pacific using short-period recordings of *P, S, PcP, ScP* and *ScS* waves produced by Tongan deep earthquakes, *Phys. Earth Planet. Int., 21,* 1–14, 1980.

Fujita, K., E. R. Engdahl, and N. H. Sleep, Subduction zone calibration and teleseismic relocation of thrust zone events in the central Aleutian Islands, *Bull. Seismol. Soc. Am., 71,* 1805–1828, 1981.

Fukao, Y., K. Yamaoka, and T. Sakurai. Spherical shell tectonics: Buckling of the subducted lithosphere, *Phys. Earth Planet. Int., 45,* 59–67, 1987.

Garfunkel, Z., C. A. Anderson, and G. Schubert, Mantle circulation and the lateral migration of subducted slabs, *J. Geophys. Res., 91,* 7205–7224, 1986.

Gephart, J. W., Principal stress directions and the ambiguity in fault plane identification from focal mechanisms, *Bull. Siesmol. Soc. Am., 75,* 621–625, 1985.

Gephart, J. W., and D. W. Forsyth, An improved method for determining the regional stress tensor using earthquake focal mechanism data: application to the San Fernando earthquake sequence, *J. Geophys. Res., 89,* 9305–9320, 1984.

Giardini, D., Systematic analysis of deep seismicity: 200 centroid-moment tensor solutions for earthquakes between 1977 and 1980, *Geophys. J. R. Astron Soc., 77,* 883–914, 1984.

Giardini, D., Frequency distribution and quantification of deep earthquakes, *J. Geophys. Res., 93,* 2095–2105, 1988.

Giardini, D., and J. H. Woodhouse, Horizontal shear flow in the mantle beneath the Tonga arc, *Nature, 319,* 551–555, 1986.

Giardini, D., and J. H. Woodhouse, Deep seismicity and modes of deformation in Tonga subduction zone, *Nature, 307,* 505–509, 1984.

Gill, J., and M. Gorton, A proposed geological and geochemical history of eastern Melanesia, *In* The western Pacific: Island arcs, marginal seas, geochemistry, (P. J. Coleman, editor), Univ. West. Austr. Press, Nedlands, 127–145, 1973.

Grand, S. P., Tomographic inversion for shear velocity beneath the North American plate, *J. Geophys. Res., 92,* 14,065–14,090, 1987.

Gurnis, M., and B. Hager, Controls of the Structure of subducted slabs, *Nature, 335,* 317–321, 1988.

Gutenberg, B., and C. F. Richter, Magnitude and energy of earthquakes, *Nature, 176,* 795–796, 1955.

Gutenberg, B., and C. F. Richter, Magnitude and energy of earthquakes, *Ann. Geofis., 9,* 1–15, 1956.

Hager, B. H., Subducted slabs and the geoid: Constraints on mantle rheology and flow, *J. Geophys. Res., 89,* 6003–6015, 1984.

Hager, B. H., R. J. O'Connell, and A. Raefsky, Subduction, back-arc spreading and global mantle flow, *Tectonophysics, 99,* 165–189, 1983.

Hager, B. H., R. W. Clayton, M. A. Richards, R. P. Comer, and A. M. Dziewonski, Lower mantle heterogeneity, dynamic topography and the geoid, *Nature, 313,* 541–545, 1985.

Hamburger, M.W., and B. L. Isacks, Diffuse back-arc deformation in the southwestern Pacific, *Nature, 332,* 599–604, 1988.

Hamburger, M.W., and B. L. Isacks, Deep earthquakes in the southwest Pacific: A tectonic interpretation, *J. Geophys. Res., 92*, 13,841–13,854, 1987.

Hanks, T. C., and H. Kanamori, A moment magnitude scale, *J. Geophys. Res., 84,* 2348–2350, 1979.

Hanus, V., and J. Vanek, Tonga-Lau system: Deep Collision of subducted lithospheric plates, *J. Geophys., 44,* 473–480, 1978.

Herrin, E., et al., 1968 seismological tables for *P* phases, *Bull. Seismol. Soc. Am., 58*, 1196–1241, 1968.

Hilde, T. W. C., S. Uyeda, and L. Kroenke, Tectonic history of the western Pacific, in *Geodynamics Progress and Prospects,* edited by C. L. Drake, pp. 1–15, AGU, Washington, D.C., 1976.

Huppert, L. N., and C. Frohlich, The P velocity within the Tonga Benioff zone determined from trace rays and observations, *J. Geophys. Res., 86,* 3771–3782, 1981.

Hsui, A. T., X.-M. Tang, and M. N. Toksöz, Thermal structure, gravitational torque and evolution of the dip angle of a subducting plate, *Geophys. Res.,* submitted, 1988.

Isacks, B., J. Oliver, and L. R. Sykes, Seismology and the new global tectonics, *J. Geophys. Res., 73,* 5855–5899, 1968.

Isacks, B., and P. Molnar, Mantle earthquake mechanisms and sinking of the lithosphere, *Nature, 223,* 1121–1124, 1969.

Isacks, B. L., L. R. Sykes, and J. Oliver, Spatial and temporal clustering of deep and shallow earthquakes in the Fiji-Tonga-Kermadec region, *Geol. Soc. Am. Bull., 80,* 1443–1470, 1969.

Isacks, B., and P. Molnar, Distribution of stress in the descending lithosphere from a global survey of focal-mechanism solutions of mantle earthquakes, *Rev. Geophys., 9,* 103–174, 1971.

Isacks , B. L. and M. Barazangi, Geometry of Benioff zones: Lateral segmentation and downwards bending of the subducted lithosphere, *In* Island arcs, deep sea trenches, and back-arc basins, (M. Talwani and W. C. Pitman III, eds.) Amer. Geophys. Union, Washington, D.C., 99–114, 1977.

Ito, E., and H. Yamada, Stability relations of silicate spinels, ilmenites, and perovskites, in High Pressure Research in Geophysics, edited by S. Akimoto and M. H. Manghnani, pp. 405–419, Center Acad. Pub. Japan, Tokyo, 1982.

Jackson. J., and D. McKenzie, The relationship between plate motions and seismic moment tensors, and the rates of active deformation in the Mediterranean and Middle East, *Geophys. J. R. Astron. Soc., 93,* 45–73, 1988.

Jeanloz, R., and A. B. Thompson, Phase transitions and mantle discontinuities, *Rev. Geophys., 21,* 51–74, 1983.

Jordan, T. H., Lateral heterogeneity and mantle dynamics, *Nature, 257,* 745–750, 1975.

Jordan, T. H., Lithospheric slab penetration into the lower mantle beneath the Sea of Okhotsk, *J. Geophys., 43,* 473–496, 1977.

Jordan, T. H., and K. A. Sverdrup, Teleseismic location techniques and their application to earthquake clusters in the south-central Pacific, *Bull. Seismol. Soc. Am., 71,* 1105–1130, 1981.

Jordan, T. H., and W. S. Lynn, A velocity anomaly in the lower mantle, *J. Geophys. Res., 79,* 2679–2685, 1974.

Jordan, T. H., A. L. Lerner-Lam, and K. C. Creager, Seismic imaging of mantle convection: the evidence for deep circulation, in *Mantle Convection,* edited by W. R. Peltier, in press, 1988.

Kamiya, S., T. Miyatake, and K. Hirahara, How deep can we see the high velocity anomalies beneath the Japan islands?, *Geophys. Res. Lett., 15,* 829–831, 1988.

Karig, D. E., Ridges and basins of the Tonga-Kermadec island arc system, *J. Geophys. Res., 75,* 239–255, 1970.

Karig, D. E., and J. Mammerickx, Tectonoc framework of the New Hebrides island arc, *Marine Geol., 12,* 187–205, 1972.

Kawakatsu, H., Downdip tensional earthquakes beneath the Tonga arc: a double seismic zone?, *J. Geophys. Res., 91,* 6432–6440, 1986.

Kincaid, C., and P. Olson, An experimental study of subduction and slab migration, *J. Geophys. Res., 92,* 13,832–13,840, 1987.

Kostrov, V. V., Seismic moment and energy of earthquakes, and seismic flow of rock. *Ivz. Acad. Sci. USSR Phys. Solid Earth, 1,* 23–44, 1974.

Kroenke, L., Tonga: the Tonga Ridge and Trench; the Lau Ridge and Trough, *U. N. ESCAP CCOP/SOPAC Tech. Bull., 6,* 77–86, 1984.

Larson, R. L. and Chase, C. G., Late Mesozoic evolution of the western Pacific ocean, *Bull. Geol. Soc. Am., 83,* 3627–3644, 1972.

Lay, T., Localized velocity anomalies in the lower mantle, *Geophys. J. R. Astron. Soc., 72,* 483–516, 1983.

Liu, L., The high-pressure phases of $MgSiO_3$, *Earth Planet. Sci. Lett., 31,* 200–208, 1976a.

Liu, L., The post-spinel phase of forsterite, *Nature, 262,* 770–772, 1976b.

Louat, R., and J. Dupont, Sismicite de l'arc des Tonga-Kermadec, *Trav. Docum. Off. Rech. Scient. Techn. Outre-Mer, 147,* 299–318, 1972.

Malvern, L. E., *Introduction to the Mechanics of a Continuous Medium,* Prentice-Hall, Englewood Cliffs, New Jersey, 1969.

McConnell, R. K., Viscosity of the mantle from relaxation time spectra of isostatic adjustment, *J. Geophys. Res., 73,* 7089–7105, 1968.

McGarr, A., Seismic moments of earthquakes beneath island arcs, phase changes, and subduction velocities, *J. Geophys. Res., 82,* 256–264,1977.

McKenzie, D., and J. Jackson, The relationship between strain rates, crustal thickening, palaeomagnetism, finite strain and fault movements within a deforming zone, *Earth Planet. Sci. Lett., 65,* 182–202, 1983.

Minster, J. B., T. H. Jordan, P. Molnar, and E. Haines, Numerical modeling of instantaneous plate tectonics, *Geophys. J. R. Astron. Soc., 36,* 541–576, 1974.

Minster, J. B., and T. H. Jordan, Present-day plate motions, *J. Geophys. Res., 83,* 5331–5354, 1978.

Mitronovas, W., and B. L. Isacks, Seismic velocity anomalies in the upper mantle beneath the Tonga-Kermadec island arc, *J . Geophys. Res., 76,* 7154–7180, 1971.

Molnar, P., Average regional strain due to slip on numerous faults of different orientations, *J. Geophys. Res., 88,* 6430–6432, 1983.

Molnar, P., T. Atwater, J. Mammerickx, and S. M. Smith, Magnetic anomalies, bathymetry and the tectonic evolution of the south Pacific since the late Cretaceous, *Geophys. J. R. Astron. Soc., 40,* 383–420, 1975.

Molnar, P., and D. Qidong, Faulting associated with large earthquakes and the average rate of deformation in central and eastern Asia, *J. Geophys. Res., 89,* 6203–6227, 1984.

Nieman, T. L., K. Fujita, and W. R. Rogers, Jr., Teleseismic mislocation of eathquakes in island arcs – theoretical results, *J. Phys. Earth, 34,* 43–70, 1986.

Oliver, J., and Isacks, B., Deep earthquake zones, anomalous structures in the upper mantle, and the lithosphere, *J. Geophys. Res., 72,* 4259–4275, 1967.

Peltier, W. R., The impulse response of a Maxwell Earth, *Rev. Geophys., 12,* 649–669, 1974.

Peltier, W. R., Ice-age geodynamics, *Annu. Rev. Earth Planet. Sci., 9,* 199–225, 1981.

Peltier, W. R., and P. Wu, Mantle phase transitions and the free-air gravity anomalies over Fennoscandia and Laurentia, *Geophys. Res. Lett., 9,* 731–734, 1982.

Prasad, G., and G. Bock, *P*-wave travel-times from the Tonga subduction zone to stations on the oceanic side of the Tonga-Kermadec trench, *Geophys. Res. Lett., 14,* 9–12, 1987.

Richter, F. M., Focal mechanisms and seismic energy release of deep and intermediate earthquakes in the Tonga-Kermadec region and their bearing on the depth extent of mantle flow, *J. Geophys. Res., 84,* 6783–6795, 1979.

Riedesel, M. A., Seismic moment tensor recovery at low frequencies, Ph.D. dissertation, Univ. of Calif., San Diego, La Jolla, 1985.

Riedesel, M. A., and T. H. Jordan, Display and assessment of seismic moment tensors, *Bull. Seismol. Soc. Am.,* in review, 1988.

Sammis, C. G., J. C. Smith, G. Schubert, and D. A. Yuen, Viscosity-depth profile of the Earth's mantle: Effects of polymorphic phase transformations, *J. Geophys. Res., 82,* 3741–3761, 1977.

Schneider, J. F., and I. S. Sacks, Stress in the contorted Nazca plate beneath southern Peru from local earthquakes, *J. Geophys. Res., 92*, 13,887–13,902, 1987.

Silver, P., and W. Chan, Observations of body wave multipathing from broadband seismograms: Evidence for lower mantle slab penetration beneath the Sea of Okhotsk, *J. Geophys. Res., 91,* 13,787–13,802, 1986.

Silver, P., and T. Jordan, Optimal estimation of scalar seismic moment, *Geophys. J. R. astr. Soc., 70,* 755–787, 1982.

Silver, P., R. W. Carlson, and P. Olson, Deep slabs, geochemical heterogeneity and the large-scale structure of mantle convection: Investigation of an enduring paradox, *Annu. Rev. Earth Planet. Sci.,* in press, 1988.

Sleep, N. H., Teleseismic *P* wave transmission through slabs, *Bull. Seismol. Soc. Am., 63,* 1349–1373, 1973.

Sondergeld, C. H., B. L. Isacks, M. Barazangi, and S. Billington, A search for velocity anomalies near the deep portions of the inclined seismic zone of Tonga Island arc, *Bull. Seismol. Soc. Am., 67,* 537–541, 1977.

Suito, K., Phase relations of pure Mg_2SiO_4 up to 200 kilobars, in High Pressure Research, Applications in Geophysics, ed. by M. H. Manghnani and S. Akimoto, pp. 255-266, Academic, New York, 1977.

Sumino, Y., The elastic constants of Mn_2SiO_4, Fe_2SiO_4, and Co_2SiO_4, and the elastic properties of olivine group minerals at high temperature, *J. Phys. Earth, 27,* 209–238, 1979.

Sumino, Y., O. L. Anderson, and I. Suzuki, Temperature coefficients of elastic constants of single crystal MgO between 80° and 1300° K, *Phys. Chem. Minerals, 9*, 38–47, 1983.

Suzuki, I., O. L. Anderson, and Y. Sumino, Elastic properties of a single-crystal forsterite Mg_2SiO_4 up to 1200° K, *Phys. Chem. Miner., 10,* 38–46, 1983.

Suzuki, I., and O. L. Anderson, Elasticity and thermal expansion of a natural garnet up to 1000° K, *J. Phys. Earth, 31,* 125–138, 1983.

Sykes, L. R., The seismicity and deep structure of island arcs, *J. Geophys. Res., 71,* 2981–3006, 1966.

Toksöz, N., J. W. Minear, and B. R. Julian, Temperature field and geophysical effects of a downgoing slab, *J. Geophys. Res., 76,* 1113–1138, 1971.

Toksöz, M. N., N. H. Sleep, and A. T. Smith, Evolution of the downgoing lithosphere and the mechanisms of deep focus earthquakes, *Geophys. J. R. Astron. Soc., 35,* 285–310, 1973.

Vassiliou, M. S., The state of stress in subducting slabs as revealed by earthquakes analysed by moment tensor inversion, *Earth Planet. Sci. Lett., 69,* 195–202, 1984.

Vassiliou, M. S., B. H. Hager, and A. Raefsky, The distribution of earthquakes with depth and stress in subducting slabs, *J. Geodyn., 1,* 11–28, 1984.

Veith, K. F., The relationship of island arc seismicity to plate tectonics, Ph.D. dissertation, South. Methodist Univ., Dallas, Tex., 1974.

Vidale, J. E., Waveform effects of a high-velocity, subducted slab, *Geophys. Res. Lett., 14,* 542–545, 1987.

Vidale, J. E., and D. Garcia-Gonzalez, Seismic observation of a high-velocity slab 1200–1600 km in depth, *Geophys. Res. Lett., 15,* 369–372, 1988.

Vogt, P., Subduction and aseismic ridges, *Nature, 241,* 189–191, 1973.

Vogt, P. R., A. Lowrie, D. R. Bracey, and R. N. Hey, Subduction of aseismic oceanic ridges: Effects on shape, seismicity, and other characteristics of consuming plate boundaries, *Geol. Soc. Amer., Special Paper 172,* 1976.

Walcott, R. I., Structure of the Earth from glacio-isostatic rebound, *Annu. Rev. Earth Planet. Sci., 1,* 15–37, 1973.

Weidner, D. J., A mineral physics test of a pyrolite mantle, *Geophys. Res. Lett., 12,* 417–420, 1985.

Wright, D. J., The nature of the northern terminus of the Tonga Trench, southwest Pacific, Masters Thesis, Texas A and M University, College Station, Texas, 1986.

Wyss, M., R. E. Habermann, and J.-C. Griesser, Seismic quiescence and asperities in the Tonga-Kermadec arc, *J. Geophys. Res., 89,* 9293–9304, 1984.

Yagi, T., P. M. Bell, and H. K. Mao, Phase relations in the system MgO-FeO-SiO_2 between 150 and 700 kbar at 1000°C, *Carnegie Inst. Washington Year Book, 78,* 614–618, 1979.

Zhou, H., and R. Clayton, *P* and *S* wave travel-time inversions for subducting slab under the island arcs of the northwest Pacific, *J. Geophys. Res.*, in review, 1988.